UNIVERSITÀ DEGLI STUDI DI MILANO

PhD Course in Molecular and Cellular Biology

XXX Cycle

STUDY OF HCN CHANNELS INTERACTORS TRIP8B AND MINT PROTEINS

Chiara Donadoni

PhD Thesis

Scientific tutor: Anna Moroni

Academic year: 2017-2018

SSD: BIO/09

Thesis performed at Università degli studi di Milano, Dipartimento di Bioscienze (Milano, Italy) and Columbia University, Neuroscience department (New York, USA)

CONTENTS

PART I

1. SUMMARY

Ion channels are membrane proteins that control crucial physiological and pathological processes in all organisms. Channels are often composed by different subunits, forming macromolecular protein complexes. They include α subunits, which are the pore-forming channel subunits, and they also include β subunits, which associate to the α subunits and can regulate channel function, surface expression and trafficking (Yu et al. 2005).

Hyperpolarization-activated cyclic nucleotide gated channels (HCN1-4) are the molecular determinants of the so-called pacemaker current $I_{f/h}$ current which controls cell excitability both in the brain and in the heart (Robinson & S. a Siegelbaum 2003).

HCN channels are dually activated by membrane hyperpolarization and cAMP binding to their cyclic nucleotide binding domain (CNBD); moreover, several regulatory β subunits have been reported to regulate HCN channels (Robinson & S. a Siegelbaum 2003), among which TRIP8b.

The cytoplasmatic tetratricopeptide repeat containing Rab8b interacting protein (TRIP8b) is an auxiliary β subunit of neuronal HCN isoforms, governing ion channel trafficking and gating. The interaction between HCN and TRIP8b proteins is already well explained in molecular details and takes place at two distinct sites: an upstream binding site where the CNBD of HCN channels interacts with an 80 aa domain in the conserved central core of TRIP8b (called miniTRIP8b); and a downstream site where the C-terminal SNL (Ser-Asn-Leu) tripeptide of the channel interacts with the tetratricopeptide repeat domain of TRIP8b (Santoro et al. 2011).

In my thesis, I identified some key residues on the CNBD important for complex formation, and finally I was able to obtain an HCN double mutant $N_{547}D/A_{548}C$ unable to bind TRIP8b at the upstream binding site. This will prevent the regulation of channel activity by its β subunit without affecting the regulation of channel trafficking. This mutant represents an important tool that can be used *in vivo* to investigate the physiological importance of TRIP8b regulation of HCN channels in certain brain regions, such as the hippocampus.

Recently HCN channels were found to interact with Mint proteins. Less is known about this new interaction. Mints are a class of adaptor proteins which contain protein-protein interaction domains through which they mediate the assembly of functional multiprotein complexes (Rogelj et al. 2006). The study of Mint proteins has become central in Alzheimer's disease. Indeed, Mint proteins are known to directly bind the cytoplasmic tail of APP. This binding is important to regulate APP

trafficking and notably also its cleavage, thus β-amyloid peptide (Aβ) production (Rogelj et al. 2006).

Mints were recently reported to interact with HCN channels (Saito et al. 2012; Kimura et al. 2004) but neither the nature of the binding (direct vs. indirect) nor the interaction site between the two partners is so far known. In my thesis I have performed a preliminary characterization of this new interaction by a combination of *in vitro* and *in vivo* experimental approaches. In particular I have investigated the functional effects of the interaction between Mint proteins and HCN channels and found that Mint expression causes a decrease in HCN channel current, due to their redistribution from the plasma membrane to intracellular compartments. In addition I was able to identify a specific region located C-terminal to the CNBD of the channel which is important for the interaction.

2. STATE OF THE ART

2.1 If/Ih current

The If/Ih current (hyperpolarization-activated current) of excitable cells of brain and heart is an inward mixed (Na^+/K^+) cationic current which typically activates with hyperpolarization of the plasma membrane and it is also regulated by cyclic nucleotides (cAMP and cGMP) (Fig. 1) (Robinson & S. A. Siegelbaum 2003).

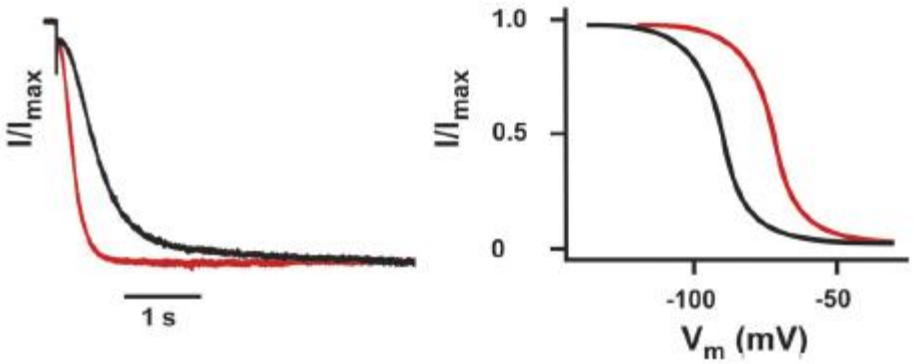

Figure 1 Left: I_h activates faster in the presence (red) than in the absence (black) of cAMP at maximal activation voltage (-140 mV). Right: activation curve of I_h in the absence (black) and presence (red) of cAMP. In the presence of cAMP, the activation curve of I_h is shifted to the right (Biel 2009).

Since its voltage dependence is opposite to the vast majority of the voltage-gated current which activates upon membrane depolarization, it was given the name of "funny current" (I_f) in the heart cells (Brown et al. 1979) and "queer current" (I_q) or "hyperpolarization activated current" (I_h) in neurons (the nomenclature used here) (Halliwell & Adams 1982).

Among all its physiological roles, I_h current is able to control the pacemaker activity (both in the heart and the brain), the resting potential and dendritic integration (Robinson & S. A. Siegelbaum 2003).

I_h current contributes to the genesis of the action potential in Purkinje cardiac fibers and in the SAN cells (DiFrancesco 1993), as in neuronal cells, such as the talamocortical relay neurons (Luthi & McCormick 1998) and the hippocampal stratum oriens interneurons (Maccaferri & McBain 1996). Indeed, the activation of I_h current at negative voltages in the repolarization phase of the action potential develops an excitatory inward current able to drive the membrane potential to the threshold for firing a subsequent action potential (Fig. 2).

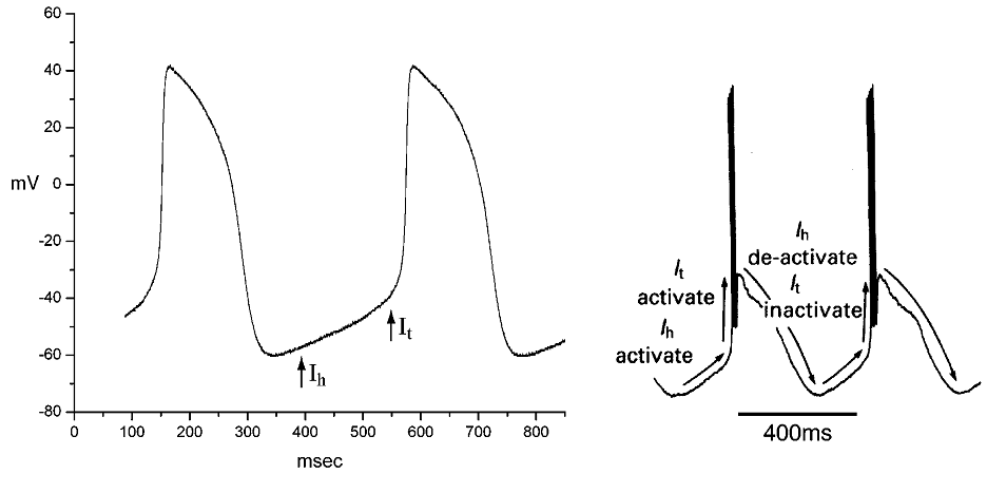

Figure 2 Pacemaking function of Ih in a cardiac sinoatrial node myocyte (left) and a thalamocortical neuron (right). In both cells, Ih activation, following an action potential produces a slow depolarization that triggers an action potential through activation of calcium channels. During the action potential, Ih deactivates and the calcium current inactivates causing repolarization (Robinson & S. A. Siegelbaum 2003).

In sinoatrial pacemaker cells and in many neurons, I_h is constitutively open at voltages near the resting membrane potential. It conducts a depolarizing inward current and sets the membrane potential to more depolarized voltages (Biel 2009). This current seems to function as a slow "voltage clamp": it counteracts both hyperpolarizing and depolarizing inputs by producing a depolarizing inward current (because of its activation) or by facilitating the hyperpolarization (because of its deactivation) (Nolan et al. 2007). In neurons, this ability to oppose to excitatory and inhibitory stimuli is important for the modulation of the amplitude and passive propagation of the excitatory postsynaptic potentials (EPSPs) and inhibitory postsynaptic potentials (IPSPs) (Magee & Carruth 1999; Steriade et al. 1993).

2.2 HCN channels

HCN (Hyperpolarization-activated and cyclic nucleotide-gated) channels represent the molecular determinants of I_h current. They belong to the superfamily of the voltage-gated K^+ channels (Ludwig et al. 1998). In all mammals, four homologous HCN channel subunits (HCN1-4) exist. These channels are expressed principally in the central nervous system and heart. The four isoforms are all expressed in the brain with different expression profiles: HCN3 shows the weakest expression whereas HCN2 has the widest expression profile. HCN1 is the second most expressed brain isoform and it shows a more selective expression profile compared to HCN2. It is highly expressed in the hippocampus, neocortex, cerebellar cortex and neuronal stem cells. HCN4 isoform

has a low expression which is restricted to specific regions like thalamus nuclei and mitral cells of the olfactory bulb (Santoro et al. 2000; Moosmang et al. 2001).

HCN channels are composed by four α subunits arranged around the centrally located pore (Biel 2009). They are able to organize themselves either in homo or hetero-tetramers (Altomare et al. 2003).

The α subunit of these channels is conserved and composed of six transmembrane segments (S1-S6): S4 is the voltage sensor of the channel while S5-S6 constitutes the pore region. They are composed of both intracellular N- and C-termini. The N-terminus and the extreme C-terminus are different in each isoform whereas the C-termini contains the C-linker/CNBD (cyclic nucleotide binding domain) region which is the better conserved of the four isoforms (Robinson & S. a Siegelbaum 2003; Biel 2009). The CNBD region is responsible for cAMP modulation of channel activity and it is connected to the pore region through the C-linker which propagates the regulation of channel gating exerted by the CNBD (Fig. 3).

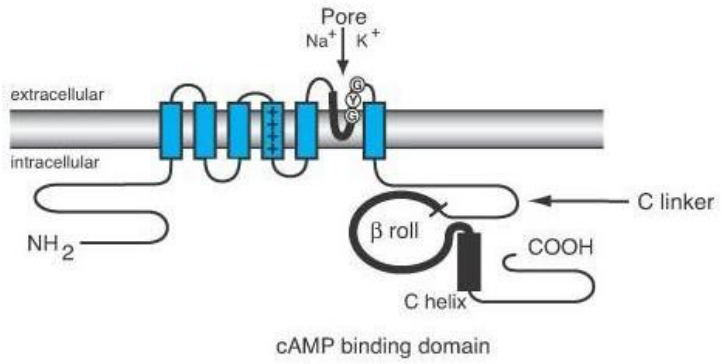

Figure 3 Transmembrane topology of a single HCN subunit indicating S1-S6 transmembrane region (blue rectangles), positive S4 segment, and pore-forming loop. It is also shown the C-terminal C-linker followed by the CNBD (in thick black) (Robinson & S. A. Siegelbaum 2003).

At the beginning of this year the structure of the human HCN1 was solved by means of cryo-electron microscopy (Lee & Mackinnon 2017) for the first time.

Figure 4 shows the structure of the human channel expressed without its extreme C-terminus. Four identical subunits form a 4-fold symmetric pore (composed by helices S5 and S6) (Fig.4, panels A and B) which is surrounded by the voltage sensor. The helix S6 bends at the level of the intracellular face of the membrane and gives rise to a helix-turn-helix structure named C-linker (in orange in Fig 4, panels C and D) which continues with the CNBD (in green in Fig.4, panels C and D) (Lee & Mackinnon 2017).

As regards the N-terminal part, the first 93 residues are not visible probably because of their unstructured or disordered nature. Moreover, a 3-α-helical domain (named HCN domain) (Fig.4 panel D in red) (Lee & Mackinnon 2017) is visible at the N-terminus for the first time.

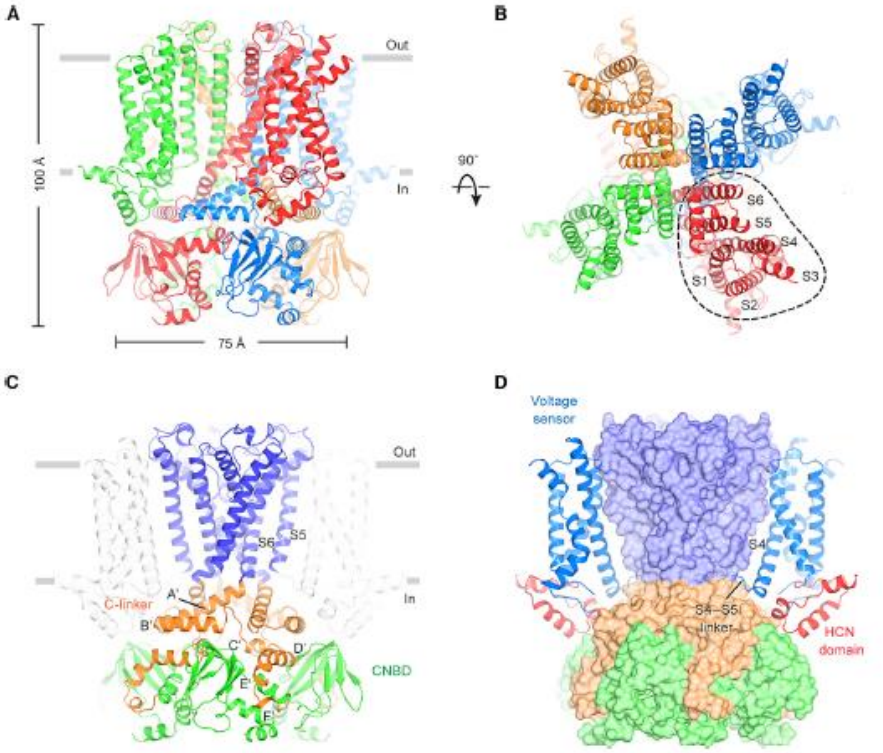

Figure 4 Structure of the human HCN1 channel. ***A,B****. Structure of the tetramer of the channel in the ligand-free state viewed parallel to the membrane (****A****) or from the extracellular side (****B****). Every subunit is represented in a different colour and membrane is represented by the grey lines.* ***C,D****. HCN channel domains. Transmembrane domain (from S1 and S6) is coloured in blue, the C-linker domain is represented in orange, the CNBD in green and the HCN domain in red* (Lee & Mackinnon 2017).

2.3 The CNB domain

The CNBD of HCN channels (Fig.5) comprises an antiparallel β-roll that includes the phosphate binding cassette (PBC). It is located between strands β6 and β7 and it constitutes the cAMP binding pocket, named PBC (Phosphate Binding Cassette) (Zagotta et al. 2003). In the N-terminal region, the N-terminal helical bundle is present and it is composed of an antiparallel helix–turn–helix motif formed by helices αE′ and αA. The N-terminal helical bundle has been conventionally associated to the C-linker sequence. Finally, at the distal end of the CNBD there are two C-terminal helices: αB and αC (Saponaro et al. 2014).

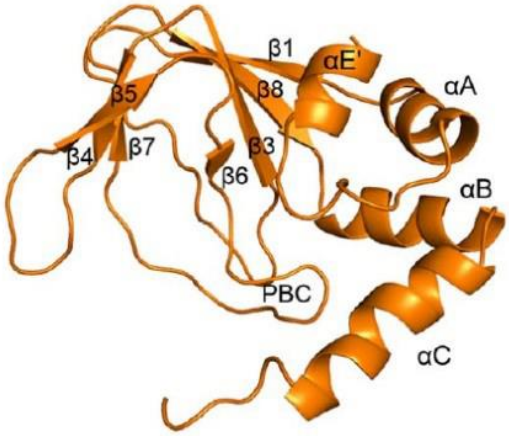

Figure 5 cAMP-free structure of human HCN2 CNBD with secondary structure elements labelled (Saponaro et al. 2014).

2.4 cAMP binding and regulation

HCN channels are not only regulated by membrane hyperpolarization but also by cyclic nucleotide binding. cAMP binding to CNBD increases the open probability at hyperpolarizing voltages and results in a shift of the voltage dependence of activation at more depolarizing potentials (Wainger et al. 2001) (Fig.1).

From the crystal of C-linker/CNBD of HCN2 bound to cAMP (Fig.6 left) it was possible to understand the residues involved in the cyclic nucleotide binding (Zagotta et al. 2003). Indeed, cAMP interacts with both the β-roll and the C-helix of the CNBD. The purine ring of cyclic nucleotide forms a hydrophobic interaction with I_{636}; moreover, it interacts with the methylene groups of R_{632} in the C-helix and V_{564}, M_{572} and L_{574} in the β-roll (Fig.6 right).

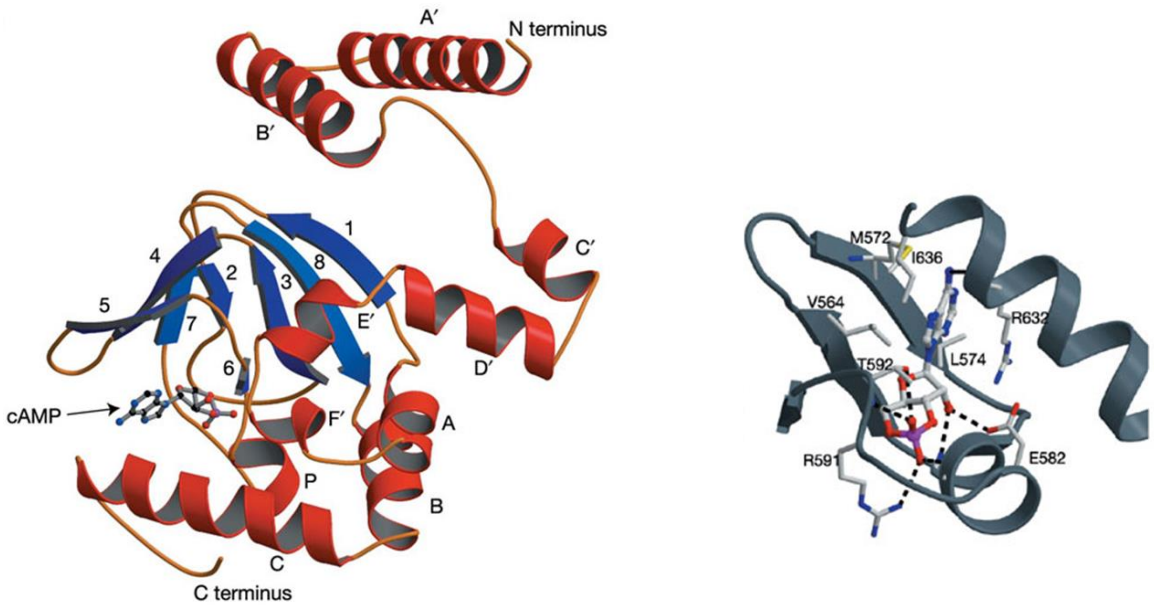

Figure 6 Structure of mHCN2 C-linker and CNBD bound to cAMP. Left: ribbon representation of an α subunit of mHCN2 bound to cAMP; right: stereoview of the cAMP-binding site, showing hydrogen bonds and salt bridges (broken lines) (Zagotta et al. 2003)

Later, a study combined molecular dynamics simulations with mutagenesis to identify ligand contacts which are important for the regulation of HCN2 channel by cyclic nucleotides. They found seven residues: three in the β-roll (R_{591}, T_{592} and E_{582}) and four in the C-helix (R_{632}, R_{635}, I_{636} and K_{638}). Surprisingly, out of seven residues that make strong contacts with ligand, only R_{632} in the C-helix of the CNBD is essential for high ligand efficacy, due to its selective stabilization of cAMP binding to the open state of the channel (L. Zhou and S. Siegelbaum 2007).

Moreover, comparing the cAMP-free and cAMP-bound structures of the CNBD (Fig.7), it was possible to understand the conformational changes which take place upon cyclic nucleotide binding. Notably, there are no differences in the β-roll, whereas the helical components of the CNBD undergo several rearrangements (Saponaro et al. 2014).

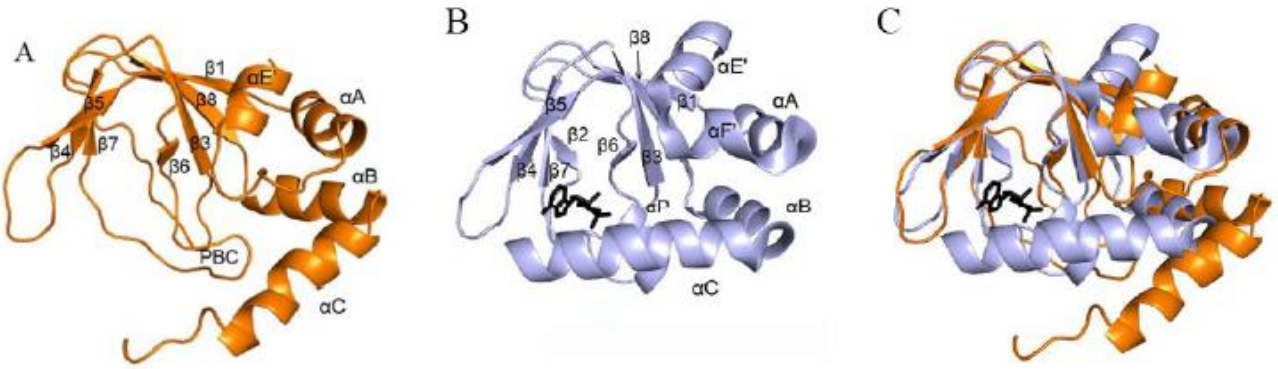

Figure 7 ***A.*** *HCN2 CNBD structure not bound to cAMP (in orange)* ***B.*** *HCN2 CNBD structure bound to cAMP (in grey). cAMP molecule is represented in black.* ***C.*** *Superposition of the cAMP-free (orange) and cAMP-bound (grey) structures of the CNBD* (Saponaro et al. 2014).

It is possible to notice in the PBC element that cAMP binding causes the formation of the P-helix. This indirectly causes the movement of the two C-terminal helices αB and αC: they move as a rigid body towards the core of the CNBD. Moreover, it is possible to notice that C-helix is one helical turn longer in the cAMP-bound form and that the movement of the C-helix sterically displaces the N-bundle which moves upward. Furthermore, in the N-terminal helical bundle, the formation of the αF' helix takes place upon cAMP binding (Saponaro et al. 2014).

A more detailed view of the mechanism of cAMP modulation was possible thanks to the structure of the human HCN1 in presence of cAMP. This allowed the identification of all the conformational changes that took place also at the C-linker level.

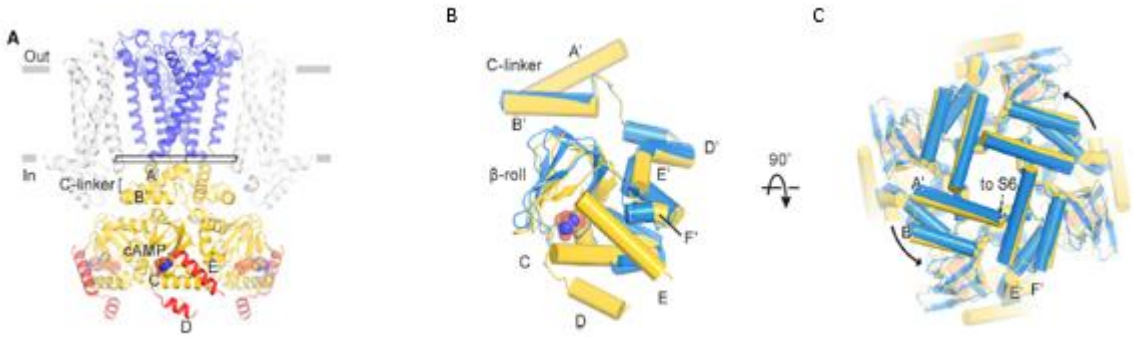

Figure 8 The modulation of the cyclic nucleotide on human HCN1. ***A.*** *Structure of human HCN1 channel bound to cAMP. The D and E helices are represented in red and the membrane is represented by the grey lines.* ***B,C****. Superposition of the C-linker and CNBD bound to cAMP (in yellow) and unbound (in blue). In* ***B*** *only one subunit is represented, in* ***C*** *all the four subunits are represented viewed from the extracellular side* (Lee & Mackinnon 2017).

First of all, it is possible to notice that in this structure two new helices (D and E, represented in red in Fig.8A) appear in the CNBD. These two helices are not observed in the structure unbound to the cyclic nucleotide but become ordered in the cAMP bound conformation. Looking at the superposition of the cAMP-bound and unbound structures (Fig.8 B and C) it is possible to see the conformational changes in the CNBD that propagate through the C-linker up to the pore. This propagated movement is a rotation of the cytoplasmic domain which propagates to the transmembrane region in order to favour channel opening (Lee & Mackinnon 2017).

2.5 TRIP8b

Besides being regulated by cAMP, HCN channels are also regulated by the association of other proteins. The most known and studied is TRIP8b (TPR-containing Rab8b interacting protein) which is a cytoplasmic protein expressed in the brain which can regulate both channel trafficking and gating (Santoro et al. 2004).

This protein co-localizes with HCN1 in the apical dendrites of CA1 pyramidal neurons of the hippocampus and neocortical layer V neurons (Santoro et al. 2004).

Nine splice variants of TRIP8b protein exist and they all share the conserved C-terminal region which contains the tetratricopeptide repeat (TPR) domain whereas they differ in the N-terminal. All these nine isoforms have a common effect on the gating of the channel but they have an isoform-specific effect on the trafficking of the channel (Santoro et al. 2009). The association of all TRIP8b isoforms has an inhibitory effect on channel opening by antagonizing the cAMP effect on channel opening and shifting the midpoint of activation ($V_{1/2}$) to more negative potentials (Fig.9) (Santoro et al. 2009; Lewis et al. 2009).

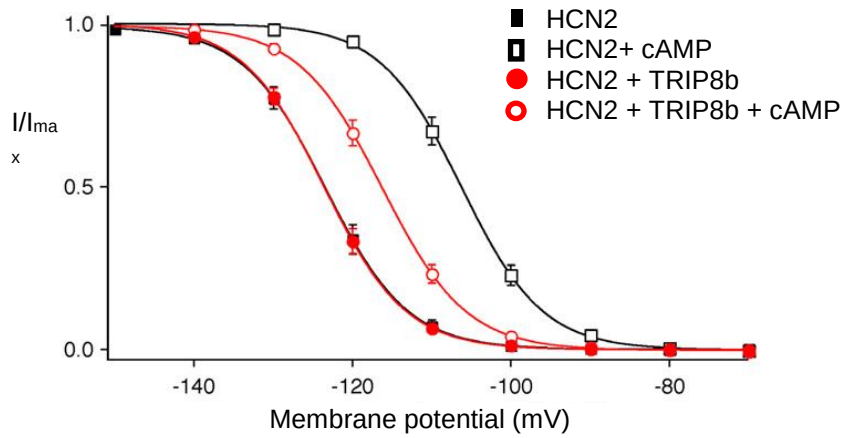

Figure 9 TRIP8b effect on HCN channel opening. Steady-state activation curves of HCN2 channels (black) and HCN2 and TRIP8b channels (red) before (filled symbols) and after application of 100 µM cAMP (open symbols). The right shift of the curve of activation due to cAMP is significantly reduced for HCN2 that is in complex with TRIP8b, indicating that TRIP8b is able to partially inhibit the cAMP effect. Image modified from (Zolles et al. 2009).

2.6 TRIP8b binding sites

TRIP8b effects on both channel trafficking and gating are achieved by the binding to the channels at two distinct binding sites, named upstream and downstream binding sites (Santoro et al. 2011).

At the level of the downstream binding site, the interaction takes place between the last three aminoacids (SLN) of HCN and the TPR domain of TRIP8b. The binding at the downstream interaction site is important to stabilize the C-terminal domain of TRIP8b, allowing for optimal interaction between HCN and TRIP8b as well as for proper assembly of the molecular complexes that mediate the effects of TRIP8b on HCN1 channel trafficking (Santoro et al. 2011).

At the upstream binding site, the interaction occurs between the CNBD of HCN channels and a conserved region of 80 amino acid (called miniTRIP8b) located in TRIP8b central core. This fragment is necessary and sufficient to interact with the CNBD of HCN channels and to exert the regulatory effect on cyclic nucleotide gating (Santoro et al. 2011).

Recently, using different structure predictions algorithms, miniTRIP8b sequence was analyzed. Part of the N- and C-termini, which were predicted to lack of secondary structure, were removed. This shorter construct obtained was 40 amino acids long (from residue 235 to 275 of the murine isoform 1a-4) and it was named nanoTRIP8b. By means of isothermal titration calorimetry (ITC), nanoTRIP8b ability to bind to the CNBD was tested and its affinity was the same of miniTRIP8b (Kd obtained with miniTRIP8b was 1.2 µM and with nanoTRIP8b was 1.5 µM) (Fig.10) (Saponaro et al., 2017 submitted).

235 275

KEHRWGSALLSR**NHSLEEEFERAKAAVESDTEFWDKMQAEWEEMARRNWISEN**QEAQNQVTVSASEKGYYFHTENPFKDWP

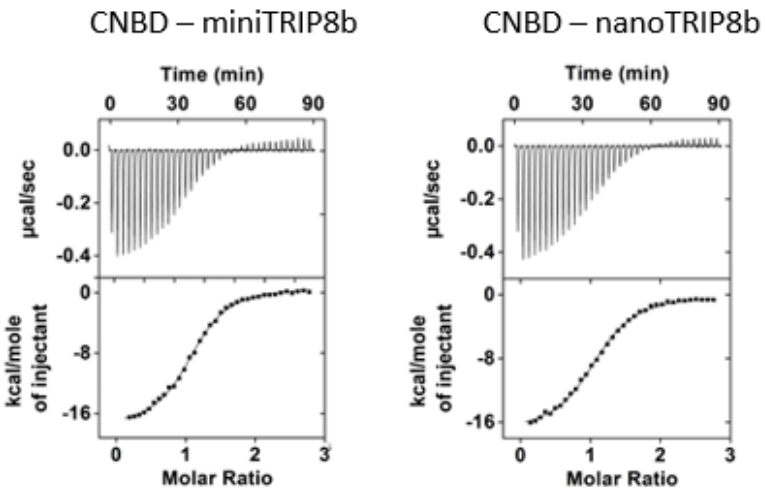

Figure 10 Top: miniTRIP8b sequence and the shorter nanoTRIP8b sequence in bold. Bottom: ITC binding of miniTRIP8b (left) and nanoTRIP8b (right) to the purified CNBD. K_D of 1.2 ± 0.1 µM for $TRIP8b_{core}$ and a K_D of 1.5 ± 0.1 µM for $TRIP8b_{nano}$. (Saponaro et al., 2017 submitted).

After the determination of the CNBD structure not bound to cAMP (Fig.5), through NMR titration it was possible to determine TRIP8b binding region on the CNBD more in detail. As shown in Fig.11, the residues, which undergo a chemical shift after TRIP8b addition, are clustered in one region which forms a continuous surface exposed to the solvent. In particular, this region is composed by the N-bundle loop and the C-helix (Fig.11) and it is solvent exposed and accessible for TRIP8b in both in the cAMP-free and cAMP-bound forms of the CNBD in its quaternary structure (Saponaro et al. 2014).

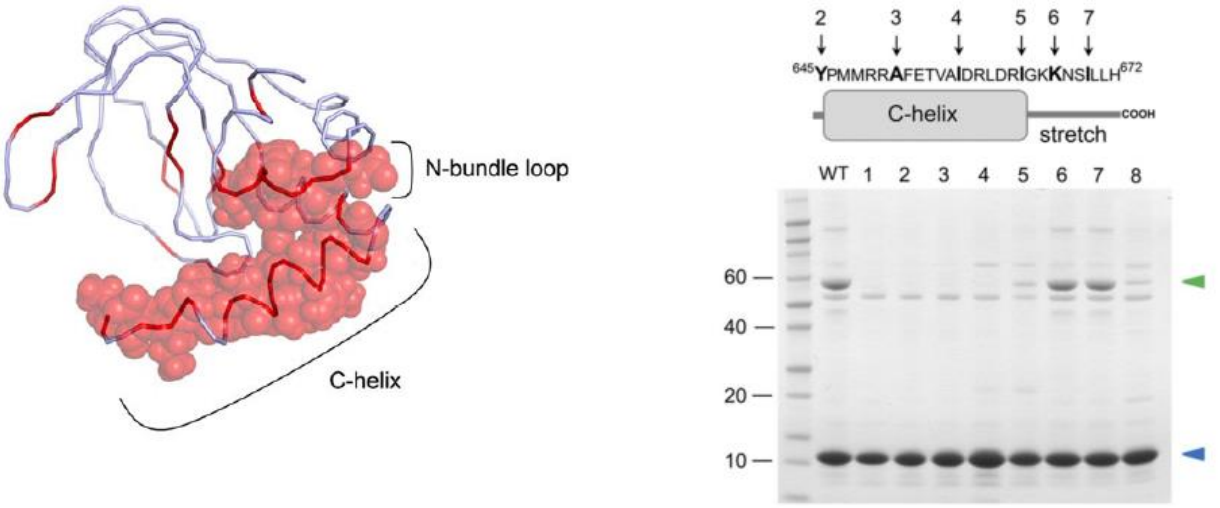

Figure 11 Left: miniTRIP8b binding region on the HCN2 CNBD. In red it is shown a ribbon representation of the CNBD residues whose amide proton (NH) signals were perturbed upon the addition of miniTRIP8b. van der Waals volumes are reported for the perturbed residues in the N-bundle loop and in the C-helix. Right: cartoon and sequence of the C-helix/stretch. Arrows show the last residue of the deletion constructs. The numbers on the arrows correspond to gel lanes. Below, SDS-PAGE of co-purifications of Strep-miniTRIP8b (blue arrowhead) with His_6-MBP–tagged CNBDWT and mutants (green arrowhead). Lane 1 contains CNBD ΔN-bundle loop, lane 2 contains CNBD ΔC-helix. Lanes 3–7 contain mutants obtained by progressive truncation of the C-helix and stretch. Lane 8 contains $K_{665}E/K_{666}E$ double-CNBD point mutant (Saponaro et al. 2014).

It was also demonstrated that both the N-bundle loop and the C-helix are required for the formation of the TRIP8b binding region (Fig.11 lanes 1 and 2) (Saponaro et al. 2014). Moreover, the deletion constructs of the C-helix revealed the importance of the two lysines in the CNBD (K_{665} and K_{666}) in complex formation (Fig.11 lane 6). In fact, the inversion of charge strongly reduced the binding of the double-mutant CNBD protein $K_{665}E/K_{666}E$ to miniTRIP8b, confirming the critical role of these two positively charged residues for the interaction (Fig.11 lane 8) (Saponaro et al. 2014).

2.7 cAMP and TRIP8b: HCN channels regulatory system

cAMP and TRIP8b have different effects on HCN channel opening and their action is mutually antagonistic. Previous electrophysiological experiments and biochemical assays showed that TRIP8b preferentially binds to the cAMP-free channels, and that its binding decreases when cAMP levels increase (Hu et al. 2013; Han et al. 2011; Saponaro et al. 2014).

After the determination of TRIP8b binding region on the CNBD (Fig.12), it was finally demonstrated that the two interactors do not compete for the same binding site on the CNBD.

cAMP and TRIP8b act through an allosteric inhibition model, in fact TRIP8b binds and stabilizes the cAMP-free conformation of the CNBD, thus antagonizing cAMP action (Saponaro et al. 2014).
cAMP and TRIP8b act to fine regulate HCN channel activity. This regulation takes place at two levels: inside the neuron and in brain regions. As a matter of fact, from cell-attached recordings on hippocampal CA1 pyramidal neurons it was seen that I_h density was 6-times higher in distal dendrites if compared to the soma. Moreover, in dendrites, I_h is more hyperpolarized than in the soma (Magee 1998). This difference is due to the regulation of cAMP and TRIP8b within the cell. TRIP8b is the responsible for the increase of I_h density and its hyperpolarized $V_{1/2}$. Where TRIP8b is present, the channel is less sensitive to cAMP and vice versa.
The fine regulation of these channels is also present in some brain regions such as the hippocampus. This one is divided in two regions: the ventral region, which is responsible for emotional behaviour, and the dorsal one involved in cognitive functions. Notably, there are differences in the dorso-ventral gradient of expression of HCN channels and TRIP8b. In earlier stages of development, there is heterogeneity in HCN channels and TRIP8b distribution in the dorsal and ventral hippocampus. TRIP8b and HCN1/2 are more expressed in the dorsal region of hippocampus with respect to the ventral one. This means that in dorsal cells, I_h is less sensitive to cAMP and vice versa in ventral cells (Fig.12A) (Marcelin, Liu, et al. 2012).
This distribution changes as hippocampal development occurs. In adult hippocampus the two isoforms of HCN channels are more expressed in the ventral region. Interestingly, TRIP8b expression is similar in both the dorsal and ventral region (Fig.12B) (Marcelin, Lugo, et al. 2012).
The meaning and the mechanism of the changes of the fine-tuned orchestration of hippocampal organization, which occur during development, are not known and remain to be determined.

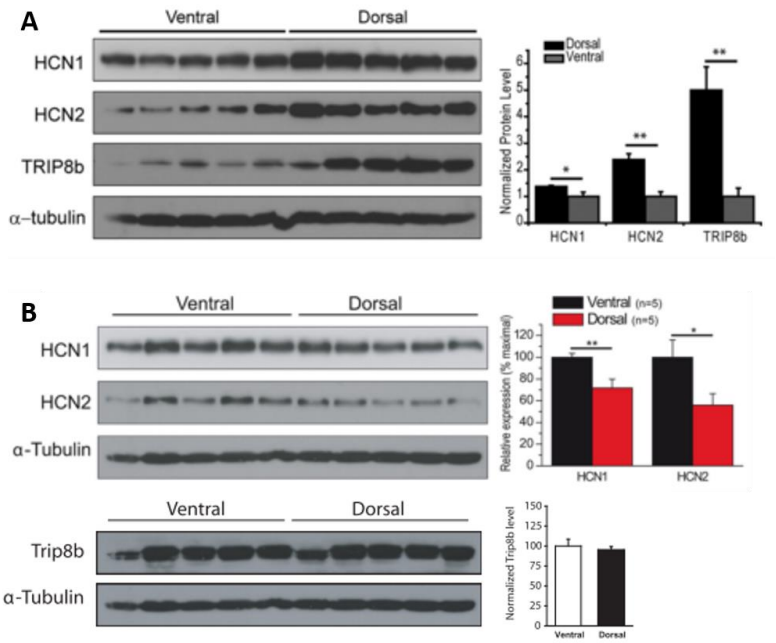

Figure 12 ***A.*** *Western blot on HCN1, HCN2 and TRIP8b protein levels in hippocampus from mice at early stages of development. HCNs and TRIP8b protein levels are larger in dorsal than ventral hippocampus* (Marcelin, Liu, et al. 2012). ***B.*** *Western blot of HCN1 and 2 (top) and TRIP8b (bottom) levels in adult mice hippocampus. The western blot shows that HCN1 and 2 protein levels are increased in the ventral hippocampus, whereas TRIP8b protein levels are similar in the dorsal and ventral hippocampi* (Marcelin, Lugo, et al. 2012).

2.8 Mint proteins

Among all the proteins known to interact with HCN channels, they were recently found to interact with Mint proteins. These are adaptor proteins which contain protein-protein interaction domains through which they mediate the assembly of functional multiprotein complexes (Rogelj et al. 2006). The Mint (X11) family is composed by three isoforms: Mint1 (or X11α) and Mint2 (or X11β) which are predominantly expressed within neurons in brain; and Mint3 (or X11γ) which is ubiquitously expressed. All three isoforms are soluble cytosolic proteins and contain a centrally located phosphotyrosine binding domain (PTB) and two contiguous C-terminal PDZ domains. PTB and PDZ are well characterized modular protein-protein interaction domains that are found in many adaptor proteins and signalling molecules. Instead, the three isoforms diverge substantially in their N-termini where a N-terminal sequence known as munc18-interacing domain (MID) is conserved in Mint 1 and 2 but not in Mint 3; moreover Mint1 (but not Mint2 and 3) binds to the presynaptic protein CASK via an N-terminal sequence CI (Fig.13) (Rogelj et al. 2006).

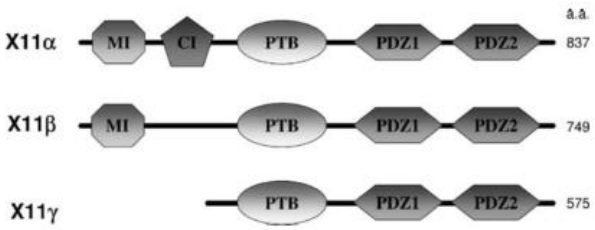

Figure 13 Schematic representation of the domains composing Mint proteins. For each isoform the amino acids number (aa) is shown on the left. MI: Munc-18 interacting domain, CI: CASK interacting region, PTB: phosphotyrosine binding domain, PDZ: PSD-95/discs large/ZO-1 domain (Rogelj et al. 2006).

Mint1 and Mint2 protein distribution are almost overlapping: Mint1 is highly expressed in the limbic structures while Mint2 is expressed throughout the brain (Nakajima et al. 2001). Moreover, Mint1 is more expressed in hippocampal inhibitory interneurons in particular in the active zone of hippocampal synapses; instead Mint2 expression pattern is somatodendritic (Nakajima et al. 2001). On the subcellular level, Mint proteins are mainly present in the trans-Golgi apparatus and also to the plasma membrane (Rogelj et al. 2006)

According to the binding partners, this family of protein has several functions such as for example synaptic vesicle docking and exocytosis, protein transport and trafficking and copper homeostasis (Rogelj et al. 2006).

The study of Mint proteins has become central in Alzheimer's disease (AD). In fact, Mint1/Mint2 proteins are known to directly bind the cytoplasmic tail of amyloid precursor protein (APP) through their PTB domain. This binding is important to regulate APP trafficking and, notably also its cleavage, and thus β-amyloid peptide (Aβ) production (Rogelj et al. 2006).

The interaction between HCN channels and Mint proteins was tested by means of immunoprecipitation assays. In particular, it was shown that HCN1 interacts with both Mint1 and 2 from murine cortex and EC (Entorhinal Cortex)-rich brain samples; and HCN2 interacts with Mint2 both in rat brain and transfected COS7 cells (Saito et al. 2012; Kimura et al. 2004).

Moreover, HCN2 and Mint2 interaction was studied in order to understand the protein regions important for the binding. By means of deletion mutants and pull-down assays, it was shown that Mint2 can bind to HCN2 via an interaction between the N-terminal MID domain (Fig.14 left) and the very C-terminal region of HCN2 (Fig.14 right), downstream of the C-helix of the CNBD (Kimura et al. 2004).

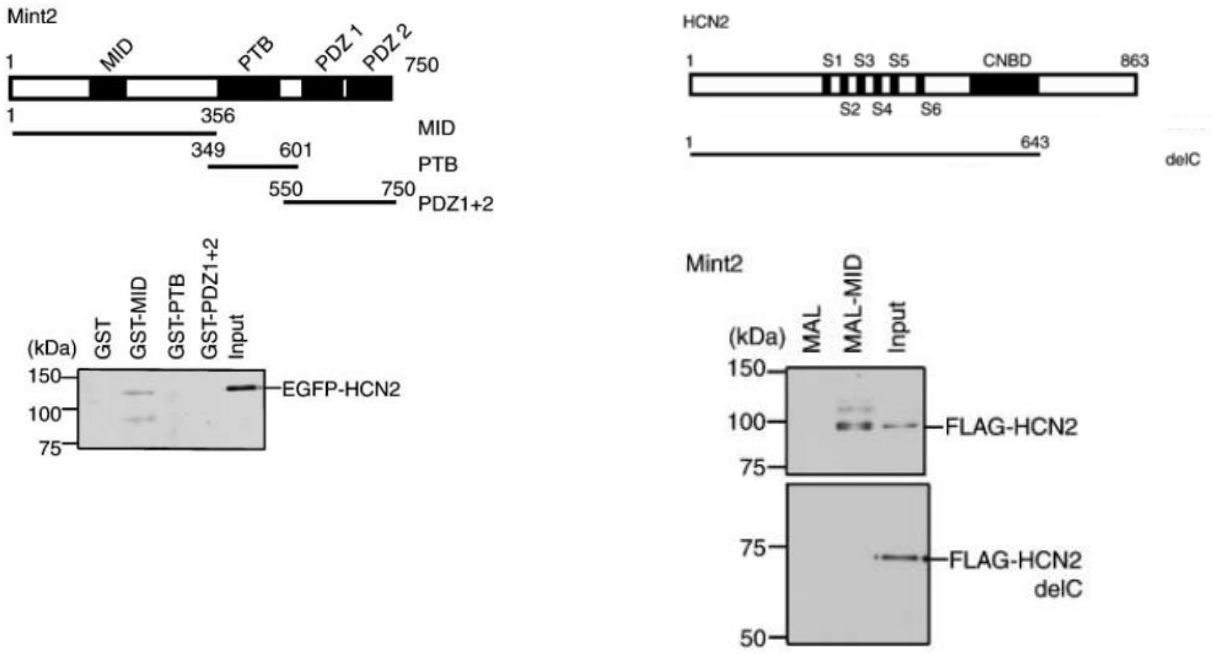

Figure 14 Identification of HCN2 and Mint2 interaction region by pull-down assays.

Left top: The MID, PTB and PDZ1 and 2 domains of Mint2 fused to GST are indicated below with a schematic structure of rat Mint2.

Left bottom: GST, GST-MID, GST-PTB and GST-PDZ1 and 2 were immobilized on glutathione- Sepharose 4B beads and incubated with EGFP-HCN2 expressed in COS-7 cells. Bound proteins were detected by immunoblotting with anti-EGFP antibody.

Right top: Schematic structures of rat HCN2 and its deletion mutant (delC) used for pull-down assays are indicated; S1-S6 arerepresent the six transmembrane segments of HCN2.

Right bottom: Maltose binding protein (MAL) and MAL-MID were immobilized on amylose resin and incubated with FLAG-HCN2 or FLAG-HCN2 delC expressed in COS-7 cells. The ability of HCN2 and HCN2 delC to bind to MAL- MID was tested by immunoblotting with anti-FLAG antibody (Kimura et al. 2004).

Finally, it was reported that HCN impairment is involved in the aberrant production of Aβ both in mice cortex and N2a cells. Moreover, it was shown that the increase in Aβ generation depends on the decrease in HCN channel activity, in fact the inhibition of HCN channels by means of a specific channel blocker (ZD7288) can affect the rate of APP processing and Aβ production (Fig.15) (Saito et al. 2012).

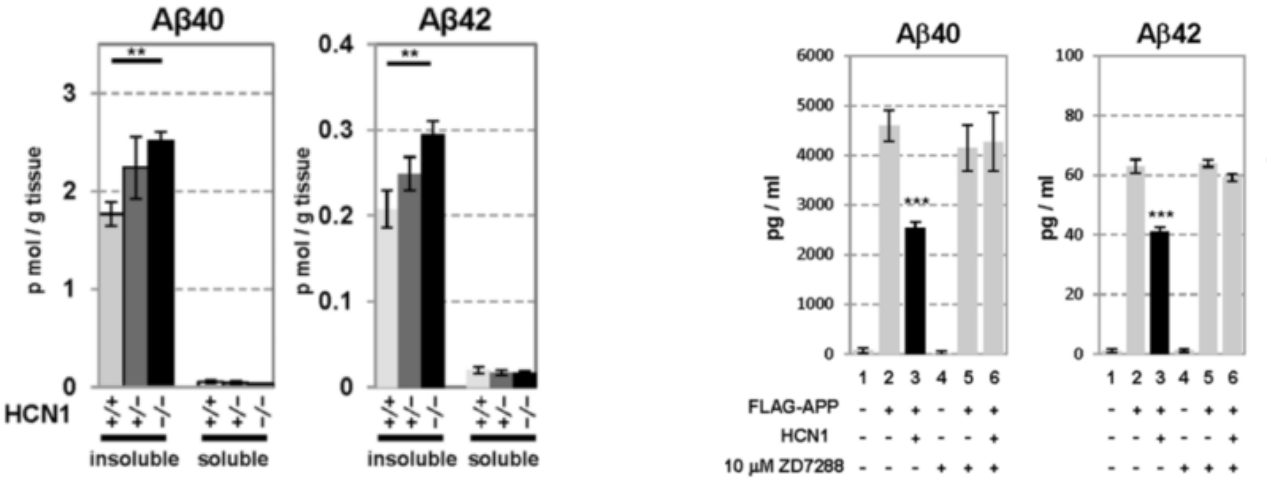

Figure 15 Aβ generation is facilitated by deficits in HCN1 channel activity. ***A.*** *Quantification of endogenous murine Aβ40 and Aβ42 in the cortex of 4-month-old HCN1+/+, HCN1+/-, and HCN1-/- mice with ELISA system.* ***B.*** *Quantification of Aβ40 and Aβ42 secreted in the medium by N2a cells with the sELISA system. FLAG-APP or FLAG-APP and HCN1 were transiently overexpressed in the cells with (+) or without (−)10 μM of the channel blocker ZD7288* (Saito et al. 2012).

3. AIMS OF THE PROJECT

My PhD project was focused on the study of the interaction of HCN channels with other two proteins: TRIP8b and Mint proteins.

For what it concerns the interaction between HCN channels and TRIP8b, it was already known that the N-bundle loop and the C-helix together composed a continuous and solvent-exposed surface accessible to TRIP8b both in the cAMP-bound and unbound configuration (Saponaro et al. 2014).

In this region, a double mutation ($K_{665}E/K_{666}E$) in the C-helix was able to affect complex formation and at the same time the affinity for the cyclic nucleotide (Saponaro et al. 2014). On this background, at first the aim of my work was to understand which of the two lysines was the responsible for the binding of TRIP8b, then to find other residues important for TRIP8b binding both in the N-bundle loop and in the C-helix. The ultimate goal was to obtain an HCN2 mutant unable to interact with TRIP8b. This could be use *in vivo* in order to understand the physiological role of the regulation of this important β subunit in brain.

For what it concerns the interaction of HCN channels with Mint proteins, very little was known. The aim of my work was to characterize this interaction. In particular, I analysed the effect of Mint proteins on HCN channels properties, and then I began to identify the regions important for the interaction.

4. MAIN RESULTS

4.1 HCN-TRIP8b INTERACTION

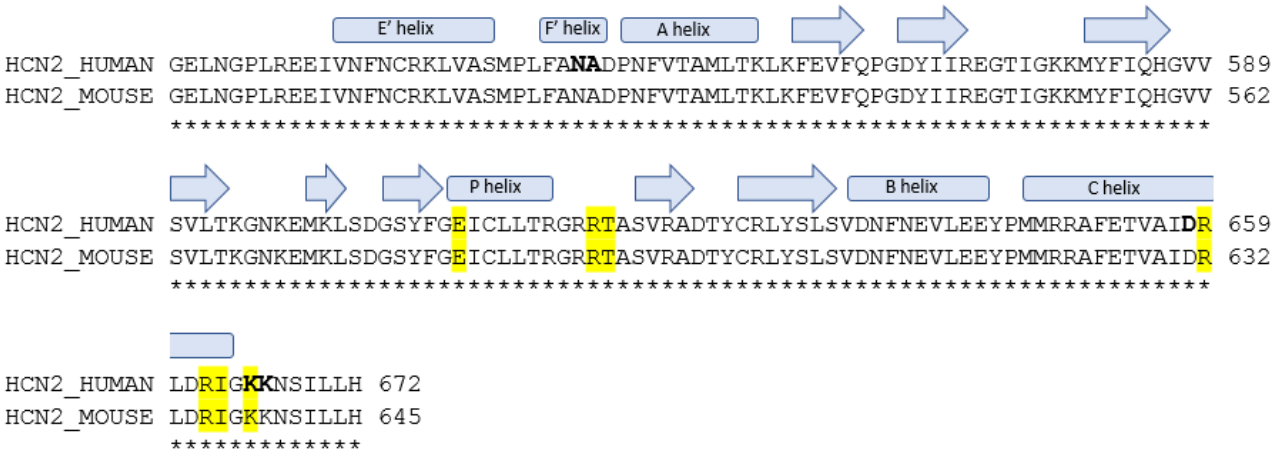

Figure 16 Sequence alignment of the CNBD construct from human (used for the experiments) with the one from mouse (shown in Par. 2.4). Secondary structures are represented by rectangles (α helices) and arrows (β strands). Secondary structure is based on Lee & Mackinnon 2017. The residues in bold are those that will be mutated in the following experiments. The residues in yellow are those important for cAMP affinity (shown in Par. 2.4, L. Zhou and S. Siegelbaum 2007).

4.1.1 Mutations in the C-helix

In order to find residues important for complex formation, I decided to introduce point mutations in the C helix, which is the largest region composing TRIP8b binding site.

As shown in Figure 11 (lane 8), the double mutant in the C-helix (mutant $K_{665}E/K_{666}E$) had a lower affinity for miniTRIP8b, but at the same time, the inversion of these two positive charges caused a decrease in cAMP affinity (Saponaro et al. 2014). In order to understand which of the two lysines was involved in the interaction, I mutated the two lysines in glutamates singolarly.

I tested whether the presence of the mutation influenced complex formation through a direct biochemical assay. I co-expressed in *E. coli* the HCN2 CNBD tagged with the His_6-MBP (Maltose Binding Protein) sequence (His_6-MBP-CNBD) wild-type or mutated with the miniTRIP8b fragment fused to the Strep sequence. The complex was purified with streptavidin column which binds miniTRIP8b. The results of the purification was analysed by SDS-PAGE; in this way it was possible to evaluate the effects of the mutations on the formation of a stable complex between the two partner proteins.

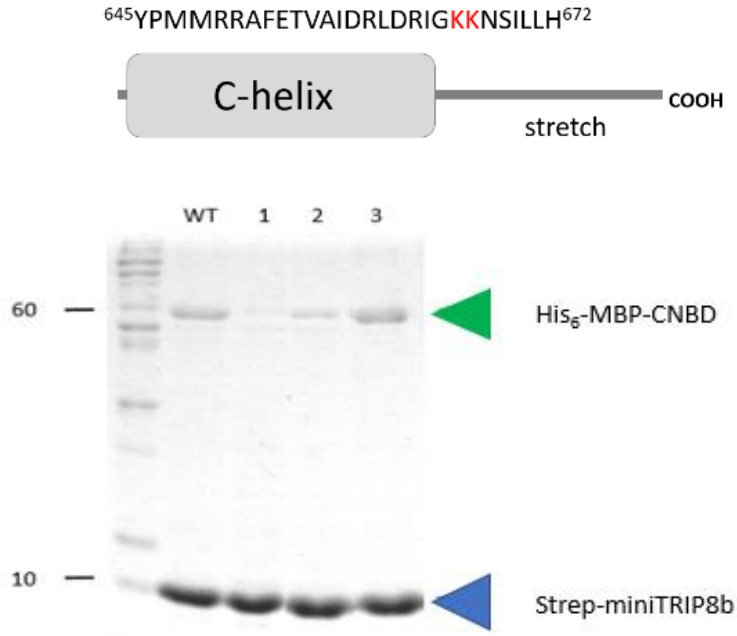

Figure 17 Upper part: Sequence and cartoon representation of the C-helix/stretch. The two lysines (K_{665} and K_{666}) are shown in red. Bottom part: SDS-PAGE of the co-purification of miniTRIP8b and His_6-MBP-CNBD wild-type or mutant. WT = CNBD wild-type, lane 1 = CNBD double mutated $K_{665}E/K_{666}E$, 2 = CNBD $K_{665}E$, 3 = CNBD $K_{666}E$. Numbers on the left indicates the molecular weight (KDa) of the marker (Novex® Sharp Pre-stained Protein Standards, Invitrogen). The green arrowhead indicates the His_6-MBP-CNBD protein, whereas the blue one indicates the strep-miniTRIP8b.

In figure 17, the results of the co-expression and co-purification assays are shown. The single mutation $K_{665}E$ (lane 2) strongly decreases the interaction between the two proteins; even though the reduction cannot be compared to the one caused by the double mutant $K_{665}E/K_{666}E$ (compare lane 1 and 2). On the contrary, the single mutation $K_{666}E$ does not affect the complex formation (lane 3). This results show that the first of the two lysines has a major role in the interaction between the CNBD and miniTRIP8b, even though it can not be excluded that also the second lysine has a role since the double mutant has a stronger effect with respect to the single $K_{665}E$ mutant. As already shown in paragraph 2.4, K_{665} residue is important for miniTRIP8b binding, but also for cAMP. As a matter of fact, the double mutant $K_{665}E/K_{666}E$ showed a reduced cAMP affinity, due to the mutation of the first lysine (as shown in L. Zhou and S. Siegelbaum, 2007).

I then focused on the region of the C-helix (DRLDRI, highlighted in red in Fig.18) which could restore a weak binding with miniTRIP8b in the deletion mutant screening (Fig.18, lane 5).

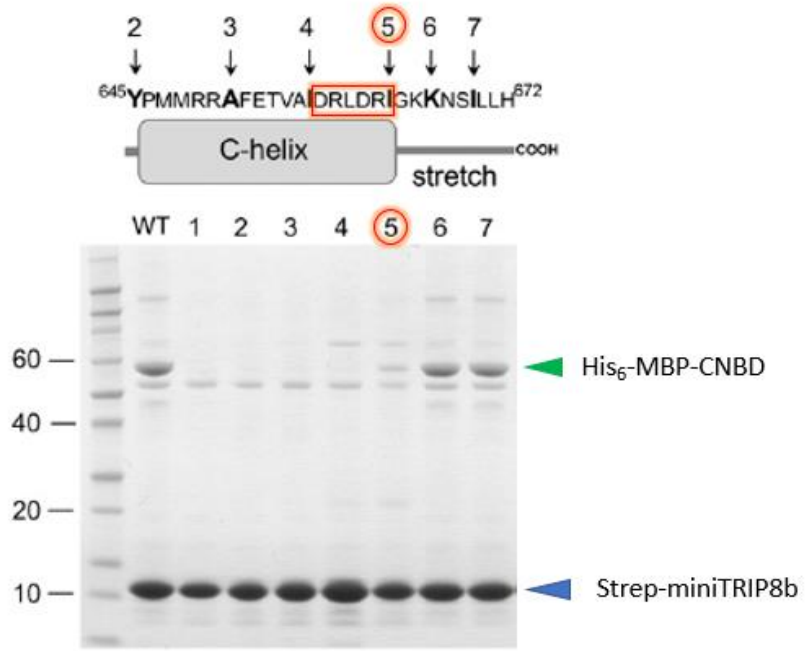

Figure 18 Cartoon and sequence of the C-helix/stretch. Arrows indicate the last residue of the deletion constructs. The numbers on the arrows correspond to gel lanes. Below, SDS-PAGE of co-purifications of Strep-miniTRIP8b (blue arrowhead) with His_6-MBP–tagged CNBDWT and mutants (green arrowhead). Lane 1 contains CNBD ΔN-bundle loop, lane 2 contains CNBD ΔC-helix. Lanes 3–7 contain mutants obtained by progressive truncation of the C-helix and stretch. In red the interested sequence and gel lanes are highlighted (modified from Saponaro et al. 2014).

This region of the C-helix contains several residues (R_{659}, R_{662}, I_{663} and K_{665}) that have been previously shown to be involved in cAMP binding (highlighted in red in Fig.19) (L. Zhou and S. Siegelbaum 2007). I therefore excluded them not to affect the affinity for the cyclic nucleotide. In particular, in this region I focused on D_{658} (highlighted in blue in Fig.19, left side) whose lateral chain is solvent exposed in the CNBD bound structure (Fig.19 righ side).

To test the importance of this residue for TRIP8b binding, it was mutated in arginine, thus reversing its charge.

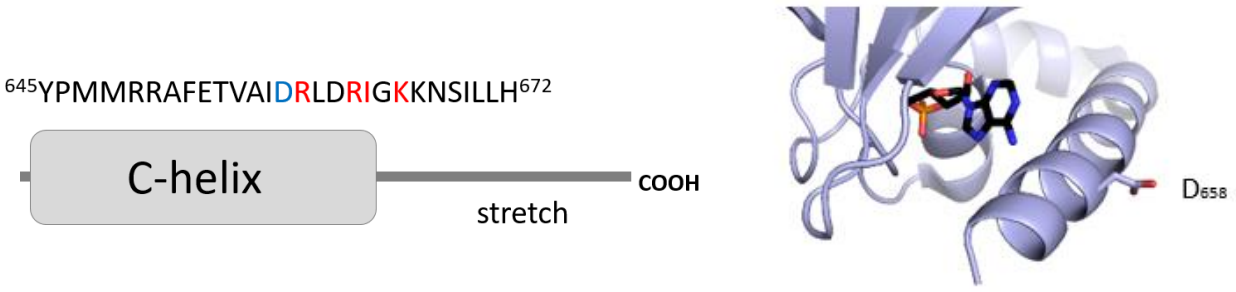

Figure 19 Left: sequence and cartoon representation of the C-helix/stretch. In red: residues important for cAMP affinity (L. Zhou and S. Siegelbaum, 2007) and in blue D_{658} residue.

Right: Ribbon representation of C-terminal part of the cAMP-bound structure (Zagotta et al. 2003). *The cAMP molecule and D_{658} are shown in stick representation.*

As shown in figure 20, the presence of the mutation decreased the interaction between the two proteins when tested as previously in *E. coli* (green arrowhead).

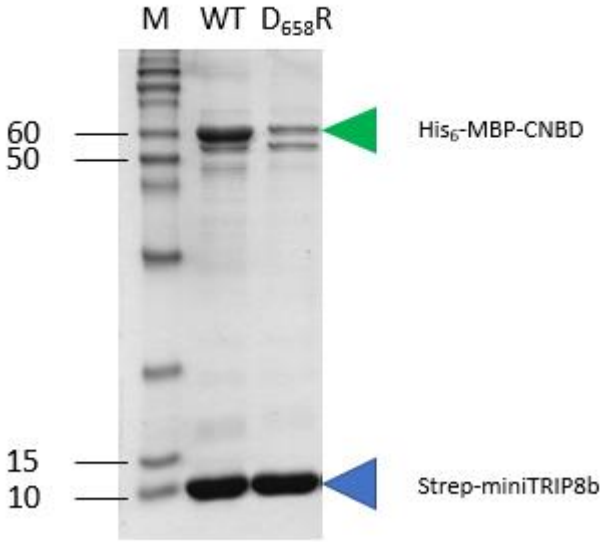

Figure 20 SDS-PAGE of the co-purification of strep-miniTRIP8b with His_6-MBP-CNBD wild-type and mutant $D_{658}R$. M = marker Novex® Sharp Pre-stained Protein Standards, Invitrogen), WT = CNBD wild-type, $D_{658}R$ = CNBD $D_{658}R$. Numbers on the left indicate the molecular weight (KDa) of the marker. The green arrowhead indicates the His_6-MBP-CNBD protein, whereas the blue one indicates the strep-miniTRIP8b.

An unchanged cAMP affinity of the mutant CNBD is an essential requirement in this study since the ultimate goal is to find a mutation that abolishes TRIP8b binding without affecting the capability of the protein to bind cAMP. Therefore, I tested the affinity of this mutant for both cAMP and nanoTRIP8b (paragraph 2.6 Fig.10) by means of Isothermal Titration Calorimetry (ITC) technique.

To this aim, I purified the CNBD both wild-type and mutated (His_6-MBP-HCN2 CNBD) which was titrated with cAMP or nanoTRIP8b. From the ITC measurements, it is possible to obtain the stoichiometry (N) and the Kd of the reaction. Table 1 shows no appreciable difference in the affinity of the wild-type CNBD with respect to the mutated one. The measured Kd for cAMP of the wild-type was 1.51 µM and the Kd of the mutated CNBD was 1.40 µM. Moreover, the stoichiometry of the reaction is 1 for both the purified proteins, confirming our empirical observation that the mutation did not induce protein aggregation and/or precipitation, which are symptomatic of protein misfolding.

His_6-MBP-HCN2 CNBD	Kd ± SEM (μM)	N ± SEM	n
WT	1,51 ± 0,09	1,04 ± 0,01	3
$D_{658}R$	1,4 ± 0,09	1,13 ± 0,03	3

Table 1 ITC measurements of the binding between His_6-MBP-CNBD wild-type and mutated ($D_{658}R$) with cAMP.

Then I tested the affinity of the mutated CNBD for nanoTRIP8b. From the ITC measurements (table 2), neither the stoichiometry of the reaction nor the Kd change, meaning that the mutation has no effect on nanoTRIP8b affinity.

His_6-MBP-HCN2 CNBD	Kd ± SEM (μM)	N ± SEM	n
WT	1,24 ± 0,05	1,1 ± 0,01	3
$D_{658}R$	1,19 ± 0,09	1,1 ± 0,03	3

Table 2 ITC measurements of the binding between His_6-MBP-CNBD wild-type and mutated ($D_{658}R$) with nanoTRIP8b.

4.1.2 Looking for alternative mutations: the single point mutation $N_{547}D$ in the N-bundle loop

Since I could not find residues important for TRIP8b binding in the C-helix without affecting the affinity for cAMP ($K_{665}E/K_{666}E$ double mutant), I focused on the N-bundle loop, the loop that connects helix E' and helix A in the N-helical bundle of the CNBD (see Figure 21A). This region is short and it is composed by 8 aminoacids: PLANADP. In order to find residues important for complex formation, I decided to produce point mutations in this region that our previous analysis indicated as a second interaction site for miniTRIP8b (Saponaro et al. 2014). During the screening, I did not mutate the two lateral prolines (P_{543} and P_{550} in Fig.20A) because from preliminary data they were found to be important for protein structure. Moreover, also phenylalanine and leucine were not mutated (Fig.21A): the lateral chain of these two hydrophobic residues points towards the core of the protein and mutations could affect protein structure.

To understand which residues were important for TRIP8b binding, the N-bundle loop sequence of HCN channels was aligned with the one from CNG channels. The latter are ionic channels with a CNBD and, differently from HCN, they are only regulated by cyclic nucleotides, while the voltage sensor, which is nonetheless present, does not control pore opening. Importantly in this context,

they are not regulated by TRIP8b (as shown in Santoro et al. 2004). Comparing the two sequences (Fig.21 panel B), it is clear that most of the residues are either identical (FA) or the mutations are conservative (I→L, E→D) except for the negative charge of the aspartate of CNG channels which is absent in HCN channels and for the cysteine that is an alanine in CNG. I first mutated the asparagine in aspartate ($N_{547}D$ mutant).

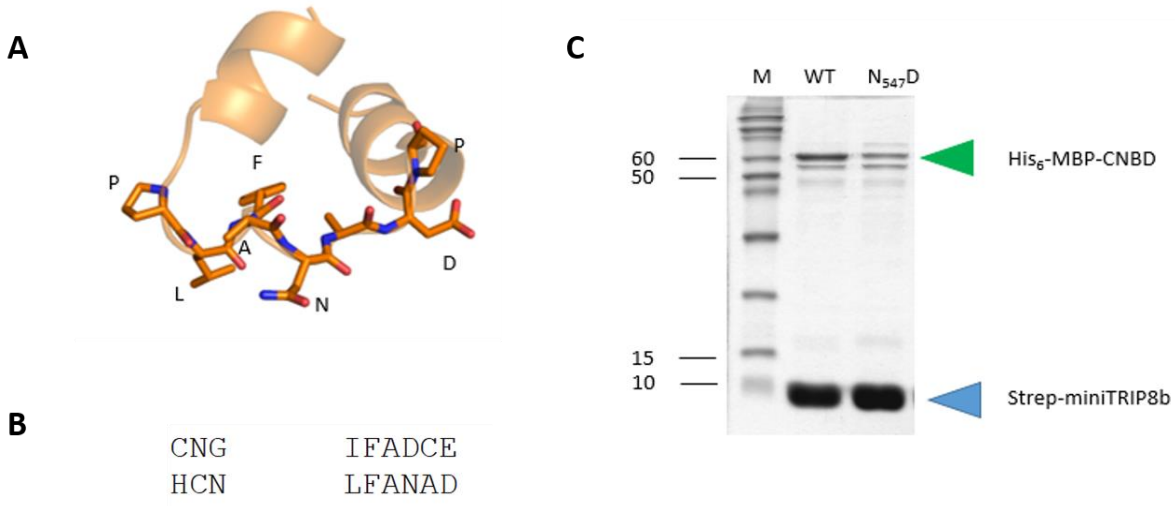

Figure 21 ***A.*** *Cartoon of the N-bundle loop and the lateral chain of its residues (structure from Saponaro et al., 2014).* ***B.*** *Alignment between HCN and CNG channels at the level of the N-bundle loop (the two lateral prolines are not shown)* ***C.*** *SDS-PAGE of the co-purification purification of strep-miniTRIP8b with His_6-MBP-CNBD wild-type and mutant $N_{547}D$. M = marker Novex® Sharp Pre-stained Protein Standards, Invitrogen), WT = CNBD wild-type, $N_{547}D$ = CNBD $N_{547}D$. Numbers on the left indicate the molecular weight (KDa) of the marker. The green arrowhead indicates the His_6-MBP-CNBD protein, whereas the blue one indicates the strep-miniTRIP8b.*

Again, to evaluate whether this residue was important for complex formation, I used the co-expression and co-purification assay. As shown in Fig.21C, the presence of the mutation $N_{547}D$ is able to reduce the interaction between the two proteins in *E.coli* (green arrowhead).

Since this residue was important for complex formation, I also tested the affinity of this mutant for cAMP by means of ITC technique. As shown in table 3, the presence of the mutation does not seem to affect the folding of the protein since the stoichiometry of the reaction (N) is close to 1. However, the introduction of the negative charge in the N-bundle loop influences cAMP affinity: the Kd of the mutant is increased with respect to the wild-type protein almost 4 folds from 1,4 µM of the wild-type to 5,5 µM of the mutant.

His_6-MBP-HCN2 CNBD	Kd ± SEM (µM)	N ± SEM	n
WT	1,4 ± 0,1	1,06 ± 0,09	3
$N_{547}D$	5,5 ± 0,4	0,85 ± 0,01	3

Table 3 ITC measurements of the binding between His_6-MBP-CNBD wild-type and mutated ($N_{547}D$) with cAMP.

4.1.3 The double mutant $N_{547}D/A_{548}C$

The insertion of a negative charge to replace the asparagine in the N-bundle loop (mutant $N_{547}D$) decreased cAMP affinity. Considering the alignment with CNG channels (Fig.21B), the aspartate in CNG is followed by a cysteine, instead of alanine for HCN channels (Fig.21B). I therefore introduced in the single mutant ($N_{547}D$) a second mutation ($A_{548}C$), to match the sequence in the CNG channels (Fig.22 left).

The effect of the double mutation $N_{547}D/A_{548}C$ on the interaction with miniTRIP8b was first tested by co-expression and co-purification assay in *E.coli*. The presence of the mutations decreased the complex formation to the same extent of the single mutation $N_{547}D$ (Fig.22 right, green arrowhead).

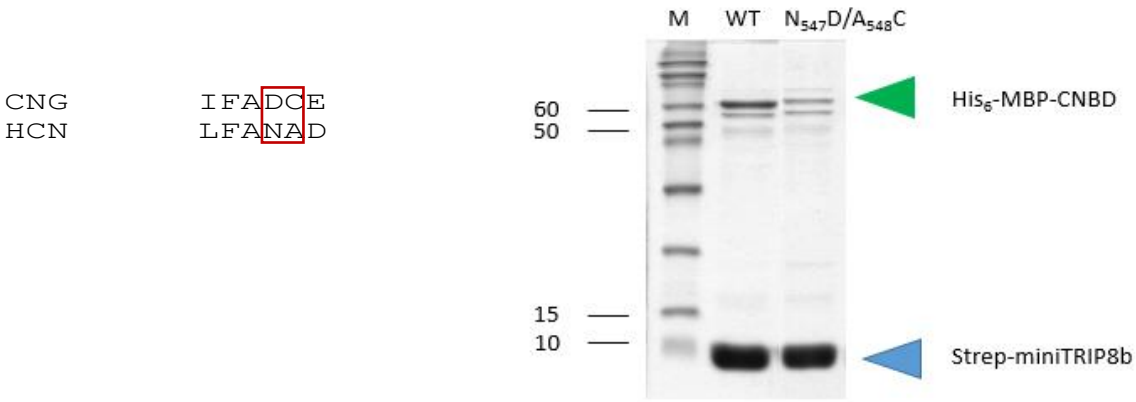

Figure 22 Left: sequence alignment of the N-bundle loop of CNG and HCN channels.
Right: SDS-PAGE of the co-purification purification of strep-miniTRIP8b with His_6-MBP-CNBD wild-type and mutant $N_{547}D/A_{548}C$. M = marker (Novex® Sharp Pre-stained Protein Standards, Invitrogen), WT = CNBD wild-type, $N_{547}D/A_{548}C$ = CNBD $N_{547}D/A_{548}C$. Numbers on the left indicate the molecular weight (KDa) of the marker. The green arrowhead indicates the His_6-MBP-CNBD protein, whereas the blue one indicates the strep-miniTRIP8b.

The double mutant was further studied by ITC for cAMP binding. As shown in table 4, the stoichiometry of the reaction is almost 1, meaning that the presence of the double mutation does not

disturb the proper folding of the purified protein. Moreover, the Kd for cAMP binding does not change with respect to the wild-type: 1.4 µM for the wild-type and 1 µM for the mutant CNBD.

His_6-MBP-HCN2 CNBD	Kd ± SEM (µM)	N ± SEM	n
WT	1,4 ± 0,1	1,16 ± 0,01	3
$N_{547}D/A_{548}C$	1 ± 0,1	1,1± 0,01	3

Table 4 ITC measurements of the binding between His_6-MBP-CNBD wild-type and mutated ($N_{547}D/A_{548}C$) with cAMP.

At this point, I could test the ability of the double mutant to bind nanoTRIP8b. As shown in table 5, the Kd of the double mutant for nanoTRIP8b is almost eight times higher with respect to the wild-type one (wild-type=1.2 µM and mutant=9.3 µM), meaning that the mutation decreased nanoTRIP8b affinity efficiently without disturbing cAMP affinity.

His_6-MBP-HCN2 CNBD	Kd ± SEM (µM)	N ± SEM	n
WT	1,2 ± 0,1	1,1 ± 0,01	3
$N_{547}D/A_{548}C$	9,3 ± 0,9	0,84 ± 0,02	3

Table 5 ITC measurements of the binding between His_6-MBP-CNBD wild-type and mutated ($N_{547}D/A_{548}C$) with nanoTRIP8b.

4.1.4 Electrophysiological characterization of mutant $N_{547}D/A_{548}C$

The double mutation $N_{547}D/A_{548}C$ was introduced on the full length HCN1 channel and characterized in HEK cells by means of patch clamp technique in the presence of TRIP8b (measurements performed by Dr. Porro).

I have chosen HCN1 (human isoform) because it is the most expressed isoform in the CA1 pyramidal neurons of the hippocampus. Among the TRIP8b splicing variants, I have used TRIP8b(1a-4) which is also the most expressed isoform in CA1 pyramidal neurons. The effect of TRIP8b(1a-4) was evaluated both on channel trafficking and gating. Co-expression of wild-type HCN channel with TRIP8b(1a-4) results in an increase of total current due to the trafficking effect of TRIP8b (Santoro et al., 2009). The second effect of TRIP8b on channel gating results in a left-shift of about 7 mV of the channel activation curve (Lewis et al. 2009) due to its competition with cAMP for the binding to the CNBD. This effect should be prevented by the double mutation if it

efficiently inhibits TRIP8b binding to the CNBD also on the full length (and tetrameric) form of the channel.

Both HCN1 wild-type (control) and mutated channel were expressed in HEK293T cells with and without TRIP8b(1a-4). Figure 23 shows exemplary activation curves recorded from single cells (Fig. 23 panels A and B) and the average values from 8 cells of the half activation potentials ($V_{1/2}$) obtained from the curves (panel C).

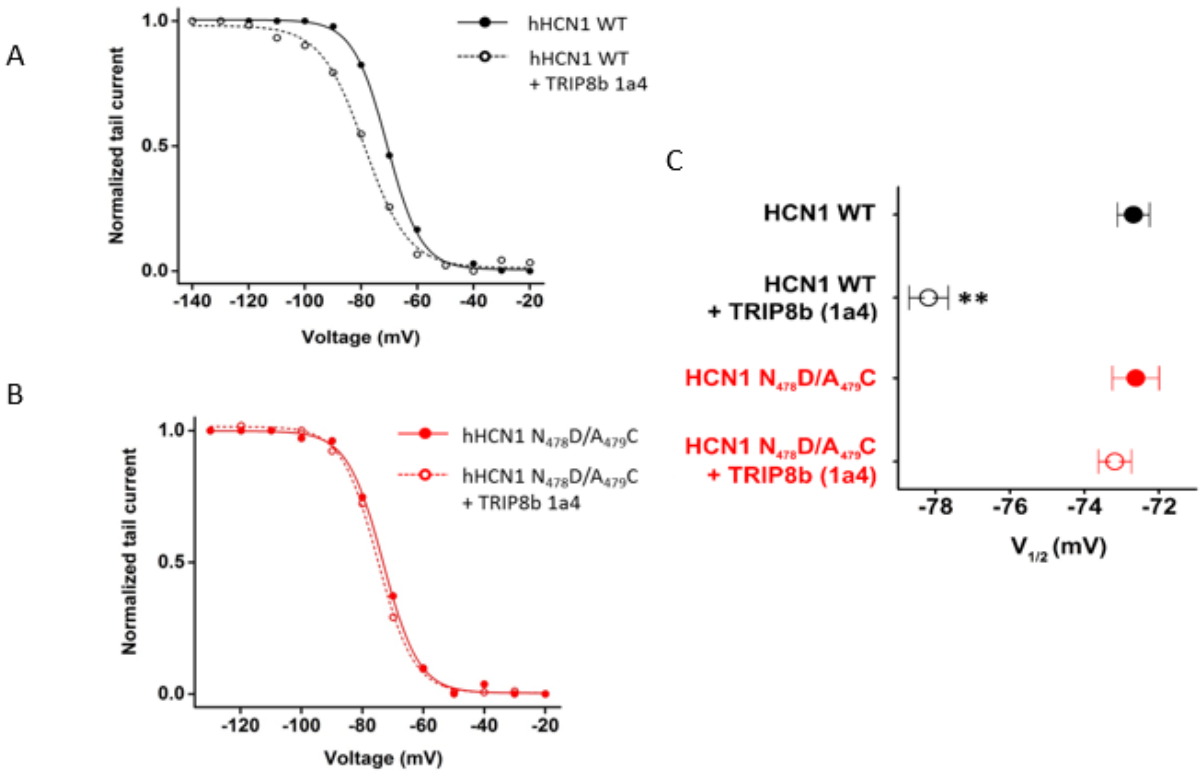

Figure 23 ***A.*** *Mean tail current activation curves of hHCN1 wild-type (black filled line and circles) and hHCN1 wild-type co-expressed with TRIP8b(1a-4) (black open circles and dotted line). Lines show fits of a Boltzmann function.* ***B.*** *Mean tail current activation curves of hHCN1 $N_{478}D/A_{479}C$ (red filled line and circles) and hHCN1 $N_{478}D/A_{479}C$ co-expressed with TRIP8b(1a-4) (red open circles and dotted line). Lines show fits of a Boltzmann function.* ***C.*** *Half activation potential ($V_{1/2}$) of hHCN1 WT and $N_{478}D/A_{479}C$ mutant alone or co-expressed with TRIP8b (1a4). hHCN1 WT (black filled circle, $V_{1/2}$ = -72.7 ± 0.4 mV, n=8); hHCN1 WT + TRIP8b (1a4) (black open circle, $V_{1/2}$ = -78.2 ± 0.5 mV, n=8); hHCN1 $N_{478}D/A_{479}C$ (red filled circle, $V_{1/2}$ = -72.6 ± 0.6 mV, n=8); hHCN1 $N_{478}D/A_{479}C$ + TRIP8b (1a4) (red open circle, $V_{1/2}$ = -73.2 ± 0.4 mV, n=8). Statistical analysis was performed with ANOVA, **=P < 0.01. (Saponaro et al., 2017 submitted).*

In figure 23A, the activation curves of the channel alone (black filled circles) and co-expressed with TRIP8b(1a-4) (black open circles) are shown normalized and superimposed. Fitting the data with a Boltzmann equation yielded the value of half activation potential ($V_{1/2}$) of -72.7 mV for hHCN1

channel alone and of -78.2 mV when co-expressed with TRIP8b isoform. Co-expression of TRIP8b(1a-4) caused a shift of the activation curve of the channel towards more negative potentials. The shift is, in this case, 5.5 mV. On the contrary, the co-expression of TRIP8b with the mutant channel $N_{547}D/A_{548}C$ did not result in a shift in the activation curve (Fig.22B and C). The shift observed in the wild-type is due to the fact that the presence of TRIP8b inhibits the binding of endogenous cAMP to the channel CNBD, as demonstrated by an independent experiment in which HCN1 was not able to bind cAMP due to the insertion of another mutation $R_{549}E$ in the cAMP binding pocket (data not shown, Saponaro et al, 2017 submitted). This confirms that the mutation inhibits the control exerted by TRIP8b on the cAMP effect, probably because of the decreased affinity of TRIP8b binding to the N-bundle loop of the CNBD. Moreover, as shown in Fig.23C, the $V_{1/2}$ of the wild-type and mutated channels alone (black and red filled circles) are similar, meaning that the mutated channel has an unaffected capability to bind to the endogenous cAMP, and thus confirming the ITC measurements on the CNBD proteins (table 4).

Finally, the current density of both the channels in the presence and absence of their interactor TRIP8b were analysed. As sown in Fig.24, the co-expression of both channels caused an increase in the maximal current density of about 2.5 fold. This result indicates that, notwithstanding the presence of the mutation ($N_{547}D/A_{548}C$), the channel is still able to interact at the downstream binding site and thus TRIP8b is still able to regulate channel trafficking to the plasma membrane.

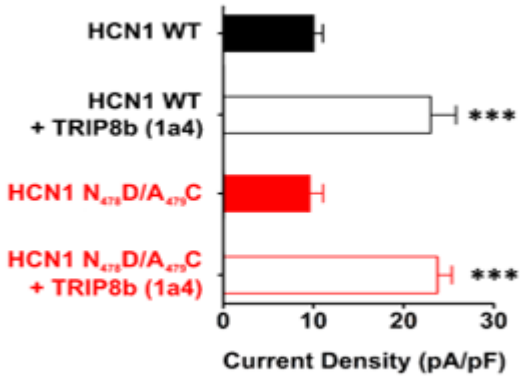

*Figure 24 Current density (pA/pF) of hHCN1 WT and $N_{478}D/A_{479}C$ mutant alone or co-expressed with TRIP8b (1a4). hHCN1 WT (black filled histogram, 10.1 ± 2.7 pA/pF); hHCN1 WT + TRIP8b (1a4) (black open histogram, 23 ± 8 pA/pF); hHCN1 $N_{478}D/A_{479}C$ (red filled histogram, 9.6 ± 4 pA/pF); hHCN1 $N_{478}D/A_{479}C$ + TRIP8b (1a4) (red open histogram, 23.8 ± 4.5 pA/pF). The number of cells (n) is 8. The statistical analyses was performed with ANOVA, ***= P < 0.001. (Saponaro et al., 2017 submitted).*

4.2 HCN-MINT INTERACTION

4.2.1 Effect of Mint proteins on HCN channels

For what it concerns the interaction between HCN channels and Mint proteins, less is known compared to TRIP8b. In fact, two paper showed the interaction by co-immunoprecipitation assays (Saito et al. 2012; Kimura et al. 2004) but no one ever investigated the effects and functionality of this interaction. For this reason, I started the characterization of this new interaction by testing the effect of Mints on HCN channel properties and then I focused on the study of the binding regions.
In order to understand whether the presence of Mint proteins had an effect on channel properties, two different isoforms of the channel (mouse HCN1 or HCN2) were co-expressed with two rat isoforms of Mints (Mint1 or Mint2) fused to the EGFP protein. The clones were co-expressed in HEK293T cells for patch clamp recordings of the currents (measurements performed by Dr. Porro).
In control experiments, the channels expressed in the absence of Mints were co-transfected with an equal amount of EGFP cDNA.
Figure 25 shows an exemplary family of currents recorded with the indicated voltage protocol (materials and methods) form a cell transfected with mHCN1 alone (panel A, left) and co-transfected with EGFP-Mint1 (panel A, right). The presence of Mint induced a sharp reduction (2.3 folds at the reference potential of -100 mV) in the current values at all voltages, as shown by the current/voltage relationship (I/V curve) in panel B. In this graph, the Y axis shows the current normalized for the cell capacitance to obtain the current density. A similar, although somewhat stronger, reduction was observed when HCN1 was co-transfected with EGFP-Mint2 (panel C). In this case the average reduction in current was about 6.5 fold (recorded at – 100 mV).

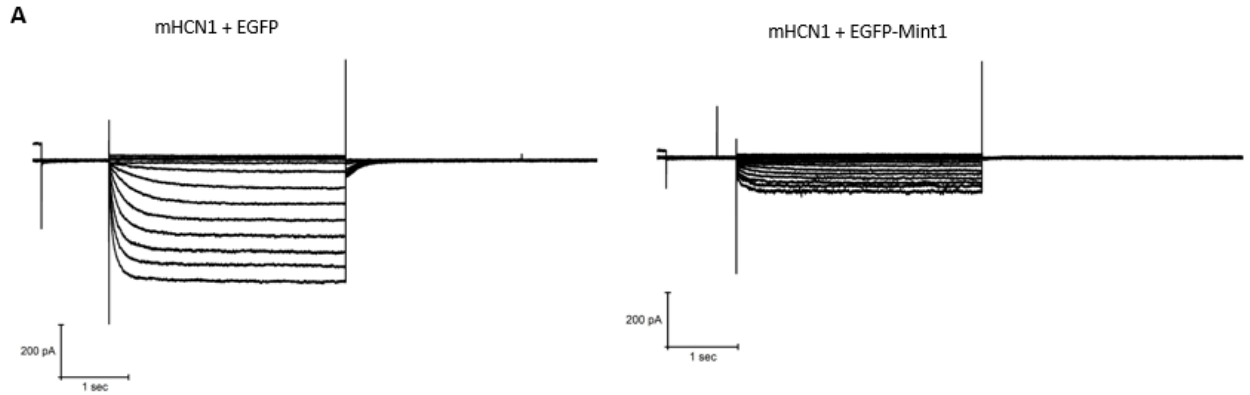

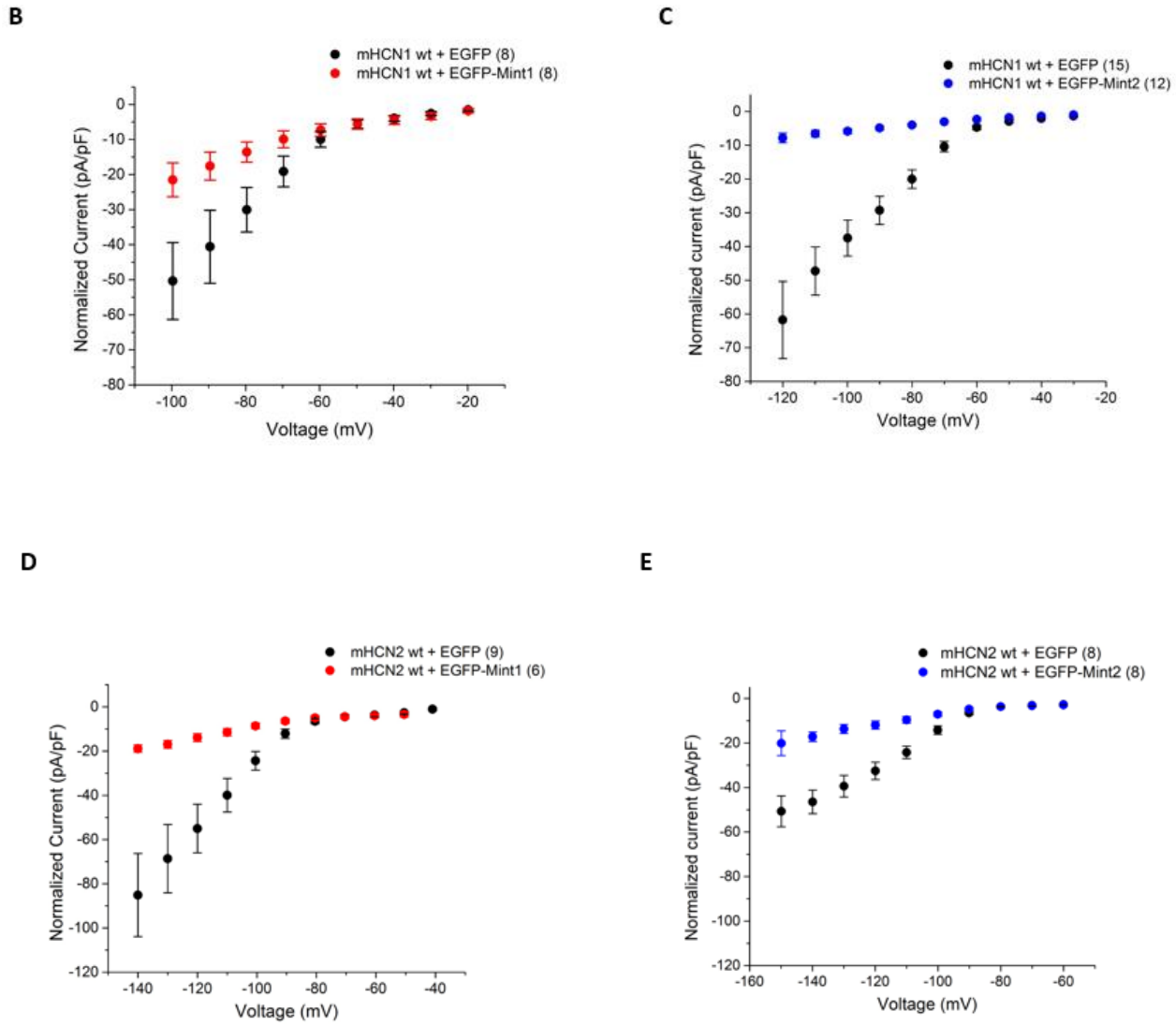

Figure 25 Effects of Mint proteins co-expression on mHCN1 and 2 channels. ***A.*** *Representative currents recorded from HEK293T cells transiently expressing mHCN1 and EGFP (right), mHCN1 and EGFP-Mint1 (left).* ***B.*** *Mean steady state current/voltage relations of mHCN1+EGFP (black filled circles, n=8) and mHCN1+EGFP-Mint1 (red filled circles, n=8).* ***C.*** *Mean steady state current/voltage relations of mHCN1+EGFP (black filled circles, n=15) and mHCN1+EGFP-Mint2 (blue filled circles, n=12).* ***D.*** *Mean steady state current/voltage relations of mHCN2+EGFP (black filled circles, n=9) and mHCN2+EGFP-Mint1 (red filled circles, n=6).* ***E.*** *Mean steady state current/voltage relations of mHCN2+EGFP (black filled circle, n=8s) and mHCN2+EGFP-Mint2 (blue filled circles, n=8).*

When mHCN2 is co-expressed with EGFP-Mint1, its current decreases 4.5 folds calculated at -140 mV (panel D), and with EGFP-Mint2 there is a 2.7 fold decrease calculated at -140 mV (panel E). The decrease in the current prevented tail current analysis and thus the analysis of the gating properties of the channel (see Fig.24 panel A).

To prove the specificity of the effect of Mints on HCN channels, I decided to co-express Mint proteins with other two well characterized voltage-gated K+ channels: KAT1 and hERG.

In the first control experiment, HEK293T cells were co-transfected with KAT1 and EGFP cDNAs as control, and KAT1 and EGFP-Mint1 in equal amounts. The currents were measured in whole-cell configuration and analysed in order to see effects on both channel properties (trafficking and gating).

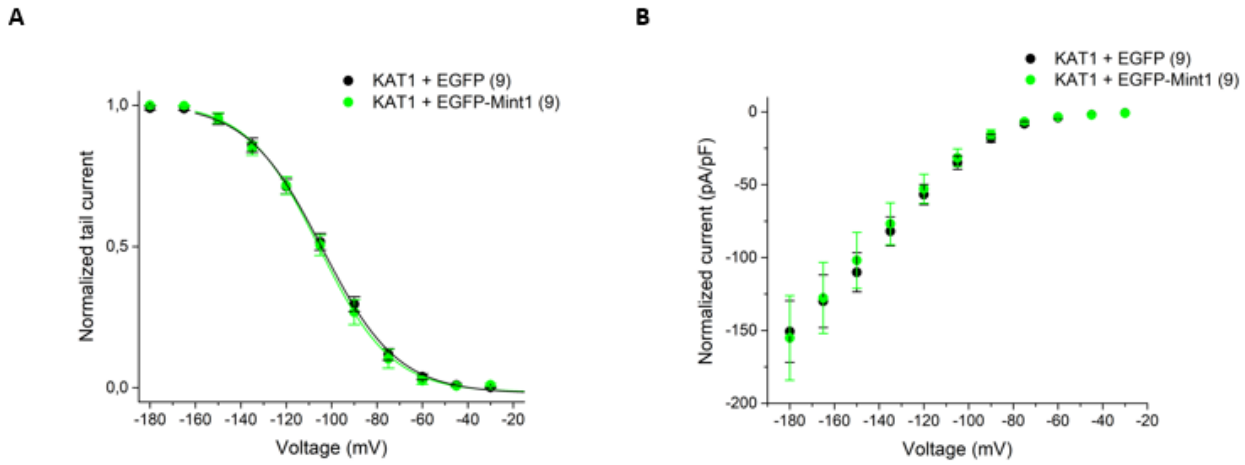

Figure 26 Effect of Mint1 co-expression on KAT1 . ***A.*** *Mean tail current activation curves of KAT1 + EGFP (black filled line and circles, n=9) and of KAT1 co-expressed with EGFP-Mint1 (green filled line and circles, n=9). Lines show fits of a Boltzmann function. V1/2 of KAT1+ EGFP = -104.1 ± 0.9 mV; V1/2 of KAT1+ EGFP-Mint1 = -105.5 ± 0.6 mV. The values did not differ significantly (P > 0.05).* ***B.*** *Mean steady state current/voltage relations of KAT1 + EGFP (black filled circles, n=9) and KAT1 + EGFP-Mint1 (green filled circles, n=9).*

Figure 26 shows the results of the co-expression of KAT1 with EGFP-Mint1. In panel A, the two normalized activation curves of KAT1 alone (in black) and expressed with EGFP-Mint1 (in green) are represented. The two curves are similar, meaning that the co-expression did not change the gating properties of the channel. Panel B shows the normalized currents of the channel alone (in black) or co-expressed with EGFP-Mint1 (in green) which are similar. In conclusion, Mint1 co-expression did not alter neither the gating properties of the channel (Fig.26A no shift in the activation curve, and thus in the $V_{1/2}$ value) nor the trafficking ones (no difference in the current density Fig.26B).

Finally, EGFP-Mint2 was co-expressed with human ERG channel. As control, hERG was co-expressed with an equal amount of EGFP cDNA, as before.

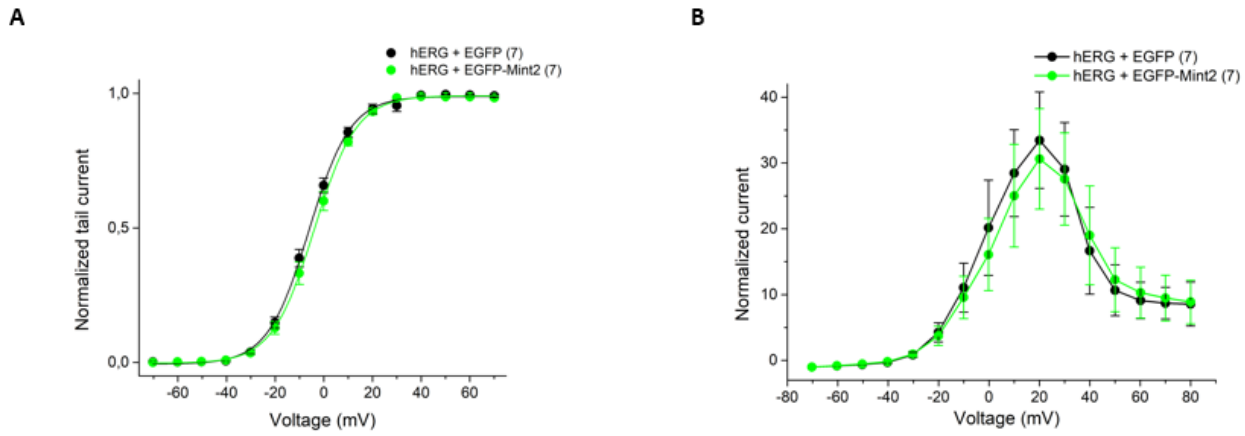

Figure 27 Effect of Mint2 co-expression on hERG . A. Mean tail current activation curves of hERG + EGFP (black filled line and dots, n=7) and of hERG co-expressed with EGFP-Mint2 (green filled line and dots, n=7). Lines show fits of a Boltzmann function. $V_{1/2}$ of hERG + EGFP = -6.1 ± 0.3 mV; $V_{1/2}$ of hERG+ EGFP-Mint1 = -4 ± 0.2 mV. The values did not differ significantly (P > 0.05). B. Mean steady state current/voltage relations of hERG + EGFP (black filled circles, n=7) and hERG + EGFP-Mint1 (green filled circles, n=7).

As shown in figure 27, the co-expression of EGFP-Mint2 with hERG has no effect on both the $V_{1/2}$ of the channel (gating property, Fig.27A) and its current density (trafficking of the channel to the plasma membrane, Fig.27B).

In conclusion, the co-expression of HCN channels with Mint1 and 2 caused a decrease in HCN current which was proved to be specific.

The decrease in the current of the HCN1/2 channels, obtained after Mints co-expression, could be the result of different events among which, for instance, protein stability.

To verify this possibility, I performed a western blot on lysates from HEK293T cells previously transfected with the channel alone (with EGFP as control) and with the channel and its interactors Mint1 or Mint 2. TRIP8b was co-transfected as a negative control, since it is known not to affect the channel total protein level.

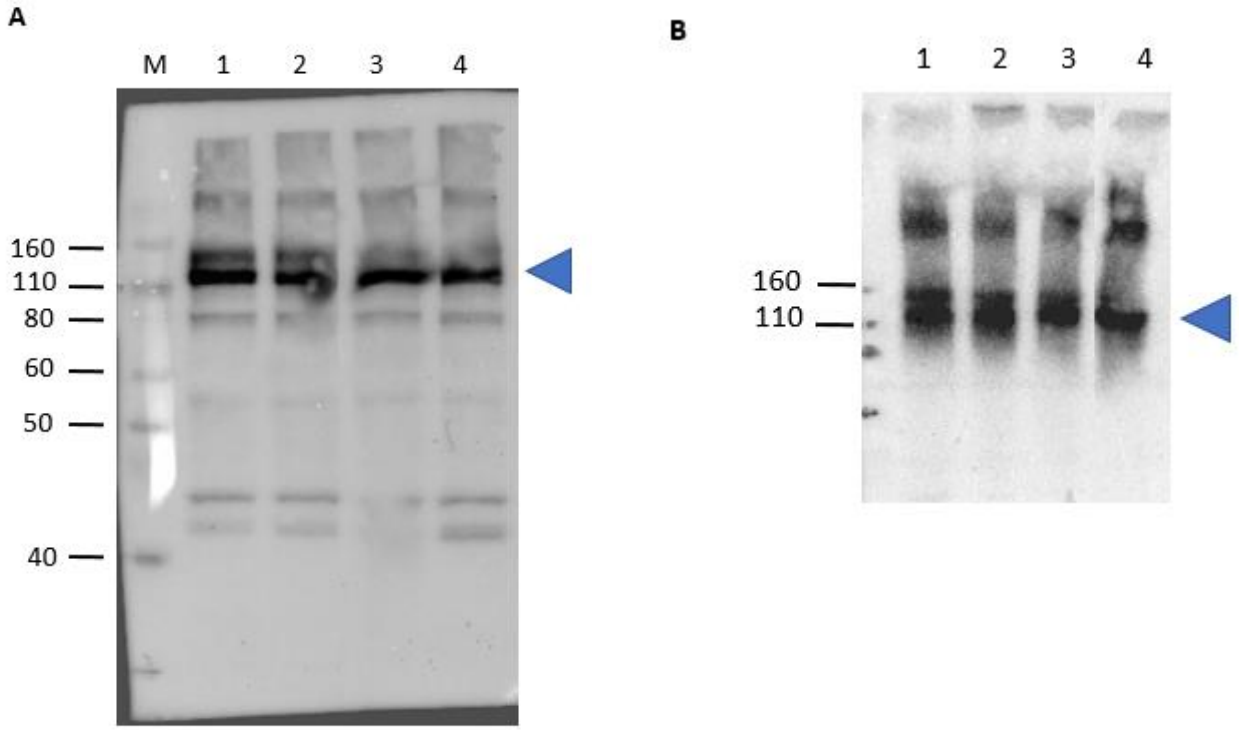

Figure 28 Western blot analysis of HCN total protein levels in the presence and absence of Mints in HEK293T cells. ***A.*** *Western blot concerning mHCN1 protein levels. M = protein marker (Novex® Sharp Pre-stained Protein Standards, Invitrogen), 1 = mHCN1+EGFP, 2=mHCN1+EGFP-Mint1, 3=mHCN1+EGFP-Mint2, 4=mHCN1+EGFP-TRIP8b(1a-4). The blue arrowhead indicates mHCN1 monomer. Numbers on the left indicate the molecular weight (KDa) of the marker.* ***B.*** *Western blot concerning mHCN2 protein levels. 1= mHCN2+EGFP, 2=mHCN2+EGFP-Mint1, 3=mHCN2+EGFP-Mint2, 4=mHCN2+EGFP-TRIP8b. The blue arrowhead indicates mHCN2 monomer. Numbers on the left indicate the molecular weight (KDa) of the marker.*

As expected, there is no difference when both mHCN1 and 2 are co-expressed with EGFP-TRIP8b, (Fig.28A and B compare lane 1 and 4). For what it concerns Mint proteins, the co-expression of the two channels with both Mint1 and 2 has no appreciable effect on the protein levels of the channels. From this result, Mint1 and 2 do not seem to decrease the total levels of mHCN1 and mHCN2 proteins in HEK293T cells.

The decrease of HCN current recorded in HEK293T cells upon the co-expression with Mint proteins (shown in Fig.25) could be the result of an inhibitory action on channel function (an effect on the gating or the permeability of the channel) or a reduction of the number of the channels in the plasma membrane (effect on the trafficking of the channel). In order to investigate these two possibilities, HEK293T cells were transfected with a EGFP-HCN2 protein with an extracellular HA tag (hemmaglutinin tag) sequence inserted in the transmembrane segment between S3 and S4 (Santoro et al. 2004). This epitope allows the detection of the channel present in the plasma membrane under nonpermeabilizing conditions by means of a commercially available antibody

against the HA tag. When the EGFP-HCN2 tagged protein was expressed in HEK 293T cells, the EGFP signal was detected by direct fluorescence with a confocal microscope and it shows an intracellular distribution that makes it difficult to assess the plasma membrane signal (Fig. 29 A, green signal). For this reason, in nonpermeabilizing conditions, the HA tag signal (in red in Fig. 29 A) was detected at the plasma membrane with a confocal microscope. In order to determine whether the HA tag signal was affected in the presence of Mint2, I decided to quantify for 34 cells (17 cells for each sample) the signal at the plasma membrane level. As shown in Fig. 29B, using Fiji software, for of each cell I draw five perpendicular lines to the plasma membrane and quantified the fluorescence signal across each line. From all the signal values, I took the maximum value corresponding to the peak and averaged all the peak values for each sample. The results of this analysis is reported in Fig.29C and it shows that upon Mint2 expression the signal of the HA tag decreases at the plasma membrane.

In conclusion, upon Mint2 co-expression, the channel is redistributed from the plasma membrane and this explains the current reduction of the channel (Fig.25).

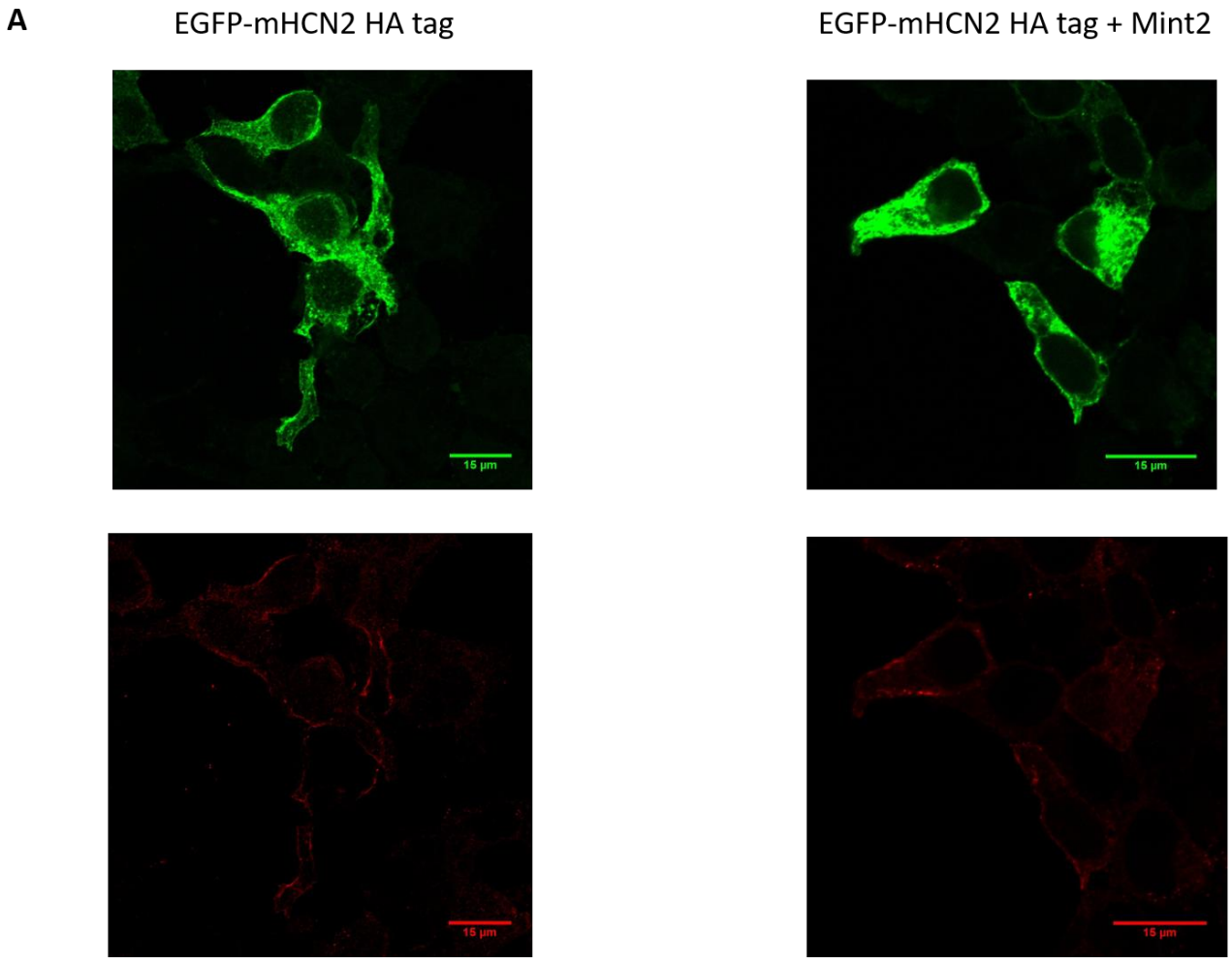

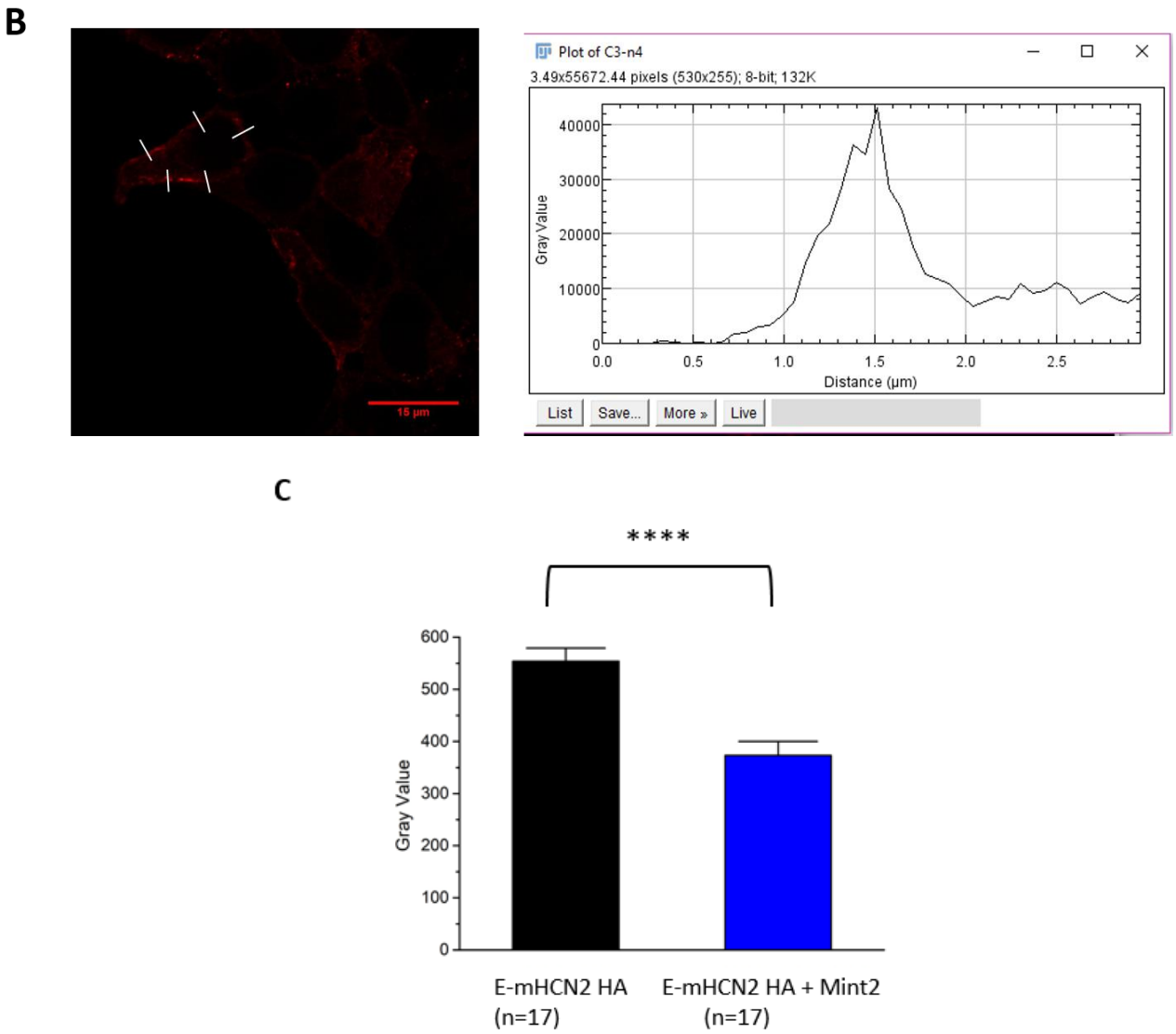

Figure 29 HEK293T cells were co-transfected with EGFP-mHCN2 HA tagged alone or with Mint2 ***A.*** *Representative images of cells expressing EGFP-mHCN2 HA tag alone (right) or with Mint2 (left). In green it is shown EGFP-mHCN2HA tag, whereas in red the signal of the antibody against the HA tag.* ***B.*** *Scheme of the procedure used to quantify the fluorescence across the plasma membrane. For each cell, five perpendicular lines to the plasma membrane were drawn (in white). For each line, the Fiji (ImageJ) software quantified the fluorescence signal from which the maximum value of the peak (corresponding to the plasma membrane signal) was taken. For each sample, all the peak values were averaged together.* ***C.*** *Quantification of the reduction of the signal in the plasma membrane. The reduction was calculated with the T-test and resulted statistically significant p<0.0001. (n= 17 cells per sample).*

After the co-expression with Mint proteins, the total amount of HCN protein is unaffected (Fig.28) but, at the same time, the amount of channels present in the plasma membrane decreases (Fig.29). I wanted to investigate whether Mint co-expression had effect on channel trafficking. To this aim, HEK293T cells were transfected with the cDNA of mHCN2 with EGFP (as control) and with EGFP-Mint2. Cells were permeabilized and incubated with an antibody against HCN2 (Neuromab). In Fig.29A two representative confocal images are reported and the signal corresponding to HCN2

is shown in red. When expressed without its interactor, the channel distribution is homogeneous (Fig.30 right). Whereas, upon co-expression and interaction with EGFP-Mint2, the channel distribution changes and the channels results more localized perinuclearly (red signal in Fig.30 left). The green signal corresponds to EGFP fused to Mint2, confirming that the cell is expressing Mint2 proteins.

Panel B shows the quantification of the phenotype frequency of HCN2 distribution that changes when Mint2 is expressed.

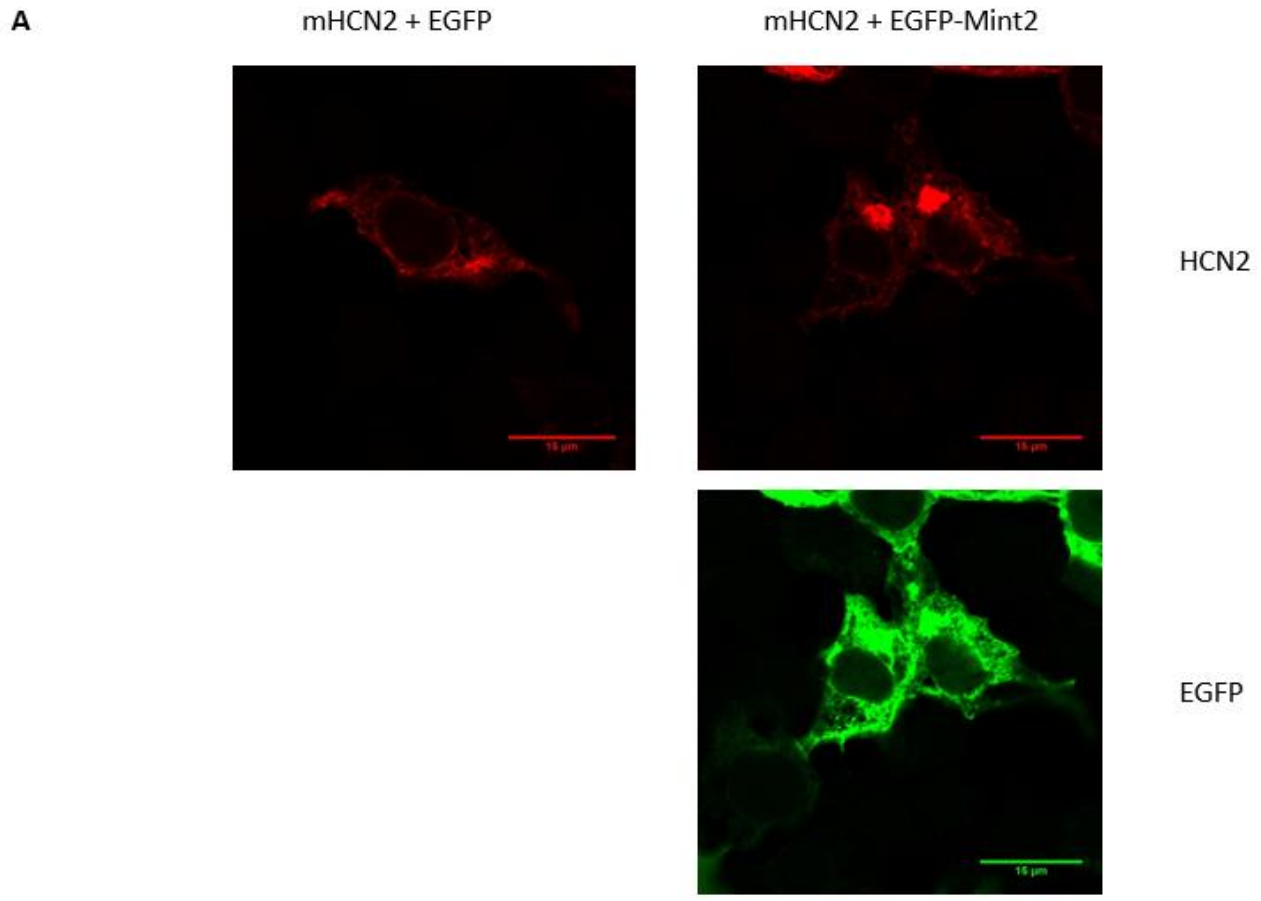

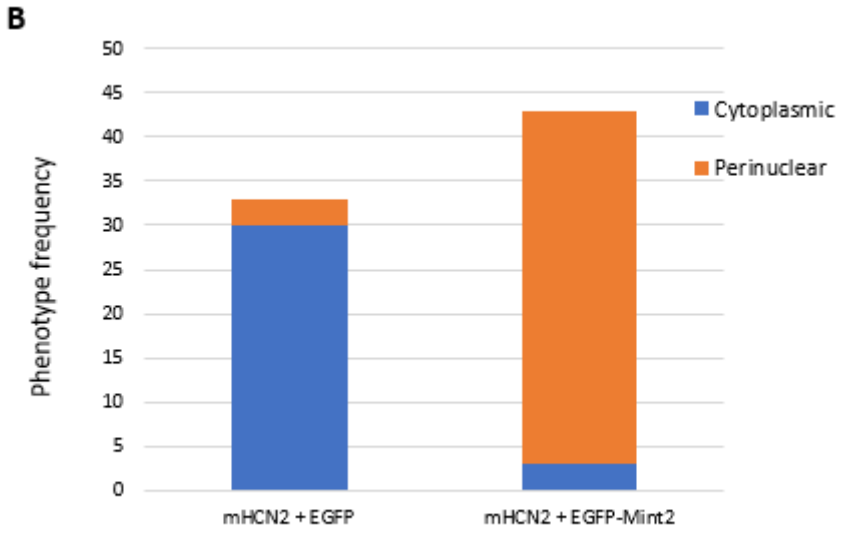

Figure 30 HEK293T cells were co-transfected with mHCN2 and EGFP alone or EGFP-Mint2. ***A.*** *Representative images of the subcellular localization of mHCN2 (in red). EGFP-Mint2 is shown in green.* ***B.*** *Quantification representing phenotype frequency as described in A (mHCN2+EGFP n=33, mHCN2+EGFP-Mint2 n=43).*

4.2.2 Identification of the regions important for the interaction between HCN and Mint proteins

In 2004, Kimura et al. began to define the regions of HCN2 and Mint2 involved in the interaction. By means of pull down assays performed on full length and deletion constructs co-expressed in COS7 cells, they found HCN2 channel to interact with Mint2 through its C-terminal domain. More specifically, they found that the region downstream of C-helix of the CNBD interacts with Mint2 (Fig.14) (Kimura et al. 2004). This region is 267 residues long, starting after residue L_{643} and ending with residue L_{910} (shown in Figure 31). In the same paper, Kimura et al also demonstrated that Mint2 interacts with HCN channels through its N-terminal domain (Fig.14), called MID (Munc-18 interacting domain) (Kimura et al. 2004). This domain is 356 amino acid long and is found in Mint1 and Mint2 but not in Mint3 (as it will become evident later in this thesis).

As part of my thesis work, I decided to 1) confirm the interaction domain of HCN and Mint2 by an independent approach, i.e. patch clamp experiments; 2) further restrict the interaction domain on HCN C-terminus; 3) confirm that MID is the interaction domain of Mint protein.

4.2.2.1 Interaction domain of Mint2 on the HCN2 C-terminus

Figure 31 Sequence alignment of the C-terminal domains of mHCN1 and mHCN2. Secondary structures are represented by rectangles (α helices) and arrows (β strands). The C-linker domain secondary structure is coloured in orange, whereas the CNBD secondary structure is in light blue. Secondary structure is based on Lee & Mackinnon 2017.

The red line indicates the end of the HCN2 construct used in Kimura et al.,2004. The coloured rectangles highlight the three conserved C-terminal regions, which could represent Mint binding site. The coloured lines indicate the last residue of each deletion mutant which was prepared and then tested electrophysiologically in HEK293T cells.

Figure 31 shows the alignment of mHCN1 and mHCN2 C-termini. The C-terminus includes a very much conserved CNBD sequence that ends with the C helix, two other conserved helices of unknown function (helices D and E) and a poorly conserved downstream sequence.

In figure 31, the red line represents the end of Kimura's HCN2 construct found to lose the binding with Mint2.

Three conserved regions, present at the C-terminus of both channels, could be involved in the binding of Mints and thus represent the hypothetical binding site of Mints. The first conserved stretch of amino acids includes helices D and E (boxed and coloured in orange in Fig.31).

The second conserved region is boxed in green and called SAS sequence (as in Santoro et al. 2004). This region is conserved among the four isoforms of HCN channels, but no protein was shown to interact with the channels through this region.

The third stretch of conserved amino acids is at the very C-terminus and includes the last three residues of HCN sequence: SNL. These three residues are important for the interaction with another known interactor of HCN channels, the auxiliary protein TRIP8b.

I therefore prepared three deletion mutants:

-Construct αCstop, ending at residue L_{663}, after the CNBD C-helix (the original Kimura construct).

-Construct αD/Estop, ending at residue E_{679}, highlighted by an orange line in Figure 31. This construct lacks the conserved SNL sequence and the conserved SAS sequence but includes helices D and E.

-Construct SASregion stop, ending at R_{813}, highlighted by a green line in Figure 31. This construct lacks the conserved SNL ending sequence and includes the other two conserved sequences (helices D and e and SAS sequence).

The full length HCN2 and deletion mutants were co-expressed in HEK 293T cells with EGFP-Mint2 protein and their currents were recorded by patch clamp.

I first tested the Kimura construct (construct αCstop) to confirm by electrophysiology that HCN2 ending with the CNBD C-helix loses the interaction with Mint2.

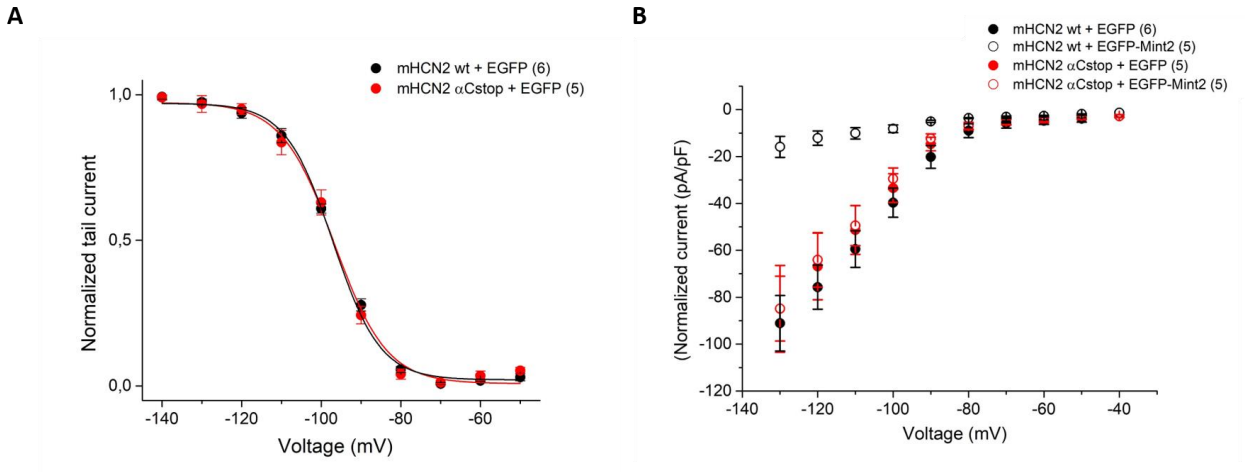

Figure 32 Effect of Mint2 on mHCN2 full-length and deleted (αCstop). ***A.*** *Mean t activation curves of mHCN2 full-length (wt) + EGFP (black filled line and dots, n=6) and of mHCN2 αCstop with EGFP-Mint2 (red filled line and dots, n=5). Lines show fits of a Boltzmann function.* $V_{1/2}$ *of mHCN2 wt+ EGFP= - 97.1 ± 0.7 mV;* $V_{1/2}$ *of mHCN2 αCstop + EGFP = -96.8 ± 0.3 mV. The values did not differ significantly (*P > *0.05).* ***B.*** *Mean steady state current/voltage relations of mHCN2 wt + EGFP (black filled circles, n=6) and mHCN2 wt + EGFP-Mint2 (black empty circles, n=5), mHCN2 αCstop + EGFP (red filled circles, n=5), mHCN2 αCstop + EGFP-Mint2 (red open circles, n=5).*

In figure 32A, the activation curves of the full-length (in black) and αCstop mutant (in red) are plotted together to show that the gating properties of the two channels are the same. Panel B shows the normalized currents of the two channels in presence and absence of EGFP-Mint2. The full-length channel (black line) current decreases upon EGFP-Mint2 co-expression (open black dot). For the mutated channel, EGFP-Mint2 co-expression does not decrease the current. In fact, the line with red dots (mutant alone) and the line with red empty dots (mutated channel co-expressed with EGFP-Mint2) overlap. In conclusion, the current of the deleted channel shows no difference in presence or absence of EGFP-Mint2, meaning and confirming that the deleted region is important for the interaction with Mint2 (as in Kimura et al. 2004).

The second mutant that was tested was SASregion stop, which ends at R_{813} and includes two conserved regions: the D and E helices (highlighted in orange in Fig.31) and the SAS region (highlighted in green in Fig.31).

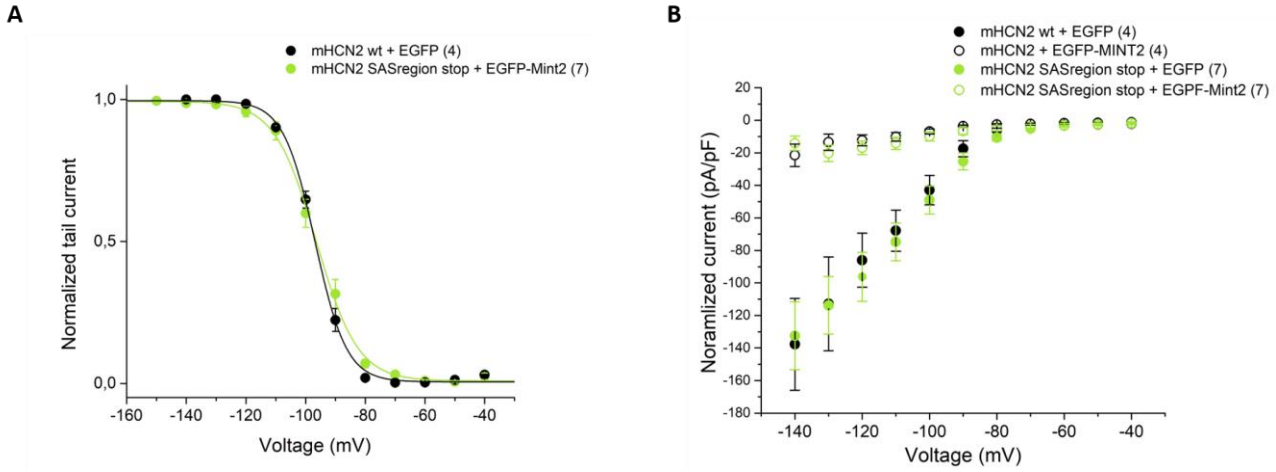

Figure 33 Effect of Mint2 on mHCN2 full-length and deleted (SASregion stop). ***A.*** *Mean activation curves of mHCN2 full-length (wt) + EGFP (black filled line and dots, n=4) and of mHCN2 SASregion stop with EGFP-Mint2 (green filled line and dots, n=4). Lines show fits of a Boltzmann function. $V_{1/2}$ of mHCN2 wt+ EGFP = - 96.5 ± 0.5 mV; $V_{1/2}$ of mHCN2 SASregion stop + EGFP = -96.9 ± 0.3 mV. The values did not differ significantly (P > 0.05).* ***B.*** *Mean steady state current/voltage relations of mHCN2 wt + EGFP (black filled circles, n=4) and mHCN2 wt + EGFP-Mint2 (black empty circles, n=4), mHCN2 SASregion stop + EGFP (green filled circles, n=7), mHCN2 SASregion stop + EGFP-Mint2 (green open circles, n=7).*

Figure 33A shows no difference in the activation curves of the SAS construct and the full-length HCN2 channel, meaning that the deletion has no effect on the gating properties of the channel with respect to the full-length one.

Figure 33B shows the normalized currents of the two channels in the presence and in the absence of EGFP-Mint2. Co-expression of EGFP-Mint2 causes a similar decrease in the current of both channels (open dots Fig.33B). This result shows that the third conserved region SLN (light blue in

Fig.31) is not required for the binding and the effect of Mints on HCN channels, whereas the other two or just one of them are.

At this point, I tested the construct αD/Estop, the deletion mutant which ends with residue R_{659} and lacks the SNL and the SAS conserved regions but not the D and E helices.

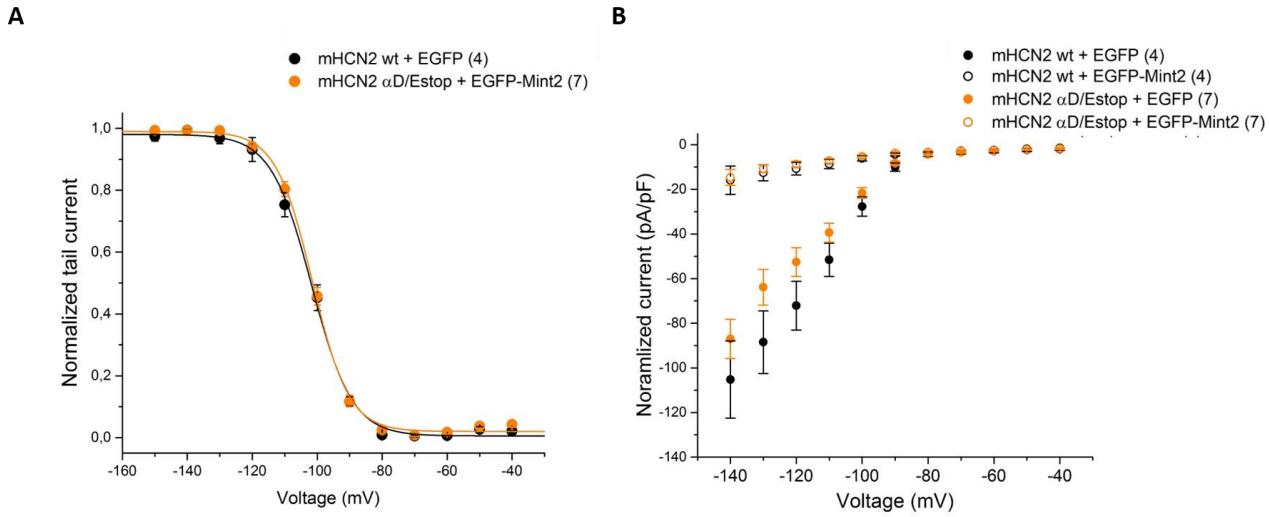

Figure 34 Effect of Mint2 co-expression on mHCN2 full-length and deleted (αD/Estop). ***A.*** *Mean activation curves of mHCN2 full-length (wt) + EGFP (black filled line and dots, n=4) and of mHCN2 αD/Estop with EGFP-Mint2 (orange filled line and dots, n=7). Lines show fits of a Boltzmann function.* $V_{1/2}$ *of mHCN2 wt+ EGFP = - 101.7 ± 0.5 mV ;* $V_{1/2}$ *of mHCN2 αD/Estop + EGFP = -101.5 ± 0.4 mV. The values did not differ significantly (P > 0.05).* ***B.*** *Mean steady state current/voltage relations of mHCN2 wt + EGFP (black filled circles, n=4) and mHCN2 wt + EGFP-Mint2 (black open circles, n=4), mHCN2 αD/Estop + EGFP (orange filled circles, n=7), mHCN2 αD/Estop + EGFP-Mint2 (orange open circles, n=7).*

This mutant had no effect on the gating properties of the channel. As shown in Fig.34A, the two activation curves of the two channels overlap, meaning that the gating properties are unaltered upon the deletion. Moreover, the co-expression of EGFP-Mint2 caused a decrease in the current for both the full-length and the αE/D mutant (Fig.34B). This result underlies the importance of the D and E helices in the interaction with Mint2: when these two helices are re-introduced in the channel, the Mint specific effect on the current is restored.

4.2.2.2 Mint1 and Mint2 share the same interaction site on HCN2

The same experiments were repeated by co-transfecting the constructs (αCstop and αD/Estop) with Mint1, in order to test whether the D and E helices of HCN2 were also important for the interaction of Mint1.

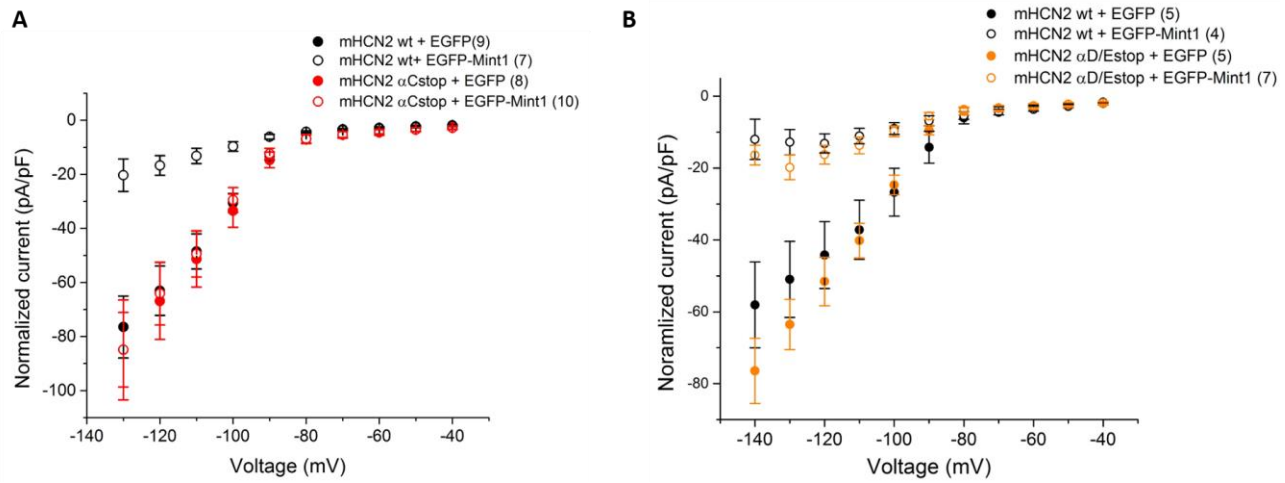

Figure 35 Effect of Mint1 co-expression on mHCN2 full-length and deleted channels. ***A.*** *Mean steady state current/voltage relations of mHCN2 wt + EGFP (black filled circles, n=9) and mHCN2 wt + EGFP-Mint1 (black open circles, n=7), mHCN2 αCstop + EGFP (orange filled circles, n=8), mHCN2 αCstop + EGFP-Mint1 (orange open circles, n=10).*

B. *Mean steady state current/voltage relations of mHCN2 wt + EGFP (black filled circles, n=5) and mHCN2 wt + EGFP-Mint1 (black empty circles, n=4), mHCN2 αD/Estop + EGFP (orange filled circles, n=5), mHCN2 αD/Estop + EGFP-Mint1 (orange empty circles, n=7).*

Figure 35 summarizes the results, showing that also Mint1 requires the presence of helices D and E to bind the C terminus of HCN2. Indeed, panel A shows a marked reduction in the current of the full-length channels, due to the presence of Mint1, while construct αCstop is unaffected. Panel B shows that the effect of Mint1 is restored when these two helices are present, as in construct αD/Estop.

4.2.2.3 Confirming the interaction domain on Mint proteins

As mentioned before, Kimura's paper showed that the interaction domain of Mint1 and 2 proteins with HCN2 channels is the so-called MID domain, found at the N terminus of Mint 1 and 2 proteins. In order to confirm Kimura et al.'s data, I took advantage of a third isoform, Mint3, belonging to the same family but lacking the N-terminal MID domain (Fig.14). When co-expressed with either mHCN1 or mHCN2 in HEK293T cells, Mint3 did not produce any significant effect on channel gating (Fig.36A and C), nor any reduction of the current (Fig.36B and D). These results,

shown in Figure 36, suggest that the effect of Mint proteins on HCN currents is mediated by the presence of the MID domain, in agreement with the results of Kimura et al.

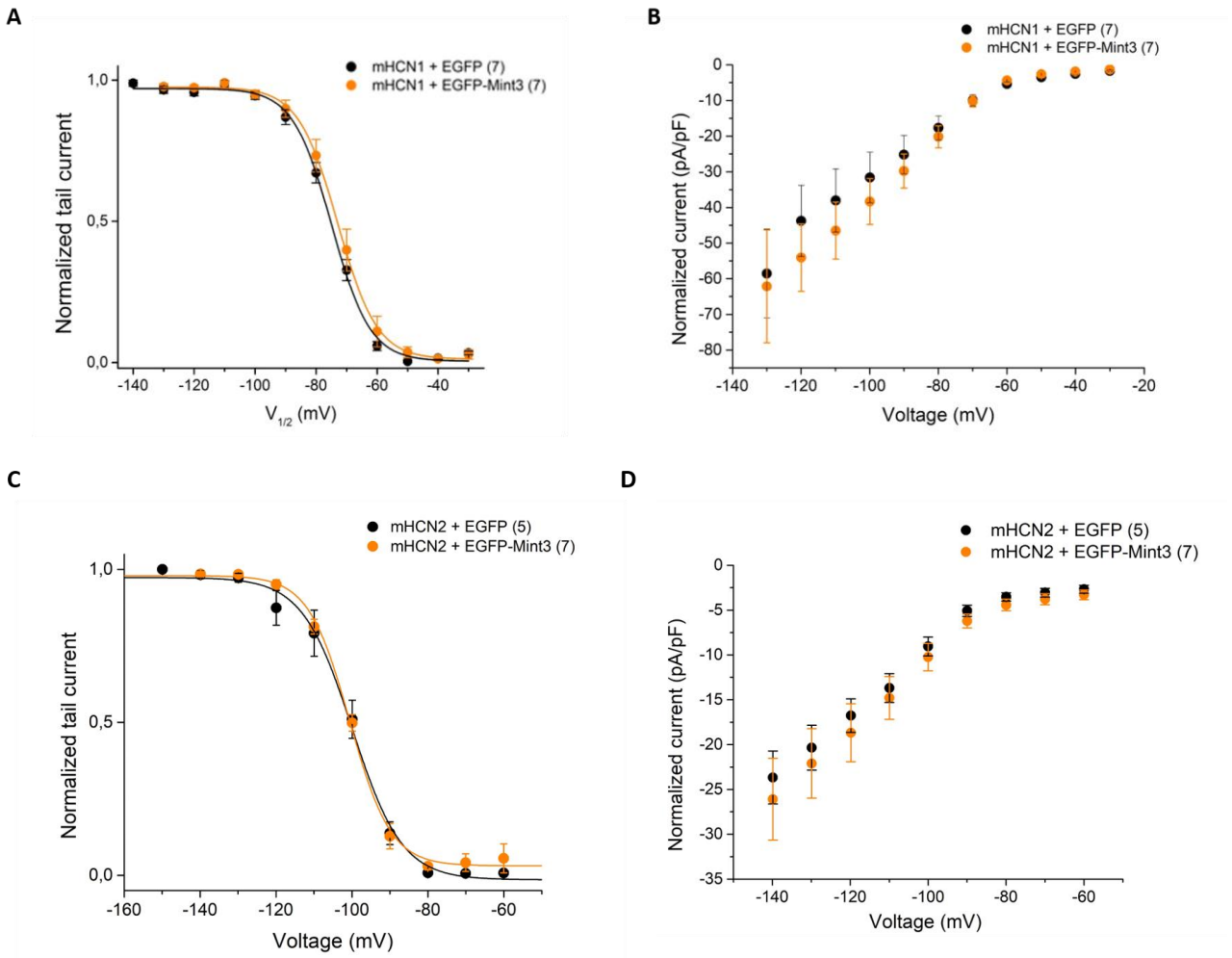

Figure 36 Effect of Mint3 co-expression on HCN channels. ***A.*** *Mean tail current activation curves of mHCN1 + EGFP (black filled line and dots, n=7) and of mHCN1 co-expressed with EGFP-Mint1 (orange filled line and dots, n=7). Lines show fits of a Boltzmann function.* $V_{1/2}$ *of mHCN1+ EGFP = -75 ± 0.5 mV;* $V_{1/2}$ *of mHCN1+ EGFP-Mint3 = -73 ± 0.4 mV. The values did not differ significantly (P > 0.05).* ***B.*** *Mean steady state current/voltage relations of mHCN1 + EGFP (black filled circles) and mHCN1 + EGFP-Mint3 (orange filled circles).* ***C.*** *Mean tail current activation curves of mHCN2 + EGFP (black filled line and dots, n=5) and of mHCN1 co-expressed with EGFP-Mint1 (orange filled line and dots, n=7). Lines show fits of a Boltzmann function.* $V_{1/2}$ *of mHCN2+ EGFP = -100 ± 0.9 mV;* $V_{1/2}$ *of mHCN2+ EGFP-Mint3 = -100.6 ± 0.6 mV. The values did not differ significantly (P > 0.05).* ***D.*** *Mean steady state current/voltage relations of mHCN2 + EGFP (black filled circles) and mHCN2 + EGFP-Mint3 (orange filled circles).*

4.2.3 In vitro validation of the binding site

For the first time, the interaction site of Mints on HCN channels was reduced to the helices D and E, which I found necessary for maintaining the Mint effect on HCN current. However, my result does not constitute a direct proof of the binding between HCN channels and Mint proteins. Therefore, I decided to test whether the D and E helices constitute the binding site of Mint. To do so, I used two different approaches: the co-expression and co-purification in *E.coli*, and the yeast two-hybrid technique.

For what it concerns the co-purification in *E.coli*, similarly to what I showed for TRIP8b, co-expression in *E.coli* was obtained by cloning the two genes in different plasmids with different antibiotic resistance and selecting for double resistance. Co-purification was performed at first through affinity purification by means of a tag placed on one of the two proteins, and then by size exclusion chromatography (gel filtration, GF). Finally, co-purification was confirmed on a SDS–PAGE and western blot.

As I have done for TRIP8b, I did not express the full length Mint and HCN proteins for this assay. For Mint proteins, I used the MID domain of Mint2 (from residue 1 to 356 of the rat isoform) which was fused to the GST protein at its N-terminus (as in Kimura et al. 2004), resulting in the construct GST-MID. For HCN2 channels, two constructs were created (shown in Fig.37): they both contain the CNBD of mouse HCN2 protein but they had different ends. In particular, one ends immediately after the C-helix of CNBD, hereafter named CNBD short (from residue E_{494} to H_{645}, used as negative control); the second contains two additional C-terminal helices (D and E helices), hereafter named CNBD long (from residue E_{494} to Q_{676}).

At first, these deletion mutants were fused at their N-termini to a His_6-MBP tag, as this is a standard procedure set up in the laboratory for facilitating the heterologous expression of soluble proteins in *E. coli.* However, I found that MBP tag aspecifically interacted with the fusion GST-MID protein. In order to overcome this problem, the MBP tag was removed, leaving only an N-terminal His_6 tag on the two constructs: His_6-CNBD short and His_6-CNBD long. Since the removal of the MBP tag did not affect neither overexpression of CNBD fragments, nor the solubility of the purified protein, I set up the co-expression and co-purification assay with these constructs.

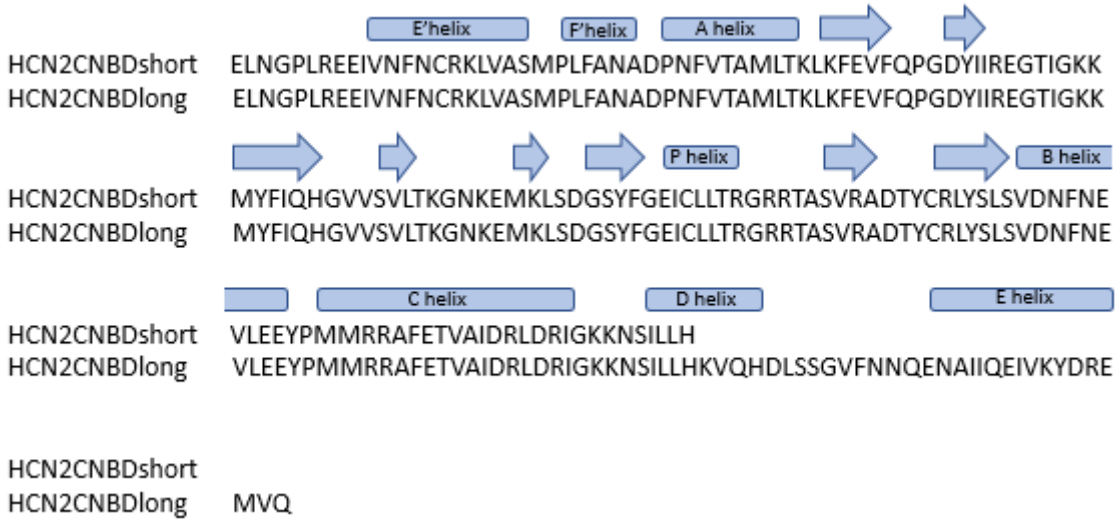

Figure 37 Sequence alignment of the two CNBD constructs of HCN2 used for the co-expression and co-purification assays in E.coli. Secondary structures are represented in by rectangles (α helices) and arrows (β strands). Secondary structure assignation is based on Lee & Mackinnon 2017.

The co-expression and co-purification assay was set as follows: the two proteins His_6-CNBD (short or long) and GST-MID were co-expressed in *E.coli* and MID fragment was purified by means of its GST tag. The elution sample of the GST-affinity chromatography was further loaded in gel filtration in order to isolate the MID proteins from the contaminant proteins of the affinity chromatography step. Finally, the co-purification of the two proteins of interest was assessed by running a SDS-PAGE, followed by both a coomassie staining and by western blot anti His_6 tag, of both the elution of the GST-affinity chromatography and the elution peak of the gel filtration which corresponds to MID fragment.

First, I tested the long CNBD protein, which contains the D and E helices.

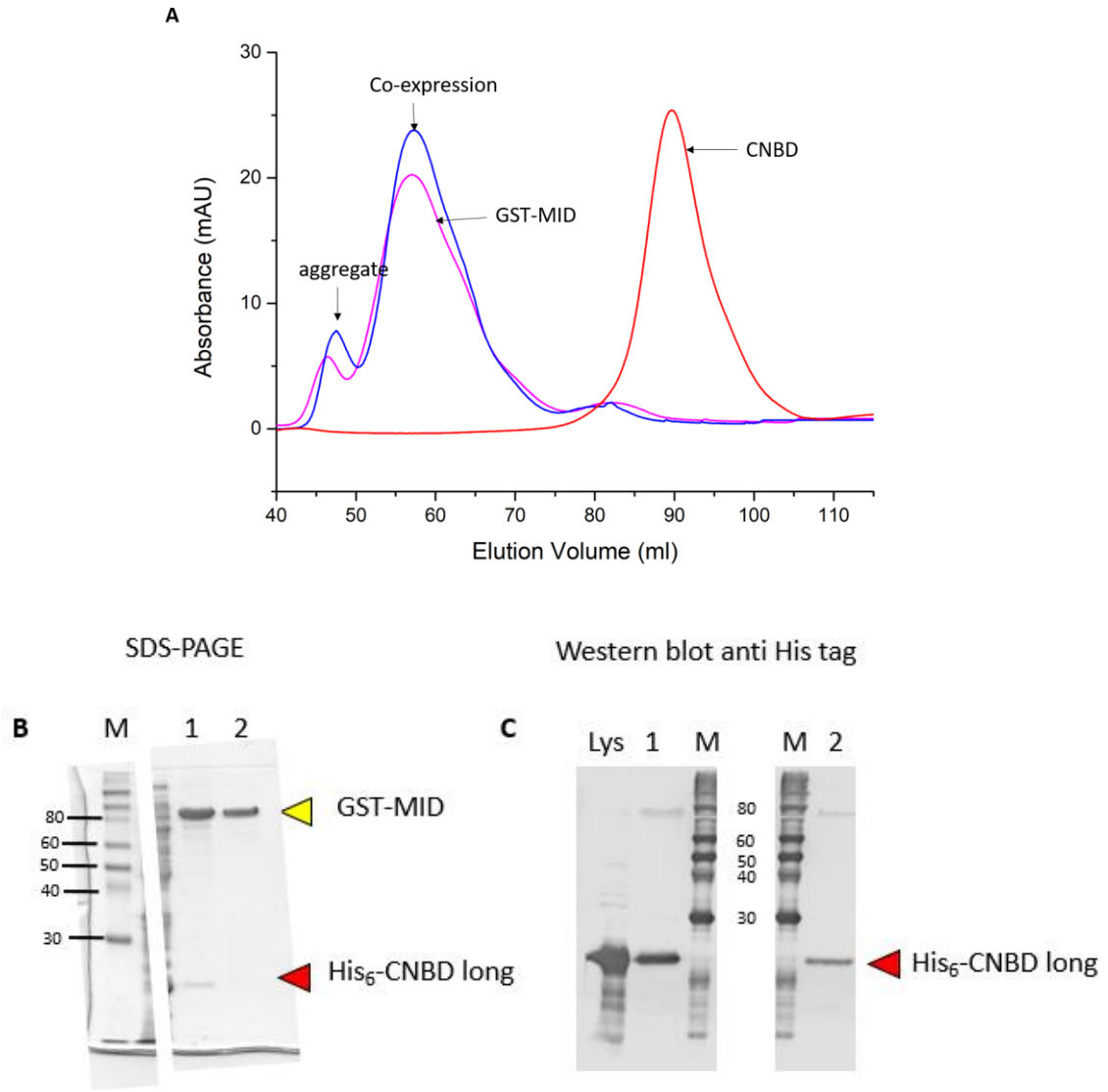

Figure 38 Results of the co-expression and co-purification of GST-MID and His_6-CNBD long (21KDa) in E.coli. ***A.*** *Gel filtration chromatogram. In blue it is represented the chromatogram of the co-expression and co-purification. In red it is represented the chromatogram of the purification of the CNBD alone and in magenta the chromatogram of the purification of GST-MID alone.* ***B.*** *SDS-PAGE M=marker, lane 1 elution of the GST column, lane 2 elution of the gel filtration peak.* ***C.*** *Western blot: lys= cellular lysate (as positive control), lane1 elution of the GST column, lane 2 elution of the gel filtration peak.*

Fig.38A shows the superimposition of three different gel filtration profiles: the CNBD protein (red line); the GST-MID (magenta line) and the co-expression (blue line). To note that the peak in the elution window of 40 – 50 ml (see blue and magenta line) corresponds to the aggregated GST-MID. The peak, which elutes at around 60 ml, is present in both the blue (co-expression) and magenta (GST-MID) elution profiles and corresponds to the soluble GST-MID protein. The blue peak (co-expression) was analysed both in SDS-PAGE (panel B) and western blot (panel C) to detect the presence of the CNBD protein construct.

In the SDS-PAGE (Fig.38B), I also checked the elution of the affinity chromatography (sample before the injection in gel filtration) and it is possible to detect prevalently the presence of the GST-MID protein (yellow arrowhead, lane 1), whereas there is a weak band at the expected molecular weight of the His_6-CNBD long protein (red arrowhead, lane 1). Instead, in lane 2, which corresponds to the gel filtration elution of the sample loaded in lane 1, I could only detect the presence of the GST-MID protein (yellow arrowhead, lane 2). In the western blot (Fig. 38C), where an antibody able to recognize the His_6 tag fused to the CNBD was used, in both lane1 and 2 it is possible to detect a band corresponding to the His_6-CNBD long protein (Fig.38C, red arrowhead), confirming that the two proteins are both present in the affinity column (lane 1) and gel filtration (lane 2) elution.

This data suggest that the GST-MID and His_6-CNBD long proteins can bind and co-elute in both the affinity purification and gel filtration.

However, the binding between the two proteins seems to be weak, since after the first step of the purification it can only be detected through the western blot technique.

Then I tested, as control, the shorter CNBD construct, which ends at the end of the C-helix and it is known to lose the binding with the MID domain (Kimura et al., 2004).

The results of the co-purification are shown in figure 39. As before, the affinity column elution was injected in gel filtration and the chromatogram is shown in blue in Fig.39A. Again, there is just one big peak, there is no peak where the CNBD protein should elute alone (red peak in Fig.39A). I tested both the fractions corresponding to the affinity chromatography elution (before injection in gel filtration) and the gel filtration peak of the co-expression of the two proteins. In SDS-PAGE (Fig.39B), in the elution of the affinity column the GST-MID band was detected (yellow arrowhead, lane 1 Fig.39B) and there was again a band at the expected molecular weight of the His_6-CNBD short (red arrowhead, lane 1 Fig.39B). In the elution of the gel filtration (Fig.39A, lane2) only the GST-MID protein is visible (yellow arrowhead). The two protein bands present in both line 1 and 2 (at 60 and 40 KDa) were tested in western blot (data not shown) with an antibody able to recognize the GST tag fused to MID domain. These two bands are likely to be the result of degradation of the MID fusion protein. To check the presence or absence of the short CNBD fusion protein, I performed a western blot (Fig.39C) on both the elution of the affinity chromatography (Fig.39C, lane 1) and of the gel filtration (Fig.39C, lane 2). In both lane 1 and 2, it was possible to detect the presence of the His_6-CNBD short protein (red arrowhead in Fig.39B) by using an antibody against the His_6 tag.

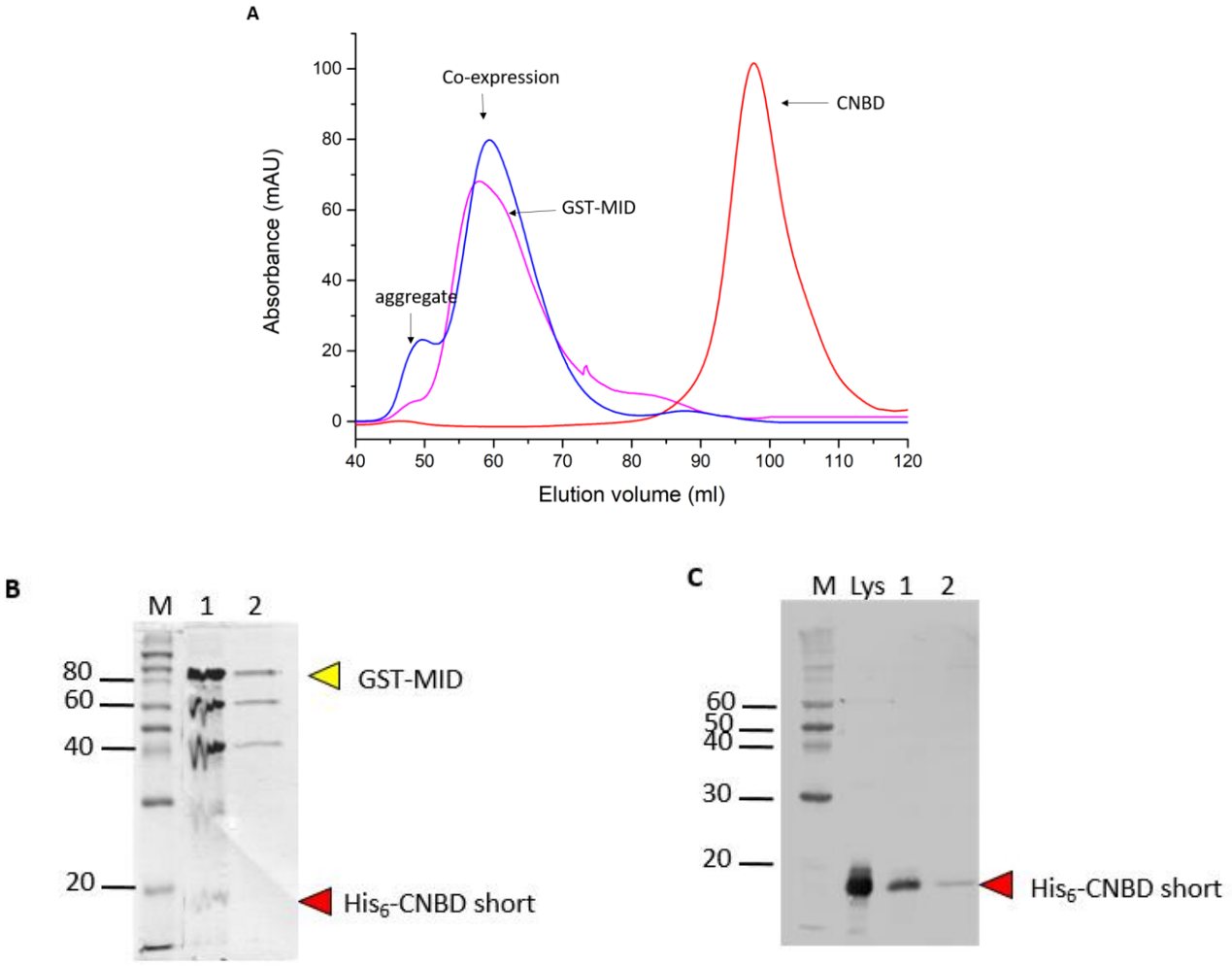

Figure 39 Results of the co-expression and co-purification of GST-MID and His_6-CNBD short (18 KDa) in E.coli. ***A.*** *Gel filtration chromatogram. In blue it is represented the chromatogram of the co-expression and co-purification. In red it is represented the chromatogram of the purification of the short CNBD alone and in magenta the chromatogram of the purification of GST-MID alone.* ***B.*** *SDS-PAGE M=marker, lane 1 elution of the GST column, lane 2 elution of the gel filtration peak.* ***C.*** *Western blot: lys= cellular lysate (as positive control), lane1 elution of the GST column, lane 2 elution of the gel filtration peak.*

From this data, it also seems that the shorter CNBD construct can interact with the fusion protein GST-MID and, as I observed for the longer construct, the binding seems weak.

This result was not in agreement with the literature: Kimura et al. had shown no interaction between GST-MID and the channel deleted of the region after the C-helix of the CNBD (which corresponds to the shorter construct). Moreover, this result was also in disagreement with the electrophysiological data already shown about the mutant αCstop (Fig.32) that confirmed a loss of the interaction with Mint2. For these reasons, I decided to test whether the detected weak binding was specific or was rather due to the aspecific binding of the CNBD to the GST tag. To answer this

question, the His_6-CNBD short protein was co-expressed with the GST tag alone in *E.coli*. Then the cell lysate was purified taking advantage of the GST column and the elution was analysed both with SDS-PAGE and western blot. In the SDS-PAGE shown in Fig.40A, it is possible to see a strong band corresponding to the GST tag (yellow arrowhead), along with many other less intense bands corresponding to protein interacting with the resin in an aspecific manner. When I perform a western blot (Fig.40B) on the same sample analysed in SDS-PAGE, unexpectedly, I detected the presence of the His_6-CNBD short protein (red arrowhead, lane E). This result proves that the weak binding detected in these co-expression and co-purification assays was most probably due to an aspecific binding of the GST tag to the CNBD, rather than a real interaction between the MID domain of Mint and the CNBD of the HCN channel.

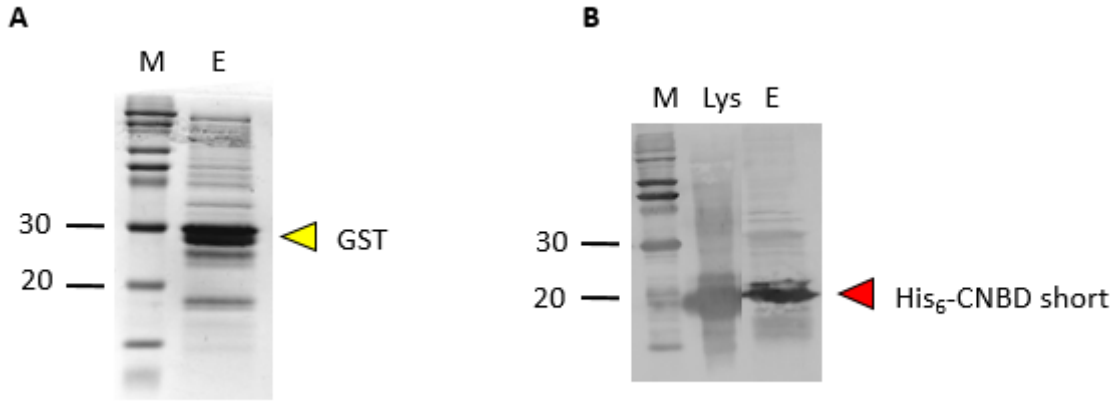

Figure 40 Results of the co-expression and co-purification of GST (30KDa) and His_6-CNBD short (18KDa) in E.coli. **A.** *SDS-PAGE: M=marker, E= elution of the GST column.* ***B.*** *Western blot: M=marker, lys= cellular lysate (as positive control), E= elution of the GST column.*

The binding assays performed in *E.coli* encountered the problem of aspecific binding to the tags used for expression and affinity purification (MBP and GST). I therefore decided to use a different approach: the yeast two hybrid system.

This well-known technique had already been used for studying Mint proteins (Okamoto & T C 1997). In particular, I used the Grow'N'Glow system (BIO 101) which uses LexA as a DNA binding domain, B42 as a transcription activation domain and GFP as a reporter of the transcription due to the interaction between the DNA binding domain and the activation domains.

For this assay, I prepared the prey and bait constructs as follows. Bait constructs were cloned into the vector pEG202, which is used to construct in frame fusions of LexA with the protein of interest.

This plasmid contains HIS3 (histidine gene) for selection in yeast. In this case, I used the C-termini of mHCN1 and mHCN2 as bait proteins. For the both of them, two constructs of different length were prepared: they all contained the C-linker (from residue D_{390} for mHCN1 and D_{443} for mHCN2). The short constructs included up to the C helix of the CNBD (up to residue Q_{592} for mHCN1 and L_{643} for mHCN2), whereas the long constructs also included the D and E helix of the CNBD (up to residue I_{625} for mHCN1 and E_{676} for mHCN2) (Fig.41).

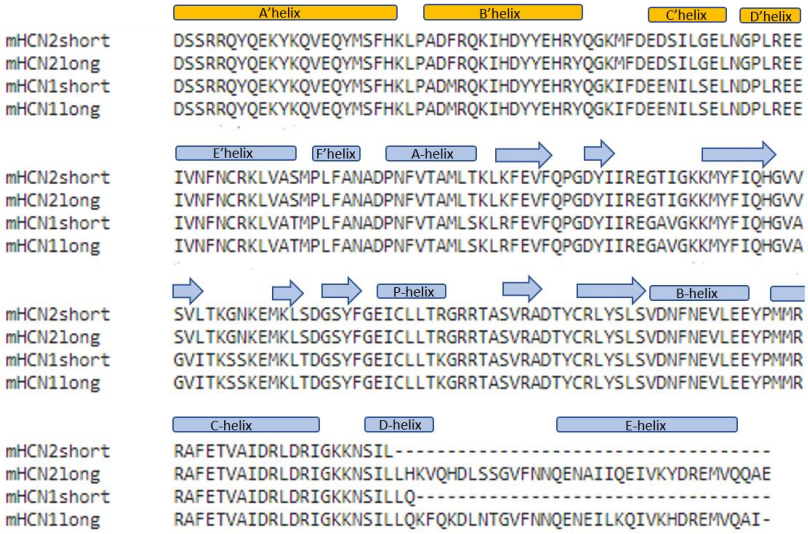

Figure 41 Sequence alignment of the short and long constructs which include the C-linker (in orange) and CNBD domains (in light blue) of mHCN1 and mHCN2. Rectangles (α helices) and arrows (β strands) represent secondary structures as in Lee & Mackinnon 2017.

Moreover, as a positive control for Mint constructs, into the bait vector I cloned Munc 18-1 full-length which is known to interact with MID domain of Mint proteins (Okamoto & T C 1997). All the resulting bait constructs are named as follows: pEG202::mHCN1 C-linker/CNBD short and long, pEG202::mHCN2 C-linker/CNBD short and long, and pEG202::Munc18-1. I also included pEG202 empty vector as negative control.

Instead, prey constructs were cloned into the pJG4-5 vector, which is used to express cDNAs fused to a cassette containing the SV40 nuclear localization sequence, the activator B42 and the HA tag. This plasmid contains TRP1 (thryptophan gene) for selection in yeast. In this prey plasmid, different constructs were cloned: the full-length Mint1 and 2, in order to test their interaction with the C-linker/CNBD constructs; miniTRIP8b as positive control as in Santoro et al.,2009.

The resulting prey constructs are named as follows: pJG4-5::miniTRIP8b, pGJ4-5::Mint1 full-length and pGJ4-5::Mint2 full-length.

For this assay, combinations of bait and prey plasmids were co-transformed with the reporter plasmid pGNG1. This vector contains the GFP gene under GAL1,10 promoter (non-galactose

inducible) which contains 8 binding sites to bind 4 LexA operators and only allows protein expression in presence of galactose. This plasmid contains URA3 (uracil gene) for yeast selection.
After the transformation, cells were plated on a selective medium (named Glu-UTH) containing glucose but lacking of URA, HIS3 and TRP1. The presence of glucose in the medium prevents the expression of the GFP reporter gene by repressing its promoter.
Transformants were re-streaked in triplicate on four different media: Glu-UTH, Glu-UTHL, Gal-UTH and Gal-UTHL. In Fig.42 it is shown an example of the procedure which was repeated for every experiment.

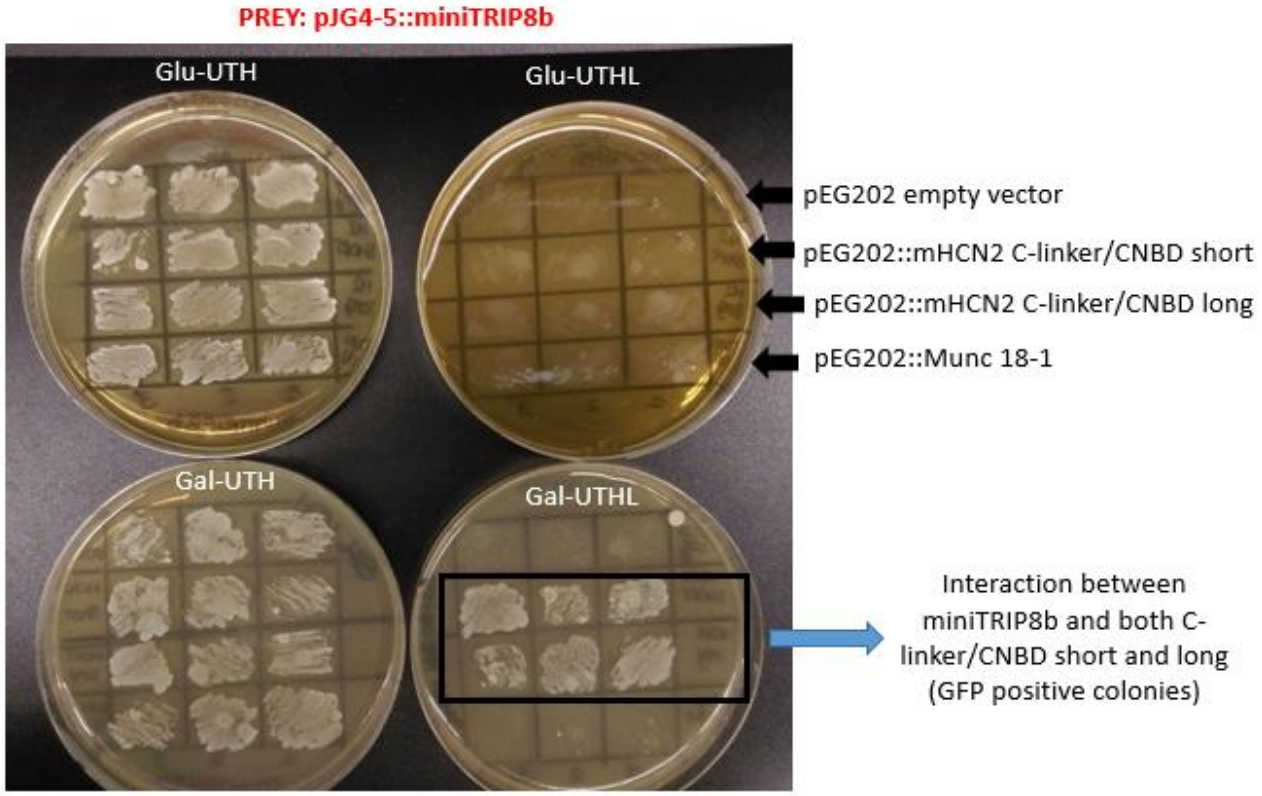

Figure 42 Picture of the four media used for the yeast two-hybrid assay. Glu = glucose, Gal = galactose, U = uracil, T = thryptophan, H= histidine, L= leucine.

The first medium, Glu-UTH, (upper left panel in Fig.42), is a further control where every clone grows since it contains the three plasmids. The second medium is similar to the first one but it also lacks leucine (Glu-UTHL, upper right panel in Fig.42). In this medium, no colony is supposed to grow because of the absence of leucine. Leucine is a genome-integrated reporter gene, which contains from 2 to 6 copies of the LexA operator upstream of the promoter. This allows the growth selection through the activation by LexA/B42. In this medium no colony is supposed to grow

because it contains glucose instead of galactose, in this way, no protein is expressed in order to activate the transcription of leucine which is absent in the medium.
The third medium contains galactose and lacks URA, HIS3 and TRP1 (Gal-UTH, bottom left in Fig.42). Here, cells are supposed to grow and, since it contains galactose, proteins are also expressed and therefore it serves as a positive control of the reporter expressions.
The last medium is the experimental one: it contains galactose, so proteins are expressed, and it also lacks URA, HIS3, TRP1 and LEU (Gal-UTHL, right bottom in Fig.42). On this medium, colonies grow only if the prey and the bait proteins are able to interact and thus to activate the translation of LEU genes. Moreover, if the interaction is strong, the GFP translation is also activated. Protein interactions using GFP as reporter are selected by examining transformants with a UV lamp after 3-4 days of growth.

	Bait (pJG4-5)		
Prey (pEG202)	miniTRIP8b (positive control)	Mint1 full-lenght	Mint2 full-lenght
Empty vector (negative control)	-	-	-
Munc18-1 (positive control)	-	+	+
mHCN1 C-linker/CNBD short	+	-	-
mHCN1 C-linker/CNBD long	+	-	-
mHCN2 C-linker/CNBD short	+	-	-
mHCN2 C-linker/CNBD long	+	-	-

Table 6 The interaction between short and long HCN constructs and full-length Mints was tested using the yeast two-hybrid assay. Activity was detected by transactivation of a GFP reporter gene. The symbol + in the table indicates fluorescence, whereas the – symbol indicates no detectable fluorescence and no cell growth.

Table 6 summarizes the results obtained for the tested interaction between the full-length Mint1 and 2 with the long and short C-linker/CNBD constructs of both mHCN1 and 2.The negative control (pEG202 co-transformed with all the bait constructs) is negative in all the experiments as expected. In addition, the positive controls are correct: Munc18-1 protein interacts with both Mint1 and 2 full-length constructs, meaning that Mint proteins are functional. miniTRIP8b protein also interacts with all the C-linker/CNBD constructs demonstrating that they are all functional and able to interact.
As shown in table 6, for both the two full-length constructs of Mint1 and Mint2 no interaction was detected with HCN C-linker/CNBD constructs.
During this experiment, I noticed that the yeast expressing the full-length Mint1 and 2 constructs was growing slower and with smaller colonies with respect to the miniTRIP8b expressing one. This is likely to be because the full-length Mint protein expression results to be toxic for yeast. In order to test whether a better protein expression could reveal a weak binding with HCN constructs, I

cloned the MID domain of both Mint1 (from residue 1 to 446) and Mint2 (from residue 1 to 356) into pJG4-5. The expression of two MID domains in yeast resulted in better growing rates with respect to the full-length constructs. I repeated the experiment testing whether the two MID domains could interact with the two C-linker/CNBD constructs of mHCN1.

	Bait (pJG4-5)		
Prey (pEG202)	miniTRIP8b (positive control)	Mint1 MID	Mint2 MID
Empty vector (negative control)	-	-	-
Munc18-1 (positive control)	-	+	+
mHCN1 C-linker/CNBD short	+	-	-
mHCN1 C-linker/CNBD long	+	-	-

Table 7 The interaction between short and long HCN1 constructs and the MID domains of Mints was tested using the yeast two-hybrid assay. Activity was detected by transactivation of a GFP reporter gene. The symbol + in the table indicates fluorescence, whereas the – symbol indicates no detectable fluorescence and no cell growth.

As shown in table 7, all the positive and negative controls are giving the expected results. However, as shown for the full-length constructs, no interaction was detected between the MID domain of both Mint1 and 2 and the two mHCN1 constructs.

4.2.4 Investigating the role of the N-terminus in the interaction with Mint proteins

A number of hypothesis can be made to explain the negative results of the yeast two-hybrid assay. A likely explanation can be, for instance, that the interaction between Mints and the full length HCN channels is favoured by the presence of the other cytosolic domain of HCN channels, the N-terminus.

I decided to test whether the N-domain of the channel could take part in the interaction. From the electrophysiological results previously shown, it is known that the full-length channel mHCN2 undergoes a Mint-induced current decrease as long as it possesses the D and E helices of the CNBD. No sequence downstream of these two helices is important for the interaction. Therefore, if there is another part of the channel that is involved in the interaction, it must be located upstream of the C-linker/CNBD region. One candidate for this interaction could be the conserved cytoplasmic N-terminal "HCN domain". This is a structured domain recently identified in the cryoEM structure of HCN1 (Lee & Mackinnon 2017). It forms a three helices complex that apparently interact with the C-linker and the CNBD of the HCN1 channel. So far, it is not clear its regulatory role. It has been proven that it is not possible to test its role by removing the HCN domain from the channel

because, when expressed in HEK 293T cells the mutant channel undergoes trafficking defects and does not reach the plasma membrane (Tran et al. 2002). For this reason, I decided to test the interaction of the HCN domain and Mint proteins in yeast. To this aim, the HCN domain of mHCN2 (Fig.43 from residue L_{136} to residue G_{137}) was cloned into the prey vector pEG202.

$_{136}$LQRQFGALLQPGVNKFSLRMFGSQKAVEREQERVKSAG$_{173}$

Figure 43 HCN domain sequence cloned into the pEG202 vector for the yeast two-hybrid assay.

Yeast cells were co-transformed with the pGNG1 vector, the prey pEG202::mHCN2 HCN domain and the baits pJG4.5::Mint1 and 2 full-length.

	Bait (pJG4-5)	
Prey (pEG202)	Mint1 full-lenght	Mint2 full-lenght
mHCN2 HCN domain	-	-

Table 8 The interaction between the N-terminal HCN domain and the full-length Mint proteins was tested using the yeast two-hybrid assay. Activity was detected by transactivation of a GFP reporter gene. The symbol + in the table indicates fluorescence, whereas the – symbol indicates no detectable fluorescence and no cell growth.

In table 8, the results of the experiment are summarized and they show that there is no interaction between the HCN domain of mHCN2 and Mint1 and 2 full-length constructs, meaning that this domain alone is not able to directly interact with Mint proteins. These results show that the HCN domain does not interact directly with the Mint protein, at least *in vitro*. It is still possible that for the interaction the N-terminus requires the presence of the Clinker/CNBD fragment of HCN. Another possibility is that the *in vitro* interaction with Mints, requires a tetrameric conformation of the CNBD, which is precluded in our assay.

As a final check, I wanted to test whether the extreme N-terminus (the sequence upstream of the HCN domain, aa 1 to 130 in mHCN2) was involved with the D and E helices in the interaction with Mint proteins. In this case, the interaction was analysed electrophysiologically. To this aim, I produced a mutant of mHCN2 lacking both the extreme N-terminus (sequence deleted from residue 2 to 130) and the C-terminus after the E helix of the CNBD. This mutant, named mHCN2 nt αD/Estop, was co-expressed alone (with EGFP, as control) and with EGFP-Mint2 in HEK293T and cell currents were recorded. Figure 44A shows the two normalized activation curves of the wild-type (in black) and mutated (in magenta) channel. As expected and reported in literature (Chen et

al. 2000), the magenta curve is shifted towards more negative potentials (left shift of the activation curve) with respect to the wild-type one (black curve).

In Figure 44B, the normalized currents of the full-length and nt αD/Estop channels in the presence or absence of EGFP-Mint2 are represented. First of all, it is possible to notice that the current of the mutated channel (magenta full circles) is decreased with respect of the wild-type one (black full circles); this reduction of the current is due to the removal of the N-terminus of the channel as published in Chen et al. 2000. The co-expression of both channels with EGFP-Mint2 causes a decrease of the currents (magenta and black empty symbols), meaning that, despite the lack of the extremely N-terminus, the channel is still able to interact with its interactor and thus that the N-terminus is not involved in complex formation.

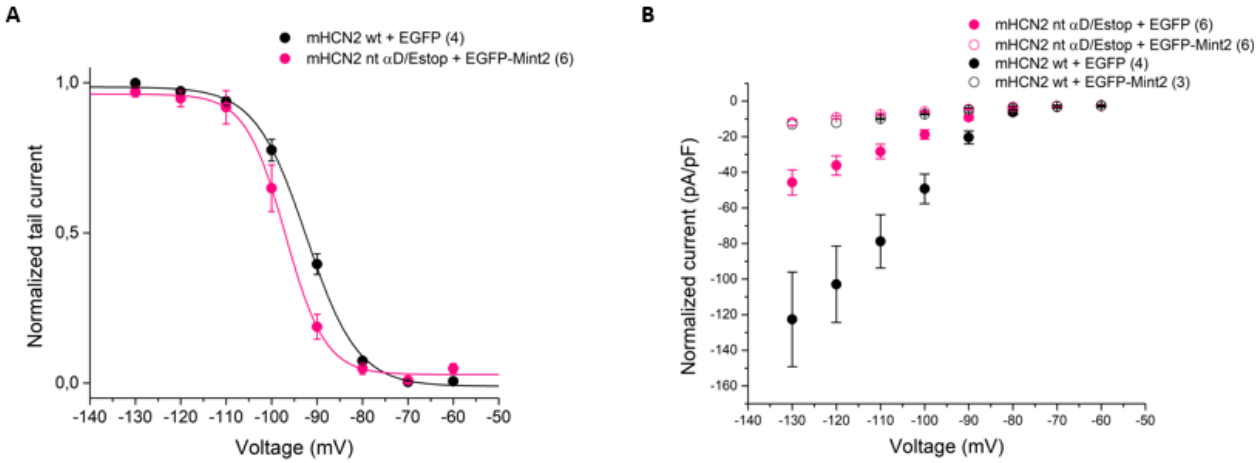

Figure 44 Effect of Mint2 co-expression on the full-length and deleted (nt αD/Estop) mHCN2. ***A.*** *Mean tail current activation curves of mHCN2 full-length (wt) + EGFP (black filled line and circles, n=4) and of mHCN2 nt αD/Estop with EGFP-Mint2 (magenta filled line and circles, n=6). Lines show fits of a Boltzmann function. $V_{1/2}$ of mHCN2 wt+ EGFP = -92.4 ± 0.4 mV; $V_{1/2}$ of mHCN2 nt αD/Estop + EGFP = -97 ± 0.3 mV. The values are statistically significant (P > 0.05).* ***B.*** *Mean steady state current/voltage relations of mHCN2 wt + EGFP (black filled circles, n=6) and mHCN2 wt + EGFP-Mint2 (black open circles, n=6), mHCN2 nt αD/Estop + EGFP (magenta filled circles, n=4), mHCN2 nt αD/Estop + EGFP-Mint2 (magenta open circles, n=3).*

5. CONCLUSION AND FUTURE PROSPECTS

In my thesis, I studied the interaction between the neuronal HCN channels and two other proteins: TRIP8b and Mints.

5.1 HCN - TRIP8b interaction

Ionic channels are involved in a wide number of physiological processes and are composed by the assembly of different subunits. The auxiliary β subunits are able to modulate the trafficking and the biophysical properties of the pore forming α subunits (Arikkath & Campbell 2003).

During my PhD thesis, I studied one of the two binding sites responsible for interaction between HCN channels and their β subunits TRIP8b. This binding region, named upstream binding site, is responsible for TRIP8b regulation of cAMP effect on the gating of the channel (Santoro et al. 2011). By means of solution NMR, the two regions of the CNBD were identified to compose together the upstream binding site: the C-helix and the N-bundle loop (Saponaro et al. 2014). Using site-directed mutagenesis, I tried to identify residues in these two regions important for complex formation. The final aim of this study was to obtain an HCN mutant unable to interact with TRIP8b at the upstream binding site, but still sensitive to cAMP. This will prevent regulation of channel activity by its β subunit without affecting regulation of channel trafficking (due to the interaction at the downstream binding site). I could not find a mutation in the C-helix that selectively affects TRIP8b binding and not cAMP affinity. On the contrary, in the N-bundle loop I found a double mutation ($N_{547}D/A_{548}C$) able to impair selectively TRIP8b regulation, but not the one of cyclic nucleotide. Moreover, this mutation does not alter the trafficking effect of TRIP8b on HCN channels. On this background, this mutation is the perfect candidate to become a genetic tool to understand the importance of the fine cAMP/TRIP8b regulation in HCN channels in some brain regions, such as in the hippocampus (see paragraph 2.7). This mutation results particularly important and advantageous since the only other possibility of studying this binary regulation of HCN channels would be the TRIP8b *knock-out* mouse model. However, the problem of this model is that knocking out TRIP8b protein, HCN channels will also lose their TRIP8b-dependent trafficking, and thus the proper distribution of the channels.

Another interesting point, obtained from the site directed mutagenesis screening, concerns the importance of the N-bundle loop in cAMP signal propagation from the CNBD up to the pore domain of the channel. In fact, the single mutation $N_{547}D$ showed a reduced affinity for the cyclic nucleotide, even though the mutation is upstream of cAMP binding site. The obtained result

underlines the involvement of the N-bundle loop in cAMP affinity regulation and signal propagation.

5.2 HCN – Mint interaction

Two studies showed that HCN1 and 2 were able to interact with Mint1 and 2 proteins (Kimura et al. 2004; Saito et al. 2012), even though the functional role of this interaction was never investigated. In my thesis, the effect of Mint proteins on channel properties was analysed for the first time. I found that the interaction between the two proteins results in a reduction of HCN current in HEK293T cells. This current decrease is specific, since it is not reproducible with other channels (such as KAT1 and hERG).

In order to test whether this current reduction was due to the decrease of the channels present in the plasma membrane, I expressed an extracellular tagged HCN2 channel (HCN2 HA tag) in HEK293T cells. After Mint2 co-expression, I found the amount of the HA tagged channel present in the plasma membrane of non permeabilized cells reduced. Moreover, upon Mint2 co-expression, HCN2 channel undergoes a redistribution in a perinuclear region within the cell.

In order to understand the identity of this compartment, I started using antibodies specific for the trans-Golgi compartment (TGN-46 Millipore) and for the autophagosome (LC3A/B Cell Signaling) (data not shown). Unfortunately, the results obtained so far show that the staining was not specific for both the antibodies. However, I am currently working on the identification of this cell compartment by changing the primary antibodies of the Golgi compartment to obtain a specific staining.

In conclusion, I showed in HEK293T cells that Mint2 binding alters HCN2 trafficking, and this results in a channel current reduction.

For what it concerns the sequences required for the interaction of Mint 1 and 2 to HCN channels, first of all I confirmed that the N-terminal region of Mint 1 and 2 (named MID domain) is necessary for the interaction (Kimura et al. 2004). When the MID domain is not present, as in Mint3, the interaction and thus the current decrease are lost. In the future, it would be interesting to reduce and identify the binding site. In fact, the long N-terminal region is not well conserved between Mint1 and Mint2 except for a 12 amino acids sequence, which could represent the binding site for HCN channels.

For HCN channels, it was already known that the C-terminal region after the C-helix of the CNBD was important for the interaction (Kimura et al. 2004). For the first time, in my thesis, the region

important for the interaction was reduced to the D and E helices of the CNBD. These two helices are important for the interaction of both Mint1 and 2, meaning that they require the same region of the CNBD of HCN2. The next step will be to understand which of the two helices is necessary. Then, it will be interesting to test whether also in HCN1 these two helices represent the interaction region for Mints.

Notably, Mint proteins interact with the CNBD of HCN2, which also constitutes the binding site for cAMP and TRIP8b. In the future, it would be intriguing to test whether Mints can affect HCN affinity for the cyclic nucleotide. In fact, in preliminary studies in our lab, we noticed that the cAMP affinity of the CNBD containing the D and E helices is higher with respect of the CNBD without the two helices (unpublished data). Thus, these two helices are important in regulating cAMP affinity.

Moreover, *in vivo*, in pyramidal neurons and stellate cells, HCN channels are associated to TRIP8b. In the future, it would be interesting to assess the effects of Mint 1 and 2 on HCN channels expression and function in the presence of TRIP8b. It could be investigated whether Mint proteins interfere with TRIP8b binding and vice versa, since they both interact with the CNBD.

In this work, with the aim of studying and characterizing this new interaction between HCN channels and Mint proteins, I tried some direct binding assays in *E.coli* and yeast since there is no evidence in literature of a direct interaction between these proteins. Unfortunately, the co-expression and co-purification assay in *E.coli* encountered the problem of the aspecific binding of the protein tags (the MBP at first, and then the GST). I therefore decided to change technique and to use the yeast two-hybrid assay, but no direct interaction was detectable. One possible reason why these two experiments did not detect a direct interaction could be that the channel needs to be in its tetrameric form in order to be recognized and bound by Mint proteins. In fact, in *E.coli* the used construct lacked of the C-linker region, which is the responsible for the tetramerization of the channel. Moreover, in yeast, even though the constructs included the C-linker, it is possible that they could not form tetramers since they were fused to other proteins. In addition to the fact that tetramerization is needed, it is also possible that the binding is weak. Still, it is also true that from my results I cannot exclude the possibility that the binding is indirect.

Finally, Mint1 and 2 are known to bind the cytoplasmic tail of the amyloid precursor protein (APP) through their phosphotyrosine binding domain (PTB), and to regulate APP trafficking and metabolism (Rogelj et al. 2006). An intriguing hypothesis is that Mint 1 and 2 may act as a bridge between HCN channels and APP, resulting in the formation of a ternary complex. This could

suggest the existence of a link between HCN channels and the APP processing pathway. It has been shown that reduced HCN1 channel function can increase the amount of toxic peptides produced in Alzheimer's disease (Saito et al. 2012). This is the reason why it is important to study and characterize the interaction between HCN channels and Mints.

6. REFERENCES

Altomare, C. et al., 2003. Heteromeric HCN1 – HCN4 channels : a comparison with native pacemaker channels from the rabbit sinoatrial node. , pp.347–359.

Arikkath, J. & Campbell, K.P., 2003. Auxiliary subunits: essential components of the voltage-gated calcium channel complex. *Current opinion in neurobiology*, 13(3), pp.298–307.

Biel, M., 2009. Review HCN channels : Structure , cellular regulation and physiological function. , 66, pp.470–494.

Brown, H.F., DiFrancesco, D. & Noble, S.J., 1979. How does adrenaline accelerate the heart? *Nature*, 280(5719), pp.235–236.

Chen, J. et al., 2000. Functional Roles of Charged Residues in the Putative Voltage Sensor of the HCN2 Pacemaker Channel *. , 275(46), pp.36465–36471.

DiFrancesco, D., 1993. Pacemaker Mechanisms in Cardiac Tissue. *Annual Review of Physiology*, 55(1), pp.455–472. Available at: https://doi.org/10.1146/annurev.ph.55.030193.002323.

Halliwell, J. V & Adams, P.R., 1982. Voltage-clamp analysis of muscarinic excitation in hippocampal neurons. *Brain Research*, 250(1), pp.71–92. Available at: http://www.sciencedirect.com/science/article/pii/0006899382909544.

Han, Y. et al., 2011. Trafficking and Gating of Hyperpolarization-activated Cyclic Nucleotide-gated Channels Are Regulated by Interaction with Tetratricopeptide Repeat-containing Rab8b-interacting Protein (TRIP8b) and Cyclic AMP at Distinct Sites * □.

Hu, L. et al., 2013. Binding of the auxiliary subunit TRIP8b to HCN channels shifts the mode of action of cAMP.

Kimura, K. et al., 2004. Hyperpolarization-activated, cyclic nucleotide-gated HCN2 cation channel forms a protein assembly with multiple neuronal scaffold proteins in distinct modes of protein-protein interaction. *Genes to Cells*, 9(7), pp.631–640.

L. Zhou and S. Siegelbaum, 2007. *Gating of HCN channels by cyclic nucleotides: residue contacts that underlie ligand binding, selectivity and efficacy*,

Lee, C. & Mackinnon, R., 2017. Structures of the Human HCN1 Hyperpolarization-Activated Channel. *Cell*, 168(1–2), p.111–120.e11. Available at: http://dx.doi.org/10.1016/j.cell.2016.12.023.

Lewis, A.S. et al., 2009. Alternatively Spliced Isoforms of TRIP8b Differentially Control h Channel Trafficking and Function. , 29(19), pp.6250–6265.

Ludwig, A. et al., 1998. A family of hyperpolarization-activated mammalian cation channels. *Nature*, 393(6685), pp.587–591.

Luthi, A. & McCormick, D.A., 1998. H-current: properties of a neuronal and network pacemaker. *Neuron*, 21(1), pp.9–12.

Maccaferri, G. & McBain, C.J., 1996. The hyperpolarization-activated current (Ih) and its contribution to pacemaker activity in rat CA1 hippocampal stratum oriens-alveus interneurones. *The Journal of physiology*, 497 (Pt 1), pp.119–130.

Magee, J.C., 1998. Dendritic Hyperpolarization-Activated Currents Modify the Integrative Properties of Hippocampal CA1 Pyramidal Neurons. , 18(19), pp.7613–7624.

Magee, J.C. & Carruth, M., 1999. Dendritic Voltage-Gated Ion Channels Regulate the Action Potential Firing Mode of Hippocampal CA1 Pyramidal Neurons. , pp.1895–1901.

Marcelin, B., Lugo, J.N., et al., 2012. Differential Dorso-ventral Distributions of Kv4 . 2 and HCN Proteins Confer Distinct Integrative Properties to Hippocampal CA1 Pyramidal Cell Distal Dendrites * □. , 287(21), pp.17656–17661.

Marcelin, B., Liu, Z., et al., 2012. Dorsoventral Differences in Intrinsic Properties in Developing CA1 Pyramidal Cells Be. , 32(11), pp.3736–3747.

Moosmang, S. et al., 2001. Cellular expression and functional characterization of four hyperpolarization-activated pacemaker channels in cardiac and neuronal tissues. *European journal of biochemistry*, 268(6), pp.1646–1652.

Nakajima, Y. et al., 2001. Neuronal expression of mint1 and mint2, novel multimodular proteins, in adult murine brain. *Molecular Brain Research*, 92(1–2), pp.27–42.

Nolan, M.F. et al., 2007. HCN1 channels control resting and active integrative properties of stellate cells from layer II of the entorhinal cortex. *The Journal of neuroscience : the official journal of the Society for Neuroscience*, 27(46), pp.12440–12451.

Okamoto, M. & T C, S., 1997. Mints, Munc 18-interacting proteins in synaptic vesicle exocytosis. *The Journal of biological chemistry*, 272(50), pp.31459–31464. Available at: papers2://publication/uuid/EC839BC0-AAFA-4B28-A12B-9B4EEF2FB606.

Robinson, R.B. & Siegelbaum, S.A., 2003. H YPERPOLARIZATION -A CTIVATED C ATION C URRENTS : From Molecules to Physiological Function. , (4).

Robinson, R.B. & Siegelbaum, S. a, 2003. Hyperpolarization-activated cation currents: from molecules to physiological function. *Annual review of physiology*, 65(4), pp.453–80.

Rogelj, B. et al., 2006. The X11/Mint family of adaptor proteins. *Brain Research Reviews*, 52(2), pp.305–315.

Saito, Y. et al., 2012. Hyperpolarization-activated cyclic nucleotide gated channels: a potential molecular link between epileptic seizures and Aβ generation in Alzheimer's disease. *Molecular neurodegeneration*, 7(1), p.50. Available at:

http://www.molecularneurodegeneration.com/content/7/1/50.

Santoro, B. et al., 2009. Article TRIP8b Splice Variants Form a Family of Auxiliary Subunits that Regulate Gating and Trafficking of HCN Channels in the Brain. *Neuron*, 62(6), pp.802–813. Available at: http://dx.doi.org/10.1016/j.neuron.2009.05.009.

Santoro, B. et al., 2000. Molecular and Functional Heterogeneity of Hyperpolarization- Activated Pacemaker Channels in the Mouse CNS. , 20(14), pp.5264–5275.

Santoro, B. et al., 2011. TRIP8b Regulates HCN1 Channel Trafficking and Gating through Two Distinct C-Terminal Interaction Sites. , 31(11), pp.4074–4086.

Santoro, B., Wainger, B.J. & Siegelbaum, S.A., 2004. Regulation of HCN Channel Surface Expression by a Novel C-Terminal Protein – Protein Interaction. , 24(47), pp.10750–10762.

Saponaro, A. et al., 2014. Structural basis for the mutual antagonism of cAMP and TRIP8b in regulating HCN channel function. , 111(40).

Steriade, M., McCormick, D.A. & Sejnowski, T.J., 1993. Thalamocortical oscillations in the sleeping and aroused brain. *Science (New York, N.Y.)*, 262(5134), pp.679–685.

Tran, N. et al., 2002. A Conserved Domain in the NH 2 Terminus Important for Assembly and Functional Expression of Pacemaker Channels *. , 277(46), pp.43588–43592.

Wainger, B.J. et al., 2001. Molecular mechanism of cAMP modulation of HCN pacemaker channels. , 411(June), pp.805–810.

Yu, F.H. et al., 2005. Overview of molecular relationships in the voltage-gated ion channel superfamily. *Pharmacological reviews*, 57(4), pp.387–395.

Zagotta, W.N. et al., 2003. Structural basis for modulation and agonist specificity of HCN pacemaker channels. , 425(September), pp.200–205.

Zolles, G. et al., 2009. Article Association with the Auxiliary Subunit PEX5R / Trip8b Controls Responsiveness of HCN Channels to cAMP and Adrenergic Stimulation. , pp.814–825.

PART II

CONTENTS

- Saponaro A., Pauleta SR., Cantini F., Matzapetakis M., Hammann C., Donadoni C., Hu L., Thiel G., Banci L., Santoro B., Moroni A. “Structural basis for the mutual antagonism of cAMP and TRIP8b in regulating HCN channel function”. 2014, PNAS.

- Saponaro A., Cantini F., Porro A., Bucchi A., Maione V., Donadoni C., Introini B., Di Francesco D., Thiel G., Banci L., Santoro B., Moroni A. “Bimodal interaction between HCN channels and TRIP8b revealed through structural characterization of the protein complex”. 2017, submitted in PNAS.

PART III

MATHERIALS AND METHODS OF HCN-MINT INTERACTION

1. HEK293T electrophysiology

HEK293T cells were co—transfected with Turbofect transfection reagent (ThermoFisher Scientific). For each 35 mm petri dish, 1 μg of HCN1 or HCN2 cDNA (pIRES::mHCN1 from A. Bucchi; pCI::mHCN2 from B. Santoro) was used plus 1 μg of EGFP (as control, pmaxGFP AmaxaBiosystems) or 1 μg of Mint proteins cDNA (pEC::rMint1, pEC::rMint2 and pEC::rMint3 from B.Santoro). The constructs of the deleted mHCN2 (pCI vector) channels were obtained by inserting two codon stops after residues 643, 679 and 813 with the QuikChange Lightning Site-Directed Mutagenesis Kit (Agilent, #210519).

Transfected cells were detected by GFP fluorescence.

For the recordings, the extracellular solution used was: 110 mM NaCl, 30 mM KCl, 1.8 mM $CaCl_2$, 0.5 mM $MgCl_2$ and 5 mM HEPES–KOH buffer (pH 7.4). Recording pipettes were fabricated from 1.5mm o.d. borosilicate glass capillaries with a P-97 Flaming/Brown Micropipette Puller (Sutter, Novato, CA, USA) and had resistances of 3–5MΩ. The pipettes were filled with the following intracellular solution: 10 mM NaCl, 130 mM KCl, 1 mM EGTA, 0.5 mM $MgCl_2$, 2 mM MgATP and 5 mM HEPES–KOH buffer (pH 7.4).

Currents were recorded in whole cells configuration with a Dagan 3900A (Degan, Minneapolis, MN, USA). Data were digitized with an Axon Digidata 1322 A/D (Axon Instruments, CA, USA) converter and analysed with Axon pClamp9. To obtain channel activation, cells were held at -40 mV and then hyperpolarizing steps (from -160 to -25 mV) of variable duration were applied in order to reach steady-state activation at all voltages. After, current tails were measured by returning to -40mV. To analyse current density, the steady-state current amplitude was measured at the end of each test potential, and normalized to cell capacitance. Mean activation curves were obtained by fitting maximal tail current amplitude, plotted against the voltage step applied, with the Boltzmann equation It=It(max)/(1+exp(V-V1/2)/k. It stands for the current amplitude of the tail current recorded for a given pre-pulse, It(max) is the maximum current amplitude of the tail current, V is the voltage of the pre-pulse, $V_{1/2}$ is the half-activation voltage and k is the slope factor in mV using Originpro software (Originlab, Northampton, MA, USA). Unpaired Student's tests (Origin software) was used to make comparisons. All data are shown as mean ± S.E.M.

2. Immunocytochemistry

HEK293T cells were transfected with Turbofect transfection reagent (ThermoFisher Scientific) or X-tremeGENE™ HP DNA Transfection Reagent (Roche). Cells were washed in PBS, fixed in 4% PFA, washed in PBS and blocked with PBS + 0.1% Triton X-100 + 3% Normal Goat Serum (ThermoFisher Scientific). Triton X-100 was not used for not permeabilizing conditions. Incubation with primary and secondary antibodies was performed in PBS + 3% Normal Goat Serum. Primary antibodies used: anti-HA (12CA5) (Roche, 1:500), anti-HCN2 (Neuromab, 1:250).
Secondary antibodies used: Goat anti-Mouse IgG2b Alexa Fluor 546 (ThermoFisher Scientific, 1:1000, A-21143), Goat anti-Mouse IgG (H+L) Alexa Fluor 647 (ThermoFisher Scientific, 1:400).

3. Western Blot on HEK293T cell lysate

HEK293T cells were transfected with Turbofect transfection reagent (ThermoFisher Scientific). For each 35 mm petri dish, 1µg of HCN1 or 2 (pIRES::mHCN1 from A. Bucchi; pCI::mHCN2 from B. Santoro) was used plus 1 µg of EGFP (as control, pmaxGFP AmaxaBiosystems) or 1 µg of Mint proteins cDNA (pEC::rMint1, pEC::rMint2, pEC::rMint3 and pEC::TRIP8b(1a-4) from B.Santoro). Cells were lysed in the lysis buffer (150 mM NaCl, 10 mM Tris-Cl pH 7.4, 2 mM EDTA, 1% Triton X-100) with protease inhibitors (Complete Mini, Roche). Cell lysates were kept in ice for 30 minutes and then centrifuged. The surnatant protein concentration was calculated with Pierce BCA protein assay kit (ThermoFisher Scientific #23225). For the Western Blot analysis of protein expression, cell lysates were run on 4-12% SDS-PAGE (ThermoFisher Scientific), transferred to a polyvinyldene difluoride membrane (PVDF, Bio-Rad) in transfer buffer (192 mM glycine, 25 mM Tris-HCl, 20% methanol). Membranes were blocked in TBST + 2% BSA. Primary antibodies incubation was performed in over-night at 4°C in TBST + 2% BSA. Primary antibodies used: anti-HCN1 RTQ (Millipore, 1:1000) and anti-HCN2 (APC-030 Alomone, 1:300). After being washed in TBST, membranes were incubated with secondary antibodies in PBS + 5% w/v milk. Secondary antibodies used: HRP-conjugate anti-rabbit (1:10000, Cell Signaling Technology #7074) and HRP-conjugate anti-mouse (1:10000, Cell Signaling Technology #7076). Protein bands were detected with SuperSignal West Pico chemiluminescent substrate (ThermoFisher Scientific #34080).

4. Protein co-expression and co-purification

In pGEX-6P-2rb, the cDNA of MID domain of the rat isoform Mint2 (from residue 1 to residue 356) was cloned BamHI/EcoRI. In pET24b, the cDNA of the short HCN2 CNBD (from residue 521 to 672 of the human isoform) and the one of the long HCN2 CNBD (from residue 594 to 676 of the murine isoform) were cloned with the LIC system.

Plasmids were co-transformed in *E.coli* BL21 Rosetta strain (Novagen). Cells were grown at 37°C and induced with IPTG 0.4Mm at OD_{600}=0.6. Three hour after induction, cells were harvested by centrifugation. Pellets were re-suspended in ice-cold lysis buffer (PBS + 5 mM β-mercaptoethanol, 5 µg/ml leupeptin, 1µg/ml pepstatin, 100 µM phenylmethylsulphonyl chloride, 10 µg/ml DNase and 0.25 mg/ml lysozyme). The lysate was sonicated 16 times 20 seconds, and then centrifuged 30 min 20000 x *g*. All purification steps were performed at 4 °C and monitored using the AKTApurifier UPC 10 fast protein liquid chromatography system (GE Healthcare). For the affinity purification, the GSTrap 4B column (GE Healthcare) was used. Protein complex was eluted in 50 mM TrisHCl pH8 + 10 mM reduced glutathione. The elution was loaded into a HiLoad 16/60 Superdex 75 prep grade size exclusion column (GE Healthcare). The fractions corresponding to the peaks were analysed by SDS-PAGE and Western blot. Anti-polyHistidine (mouse monoclonal, 1:1000, Sigma-Aldrich H1029) was used as primary antibody and goat anti-mouse IgG antibody linked to the Alkaline Phosphatase (1:1000, Sigma-Aldrich A3688) was used as secondary antibody. For protein detection, SIGMAFAST™ BCIP®/NBT tablets (Sigma-Aldrich) was used.

5. Yeast two-hybrid assay

Assays were performed using the Grow'N'Glow Two-Hybrid kit (Bio 101) and yeast strain EGY48. In vector pEG202 the following bait constructs were cloned: mHCN1 C-linker/CNBD short (from residue 390 to 592) and long (from residue 390 to 625), mHCN2 C-linker/CNBD short (from residue 443 to 643) and long (from residue 443 to 676), Munc18-1 (full-length). In pJG4-5 the prey constructs were cloned: miniTRIP8b (used as positive control, from residue 236 to 316 of TRIP8b(1b-2) (Santoro et al. 2011)), Mint1 full-length (rat isoform), Mint1 MID (rat isoform, from residue 1 to 446) ,Mint2 full-length (rat isoform), Mint2 MID (rat isoform, from residue 1 to 356). Cloning was performed with In-Fusion® HD Cloning Kit (Takara Bio USA).

Bait and prey plasmids were co-transformed with the reporter plasmid pGNG1 with the Frozen-EZ yeast transformation II kit (Zymo Reasearch). After transformation, cells were plated onto glucose-containing medium. Transformants were restreaked on selective medium (galactose+/leucine-), and after 3–5 days of growth, they are screened for positive GFP expression under a UV light.

Structural basis for the mutual antagonism of cAMP and TRIP8b in regulating HCN channel function

Andrea Saponaro[a], Sofia R. Pauleta[b], Francesca Cantini[c], Manolis Matzapetakis[d], Christian Hammann[e], Chiara Donadoni[a], Lei Hu[f], Gerhard Thiel[g], Lucia Banci[c], Bina Santoro[f], and Anna Moroni[a,1]

[a]Department of Biosciences, University of Milan, 20133 Milan, Italy; [b]Rede de Química e Tecnologia/Centro de Química Fina e Biotecnologia (REQUIMTE/CQFB), Departamento de Química, Faculdade de Ciências e Tecnologia, Universidade Nova de Lisboa, 2829-516 Caparica, Portugal; [c]Centro Risonanze Magnetiche (CERM) and Departement of Chemistry, University of Florence, 50019 Sesto Fiorentino, Italy; [d]Instituto de Tecnologia Química e Biológica António Xavier, Universidade Nova de Lisboa, 2780-157 Oeiras, Portugal; [e]School of Engineering and Science, Molecular Life Sciences Research Center, Jacobs University Bremen, DE-28759 Bremen, Germany; [f]Department of Neuroscience, Columbia University, New York, NY 10032; and [g]Membrane Biophysics, Technical University of Darmstadt, 64287 Darmstadt, Germany

Edited by Christopher Miller, Howard Hughes Medical Institute, Brandeis University, Waltham, MA, and approved August 7, 2014 (received for review June 4, 2014)

cAMP signaling in the brain mediates several higher order neural processes. Hyperpolarization-activated cyclic nucleotide-gated (HCN) channels directly bind cAMP through their cytoplasmic cyclic nucleotide binding domain (CNBD), thus playing a unique role in brain function. Neuronal HCN channels are also regulated by tetratricopeptide repeat-containing Rab8b interacting protein (TRIP8b), an auxiliary subunit that antagonizes the effects of cAMP by interacting with the channel CNBD. To unravel the molecular mechanisms underlying the dual regulation of HCN channel activity by cAMP/TRIP8b, we determined the NMR solution structure of the HCN2 channel CNBD in the cAMP-free form and mapped on it the TRIP8b interaction site. We reconstruct here the full conformational changes induced by cAMP binding to the HCN channel CNBD. Our results show that TRIP8b does not compete with cAMP for the same binding region; rather, it exerts its inhibitory action through an allosteric mechanism, preventing the cAMP-induced conformational changes in the HCN channel CNBD.

Hyperpolarization-activated cyclic nucleotide-gated (HCN1–4) channels are the molecular determinants of the h-current (I_h), which regulates critical neuronal properties, including membrane resting potential, dendritic excitability, and intrinsic rhythmicity (1). HCN channels are dually regulated by voltage and by binding of cAMP to the cyclic nucleotide binding domain (CNBD), which is found on the cytoplasmic C-terminal tail of the channel. The CNBD exerts a tonic inhibition on the channel pore, with the opening transition of the channel being allosterically coupled to the conformational changes in the CNBD induced by cAMP binding (2). Thus, the closed-to-open transition of the channel is thought to reflect the transition from the cAMP-free conformation to the cAMP-bound conformation of the CNBD, which stabilize, respectively, the closed and open states of the channel (2, 3). The C-linker, an α-helical folded domain that connects the CNBD to the pore region, conveys the regulation of channel gating from the CNBD to the pore (4–6). As a result of this allosteric mechanism, the binding of cAMP shifts the voltage dependence of the HCN channel opening to more positive potentials and increases maximal I_h at extreme negative voltages, where voltage gating is complete.

In addition to cAMP, HCN channels in the brain are regulated by auxiliary proteins, such as TRIP8b, a cytosolic β-subunit of neuronal HCN channels, which inhibits channel activation by antagonizing the effects of cAMP (7–9). We have previously shown that $TRIP8b_{core}$, an 80-aa sequence located in the TRIP8b protein core that directly interacts with the C-linker/CNBD region of HCN channels, is necessary and sufficient to prevent all of the effects of cAMP on the channel (10, 11). $TRIP8b_{core}$ decreases both the sensitivity of the channel to cAMP [half maximal concentration ($k_{1/2}$)] and the efficacy of cAMP in inducing channel opening [half activation voltage ($V_{1/2}$)]; conversely, cAMP binding inhibits these actions of TRIP8b. These mutually antagonistic effects are well described by a cyclic allosteric model in which TRIP8b binding reduces the affinity of the channel for cAMP, with the affinity of the open state for cAMP being reduced to a greater extent than the cAMP affinity of the closed state (11).

A second important action of TRIP8b is to reduce maximal current through HCN channels in the absence of cAMP (11). As a consequence, application of cAMP produces a larger increase in maximal I_h in the presence of TRIP8b than in its absence. The observation that TRIP8b exerts opposing influences on the two major actions of cAMP on HCN channel function, namely, reduces the effect of cAMP to shift the voltage dependence of channel gating but enhances the effect of cAMP to increase maximal current, has important implications for the ability of cAMP to modulate neuronal excitability in vivo. Thus, the relative extent by which neuromodulatory transmitters alter maximal I_h or shift the voltage dependence of HCN channel gating can vary widely among distinct classes of neurons (12–14). The differential expression of TRIP8b may provide a mechanistic explanation for this finding, because in neurons with high levels of TRIP8b expression, cAMP will exert a larger action to enhance maximal current, and a smaller

Significance

cAMP regulation of ion channels controls higher brain functions, such as sleep, memory, and cognition. Hyperpolarization-activated cyclic nucleotide-gated (HCN) channels are activated by the direct binding of cAMP to their cytoplasmic tail and inhibited by the neuronal β-subunit tetratricopeptide repeat-containing Rab8b interacting protein (TRIP8b), which prevents cAMP binding. Understanding the molecular mechanisms of regulation of this family of ion channels is critical because it pertains to the physiological processes and diseases associated with dysfunctions in the HCN current. Here, we explain the dual regulatory system of HCN2 channels in atomic detail. cAMP and TRIP8b do not compete for the same binding site on the HCN2 cytoplasmic tail; rather, they exert their mutual competition by promoting and stabilizing two different conformational states of the protein.

Author contributions: G.T., L.B., B.S., and A.M. designed research; A.S., C.D., and L.H. performed research; S.R.P., M.M., and C.H. contributed new reagents/analytic tools; A.S., S.R.P., F.C., M.M., and A.M. analyzed data; and A.S., F.C., B.S., and A.M. wrote the paper.

The authors declare no conflict of interest.

This article is a PNAS Direct Submission.

Data deposition: The atomic coordinates have been deposited in the Protein Data Bank, www.pdb.org (PDB ID code 2MPF) and in the BioMagResBank (BMRB ID code 19977).

See Commentary on page 14320.

[1]To whom correspondence should be addressed. Email: anna.moroni@unimi.it.

This article contains supporting information online at www.pnas.org/lookup/suppl/doi:10.1073/pnas.1410389111/-/DCSupplemental.

action to alter the voltage dependence of channel gating, compared with neurons in which TRIP8b expression is low. Such fine-tuning broadens the range of physiological actions that cAMP can exert to modulate neuronal firing.

In the present study, we address the structural basis for the mutually antagonistic effects of cAMP and TRIP8b on HCN channel function. Although our previous biochemical and electrophysiological data strongly support the hypothesis that TRIP8b and cAMP binding sites do not overlap, direct structural information on the TRIP8b–CNBD complex is required to validate the allosteric antagonism model of interaction between the two ligands. A plausible hypothesis for the antagonistic effect of TRIP8b and cAMP is that each of the two ligands stabilizes the CNBD in a conformation that decreases the affinity for the other. To test this hypothesis, we first generated the 3D structure of the cAMP-free HCN2 channel CNBD using solution NMR spectroscopy and then characterized its interaction with the $TRIP8b_{core}$ fragment. By comparing the cAMP-free with the available cAMP-bound HCN2 channel CNBD structure (15, 16), we reconstruct the full conformational changes induced by cAMP binding, revealing critical transitions occurring in the P- and C-helices of the CNBD, and further highlighting the role of the N-terminal helical bundle in transducing the movements of the CNBD to the channel pore. We next identify, through NMR titration, site-directed mutagenesis, and biochemical interaction assays, the binding site of $TRIP8b_{core}$ on the cAMP-free form of the HCN2 channel CNBD. Our results demonstrate that cAMP and TRIP8b do not directly compete for the same binding region and support a model of mutual allosteric inhibition between cAMP and TRIP8b. Finally, our results clarify the mechanism by which TRIP8b antagonizes the effect of cAMP on channel gating: TRIP8b directly interacts with two mobile elements that drive the ligand-induced conformational changes in the CNBD. TRIP8b binding to the CNBD therefore prevents the cAMP-induced transition and stabilizes the channel in the cAMP-free conformation.

Results

cAMP Destabilizes the $TRIP8b_{core}$–HCN2 C-Linker/CNBD Protein Complex. Electrophysiological experiments have shown that the antagonistic role of TRIP8b on the cAMP-dependent effects on HCN channel activity is due to the $TRIP8b_{core}$ fragment, the 80-aa core domain of the full-length TRIP8b protein that interacts with the C-linker/CNBD domain of the channels (10, 11). Furthermore, previous electrophysiological analysis and biochemical assays have suggested that native TRIP8b preferentially interacts with full-length HCN1 or HCN2 in the absence of cAMP, and that binding activity decreases with increasing cAMP concentration (11, 17). We therefore tested whether this behavior is also maintained in vitro between the isolated HCN2 C-linker/CNBD and $TRIP8b_{core}$ protein fragments. We coexpressed in *Escherichia coli* the His_6-maltose binding protein (MBP)–tagged C-linker/CNBD (hereafter, the $CNBD_{C\text{-}linker}$) and the Streptactin-binding (Strep)-tagged $TRIP8b_{core}$ protein fragments. The bacterial lysate was supplemented with increasing cAMP concentrations (from 0 to 1 mM), and the complex was subsequently purified using a nickel affinity column. Increasing cAMP concentration in the lysate decreased the amount of $TRIP8b_{core}$ protein copurified with the $CNBD_{C\text{-}linker}$, revealing the destabilizing effect of the cyclic nucleotide on TRIP8b–CNBD interaction (Fig. S1*A*). These results confirm that $TRIP8b_{core}$ and cAMP are competing for binding to the CNBD and that TRIP8b preferentially binds the cAMP-free conformation of the CNBD. The question remains as to whether a direct (for the same binding site) or indirect (allosteric) competition occurs between the two ligands. To answer this question, we used solution NMR spectroscopy to obtain the 3D structure of the HCN2 CNBD in the cAMP-free conformation and, subsequently, to map the TRIP8b binding site on the channel's CNBD.

Biophysical Characterization of the $TRIP8b_{core}$–CNBD Protein Complex. A shorter construct lacking the first three α-helices (αA′–αC′) of the HCN2 C-linker region (hereafter, the CNBD) was prepared to prevent the C-linker–driven tetramerization of the protein, which occurs at high concentrations (15, 18), and to reduce the fragment to a size within the optimal range for solution NMR experiments (17.9 kDa). To verify that the partial removal of the C-linker domain did not affect the interaction with $TRIP8b_{core}$, we first coexpressed the His_6-MBP–tagged CNBD with $TRIP8b_{core}$ in *E. coli* and purified the complex using the $TRIP8b_{core}$ Strep tag. As shown in Fig. S1*B*, the CNBD efficiently copurifies with $TRIP8b_{core}$, confirming that neither the complete C-linker domain nor the oligomerization of the HCN2 CNBD is required for the interaction with the $TRIP8b_{core}$ fragment. We further determined the thermodynamic parameters of this interaction by isothermal titration calorimetry (ITC). Fig. S1*C* shows that the interaction is exothermic. Analysis of the binding curve yields a stoichiometry of $n = 0.98 \pm 0.01$ and a calculated dissociation constant, K_d, of 1.30 ± 0.06 μM ($n = 3$). This finding is in agreement with the 1:1 stoichiometry recently determined for HCN2 and the full-length TRIP8b, using a single-molecule fluorescence bleaching method (19).

Structure of the Human HCN2 CNBD in the cAMP-Free Form and Ligand-Induced Conformational Changes. The structure of HCN2 CNBD in the cAMP-free form adopts the typical overall fold of CNBDs (20) (Fig. 1*A* and Fig. S2 *A* and *B*). Such a fold comprises an antiparallel β-roll that includes, between strands β6 and β7, the phosphate binding cassette (PBC), which forms the cAMP binding pocket (16); an N-terminal helical bundle, composed of an antiparallel helix–turn–helix motif formed by helices αE′ and αA; and two C-terminal helices, αB and αC, located at the

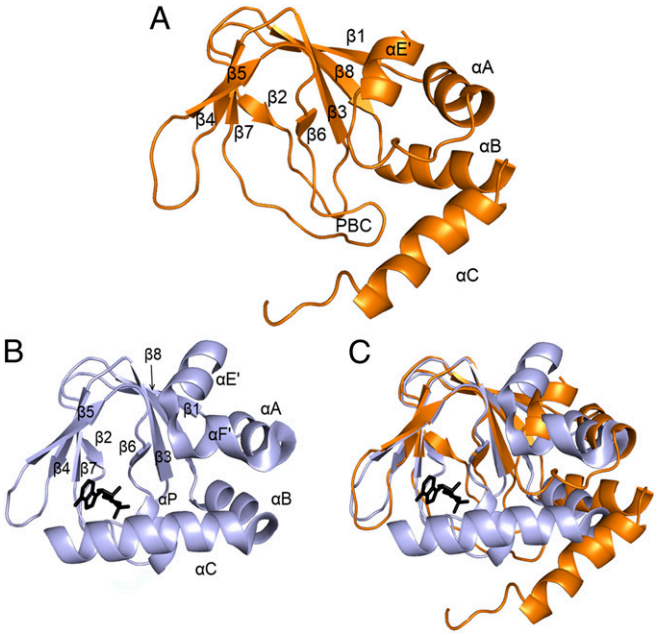

Fig. 1. cAMP-free structure of the human HCN2 CNBD and comparison with the bound structure. (*A*) Ribbon representation of the cAMP-free CNBD structure (orange). For better visualization of the structure, only one conformation of the unstructured C-terminal part of the C-helix (residues 659–663) is shown, whereas the unfolded region at the N terminus of the construct (residues 521–532) and the stretch following the C-helix (residues 664–672) are not shown. Secondary structure elements are labeled. (*B*) Ribbon representation of the X-ray cAMP-bound CNBD structure (gray) [PDB ID code 1Q5O (ref. 16)]. The cAMP molecule is shown in stick representation in black. (*C*) Superposition of the cAMP-free and cAMP-bound structures of the CNBD.

distal end of the CNBD. A comparison of the cAMP-free and cAMP-bound CNBD structures (Fig. 1 *A* and *B*) reveals clear differences between the two states of the HCN2 channel's CNBD (Fig. 1*C*), however. In particular, a number of major rearrangements are observed in the helical components of the CNBD, whereas less pronounced differences are observed in the β-roll. Indeed, the β-strands undergo only minor displacement upon ligand binding [Fig. 1*C*; C^{α} rmsd of 0.78 Å between cAMP-free (orange) and cAMP-bound forms (gray)]. In striking contrast, substantial changes occur in the helical components of the CNBD, as illustrated in detail in Fig. 2. Within the PBC element (Fig. 2 *A* and *B*), cAMP binding triggers the formation of the P-helix (residues 609–615; highlighted in red in Fig. 2*B*). The folding of the P-helix is instrumental in forcing residue Leu_{612} into a new configuration, which allows Phe_{638} located in the B-helix to approach the β-roll (residue movements highlighted by arrows in Fig. 2*A*; the B-helix moves by about 4.5 Å). Thus, following the displacement of Leu_{612}, the B-helix moves toward the cavity, together with the C-helix (Fig. 2*C*), with the two helices moving as rigid bodies toward the core of the CNBD (the angle between αB and αC is 125.05° in the cAMP-free form and 123.83° in the cAMP-bound form).

The structure of the cAMP-free HCN2 CNBD also reveals that the C-terminal region of the C-helix (residues 659–663) is unstructured (Fig. 2*C*), in agreement with the lack of medium- and long-range NOEs involving these residues (Fig. S2*C*). Residues 659–663 featured small $\{^1H\}$-^{15}N–NOE values (Fig. S2*D*), indicating that they experienced dynamics on the subnanosecond time scale in the cAMP-free form, which is consistent with a random-coil conformation. The C-helix is one helical turn longer in the cAMP-bound form (Fig. 2*D*). Thus, the formation of tight contacts between the side chains of Arg_{659} and Ile_{663} and the cAMP purine ring (16, 21) induces conformational changes in the backbone of the C-terminal part of the C-helix, which are critical in stabilizing the interaction between the cAMP molecule and the β-roll cavity.

Finally, the rearrangement of the PBC also indirectly induces the movement of the N-terminal helical bundle. By moving closer to the β-roll, the C-helix sterically displaces the N-terminal helical bundle, as shown in Fig. 2*E*. As a result, the E′-helix undergoes a major displacement, moving upward by about 5.5 Å; the loop (residues 543–549) connecting the E′- and A-helices is displaced upward by 5 Å, and forms a new helix (αF′) in the cAMP-bound form (Fig. 2*F*). Although the F′-helix is not present in the cAMP-free state, the analysis of ^{13}C chemical shifts, which reflect local conformation and thus secondary structural elements, nevertheless shows that three residues located in the corresponding loop (residues 543–545) do have a marked helix propensity.

In conclusion, the comparison between the cAMP-free and cAMP-bound structures of the HCN2 channel CNBD allows the first detailed description, to our knowledge, of the conformational changes induced by cyclic nucleotide binding in this protein. Such comparison highlights how, similar to other CNBDs, the binding of the cyclic nucleotide to the PBC causes the tightening of this element, which, in turn, drives the movement of the helices at both the N and C termini of the β-roll (Movie S1).

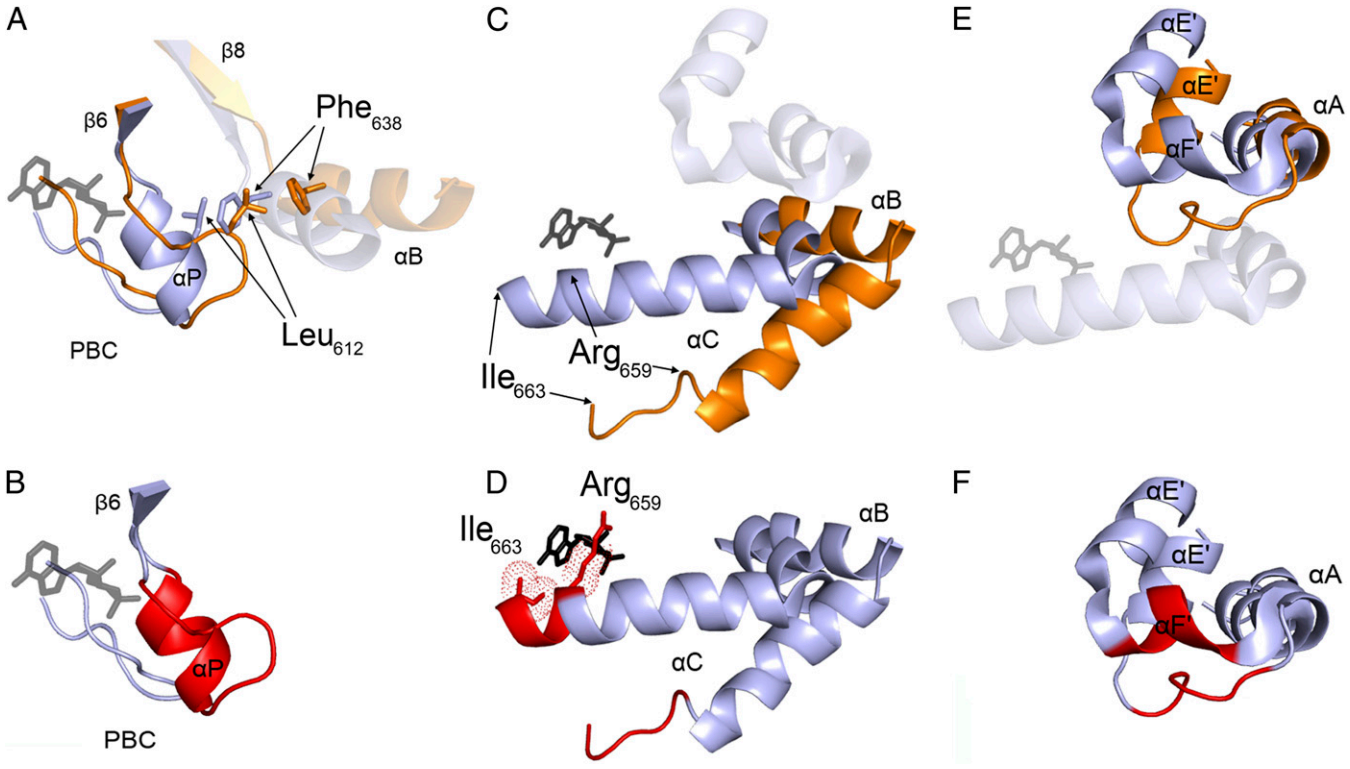

Fig. 2. Conformational changes in the helical components following cyclic nucleotide binding to the CNBD. (*A*) Close-up view of the PBC. The phosphate-sugar moiety of cAMP binds to the PBC, inducing its rearrangement. In the absence of cAMP, Leu_{612} of PBC occupies the space that is filled by Phe_{638} of the B-helix in the cAMP-bound conformation. (*B*) Highlighted in red is the portion of the PBC loop that folds into αP upon cAMP binding. (*C*) Translational movement of the B- and C-helices moving as a rigid body toward the cAMP molecule bound to the PBC. (*D*) Folding of the C-terminal portion of the C-helix from Arg_{659} to Ile_{663} (shown in red). cAMP apolar interactions with the side chains of Arg_{659} and Ile_{663} are represented as dotted spheres. (*E*) Close-up view of the N-terminal helical bundle (αE′–turn–αA). The cAMP-induced movement of the B- and C-helices element forces the N-terminal helical bundle to adopt a new position. (*F*) Red-marked loop between αE′ and αA folds into αF′.

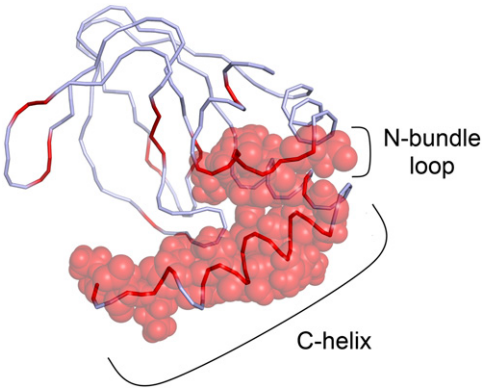

Fig. 3. Proposed binding region for TRIP8b$_{core}$ on the HCN2 CNBD. A ribbon representation of the CNBD shows in red the residues whose amide proton (^{N}H) signals were perturbed upon the addition of TRIP8b$_{core}$. van der Waals volumes are reported for the perturbed residues in the N-bundle loop and in the C-helix. For simplicity, only one conformation of the unstructured region of the C-helix (residues 659–663) is shown. The N- and C-terminal regions of the construct are omitted as in Fig. 1.

TRIP8b Binding Region on the CNBD. Having determined the structure of the CNBD in the cAMP-free form, we next carried out NMR titrations to identify the binding region of TRIP8b on the HCN2 CNBD. We acquired a series of [^{1}H, ^{15}N] heteronuclear single quantum coherence spectra of the ^{15}N-labeled CNBD in the presence of different concentrations of unlabeled TRIP8b$_{core}$. The addition of increasing amounts of TRIP8b$_{core}$ induced a progressive reduction in the intensity of a set of amide proton (^{N}H) signals of the free CNBD and the appearance of a new set of signals of the protein in complex with TRIP8b$_{core}$. At a ratio of [TRIP8b$_{core}$]/[CNBD] of 2.0, a single set of ^{N}H signals was observed (Fig. S3).

A complete list of the residues that experience a different chemical shift upon addition of TRIP8b$_{core}$ is presented in Table S1. The majority of these residues cluster in one region, forming a continuous surface exposed to the solvent (Fig. 3). This region comprises the loop between αE′ and αA of the N-terminal helical bundle (hereafter, the "N-bundle loop") and the C-helix. Interestingly, in the quaternary structure of the cAMP-bound form of the HCN2 channel C-linker/CNBD fragment (Fig. S4), the identified region is not located at the subunit interface but remains fully exposed to the solvent, and thus accessible to the TRIP8b protein both in the cAMP-free and cAMP-bound forms of the CNBD. This finding is consistent with our previous electrophysiological results showing that TRIP8b binding can also occur in the presence of a saturating concentration of cAMP (11).

A few additional residues, experiencing a different chemical shift upon addition of TRIP8$_{core}$, are located in the β-roll and are essentially buried. Finally, three residues in the short stretch that follows the C-helix (Gly$_{664}$, Lys$_{665}$, and Ile$_{669}$) were also perturbed by the addition of TRIP8$_{core}$. Because chemical shift changes at a given residue upon addition of a binding partner do not necessarily indicate a direct contribution of that residue to the binding interaction but can also be the consequence of local structural rearrangements [a behavior observed in a number of other protein–protein complexes characterized by NMR (22–24)], we next sought to obtain direct biochemical evidence implicating the solvent-exposed region identified in Fig. 3 as the prime candidate for mediating the interaction between TRIP8b$_{core}$ and the HCN2 channel CNBD.

Biochemical Validation of TRIP8b Binding Site on the CNBD. To confirm that the N-bundle loop and C-helix regions directly mediate TRIP8b–CNBD interactions, we performed site-directed mutagenesis and biochemical binding assays by affinity-purifying the molecular complex from *E. coli* cells coexpressing the two partner proteins. Deletion of the N-bundle loop (construct CNBD$_{\Delta N}$, comprising residues 550–672) or of the C-helix (construct CNBD$_{\Delta C}$, comprising residues 521–645) completely abolished the formation of the complex between the CNBD and TRIP8b$_{core}$ (Fig. 4). To rule out the possibility that the loss of binding may be due to a global loss of folding of the truncated CNBD constructs, we further confirmed using ITC that the CNBD$_{\Delta N}$ construct retained the same cAMP binding properties of the WT (Table S2). Because the absence of the C-helix prevents cAMP binding (2, 21), the correct global folding of the CNBD$_{\Delta C}$ construct was verified using NMR (Fig. S5). In addition, lack of binding activity to TRIP8b$_{core}$ was further verified for both CNBD truncation constructs using ITC (Table S2). Overall, our results demonstrate that both the N-bundle loop and the C-helix are required for the formation of the TRIP8b binding region. Moreover, our data show that each of these elements is necessary but not sufficient for the binding.

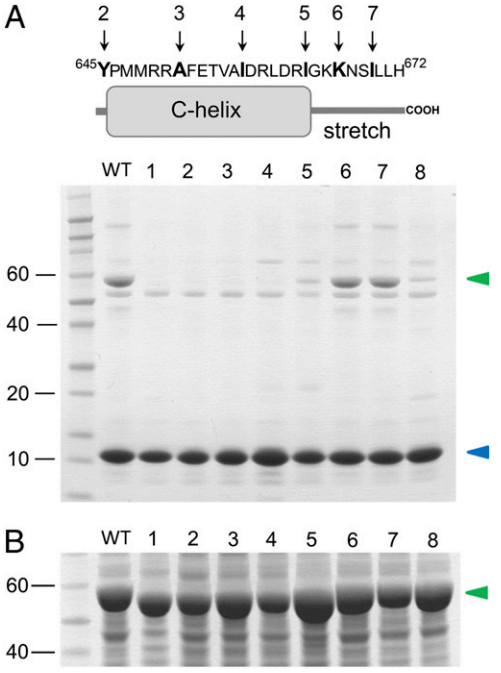

Fig. 4. Contribution of the N-bundle loop and the C-helix/stretch to the TRIP8b binding site. (*A*, *Lower*) Bacterial lysates from cells coexpressing Strep-tagged TRIP8b$_{core}$ (blue arrowhead) and His$_6$-MBP–tagged CNBD WT and mutants (green arrowhead) were loaded onto a Strep-tactin affinity column for Strep-tag purification. Eluted samples were analyzed by Coomassie Blue staining following SDS/PAGE separation. Numbers on the left indicate molecular mass markers (kDa), loaded in the first lane. Lane 1 contains CNBD$_{\Delta N}$. Lane 2 contains CNBD$_{\Delta C}$. Lanes 3–5 contain mutants obtained by progressive truncation of the C-helix. A stop codon was introduced after the following residues: Ala$_{651}$ (lane 3), Ile$_{657}$ (lane 4), and Ile$_{663}$ (lane 5). Pro$_{646}$ and Ile$_{663}$ correspond to the first and last amino acids of the C-helix, respectively. Lanes 6 and 7 contain mutants obtained by progressive truncation of the stretch following the C-helix. A stop codon was introduced after the following residues: Lys$_{666}$ (lane 6) and Ile$_{669}$ (lane 7). Lane 8 contains K$_{665}$E/K$_{666}$E double-CNBD point mutant. (*A*, *Upper*) Sequence and cartoon representation of the C-helix/stretch are shown. Arrows indicate the last residue of the deletion constructs. Numbering of the arrows corresponds to gel lanes. (*B*) Coomassie Blue staining of the bacterial lysates before Strep-tactin affinity purification, showing an equivalent expression level of all the mutant constructs tested. The green arrowhead indicates the His$_6$-MBP–tagged CNBD proteins. Lane numbers are as in *A*.

Because the C-helix is rather long, comprising 18 residues in total, we carried out additional mutagenesis experiments to identify the residues essential for the interaction. To this end, we gradually reintroduced the C-helix in the $CNBD_{\Delta C}$ fragment and tested the resulting constructs for $TRIP8b_{core}$ binding. Somewhat surprisingly, reintroduction of the C-helix (up to residue Ile_{663}) conferred minimal binding activity to $TRIP8b_{core}$, whereas the interaction with $TRIP8b_{core}$ was restored only upon addition of the first three residues of the stretch following the C-helix (GKK, residues 664–666) (Fig. 4). Further addition of downstream residues (667–672) did not improve the binding. We further investigated the role of the two lysines in this stretch (Lys_{665} and Lys_{666}) by mutating them to glutamates. The inversion of charge strongly reduced the binding of the double-mutant CNBD protein $K_{665}E/K_{666}E$ to $TRIP8b_{core}$, confirming the critical role of these two positively charged residues for the interaction (Fig. 4). The proper folding of the double-mutant protein was again assessed using ITC, which confirmed that the $K_{665}E/K_{666}E$ mutant retains cAMP binding activity (Table S2). Of note, the somewhat higher K_d of the double-point mutant compared with WT is likely to reflect the mutation at position 665 because this residue is thought to contribute a direct contact with cAMP in the HCN2 channel CNBD (21).

Discussion

In the present study, we provide direct structural information on the HCN2 channel CNBD conformational transitions due to cAMP binding and identify the specific TRIP8b binding site on the channel's CNBD.

We show here, for the first time to our knowledge, the experimentally determined structure at a high resolution of the human HCN2 channel CNBD in the cAMP-free form, which allows a detailed characterization of all of the conformational transitions that occur in the HCN channel CNBD upon cyclic nucleotide binding. By comparing the cAMP-free and cAMP-bound structures, we show that cAMP binding promotes the following rearrangements in the channel's CNBD: (*i*) folding of the P-helix within the PBC element, located in the β6–β7 loop, which, in turn, causes a repositioning of the hydrophobic residues occupying the β-roll cavity; (*ii*) translational movement of the B- and C-helices toward the β-roll and folding of the distal portion of the C-helix due to its interaction with cAMP; and (*iii*) folding of the F′-helix and upward displacement of the N-terminal helical bundle. The latter displacement likely represents the key movement in the transmission of the cAMP signal from the CNBD to the pore. In HCN channels, the N-terminal helical bundle, which is a conserved element in all CNBDs, comprises the last two helices (αE′ and αF′) of the C-linker, which is directly connected to the pore. Although the precise movements of the HCN channel C-linker, as well as how it affects the pore module, are not completely understood (4, 5, 25), it is clear that the upward movement of the N-terminal helical bundle is crucial in triggering the rearrangement in the C-linker leading to pore opening. In this regard, the HCN2 CNBD behaves in line with the universally conserved mechanism governing CNBDs from several other prokaryotic and eukaryotic proteins (20). Thus, the N-terminal helical bundle is the key element in translating the activation mechanism of several CNBD-containing enzymes, including PKA and EPAC, and the bacterial CNG channel MloK1 (26–28).

We also provide direct structural evidence that the C-terminal part of the C-helix in HCN channels is disordered in the absence of cAMP. Its folding upon addition of cAMP is driven by the formation of a hydrophobic stacking interaction between the side chains of Arg_{659} and Ile_{663} of the C-helix and the adenosine ring of the nucleotide (16, 21). Because these two key residues localize in the disordered region of the C-helix, the capture of the ligand into the CNBD binding pocket in HCN channels requires the stabilization of a dynamic element, a step that may affect the affinity of the protein for cyclic nucleotides. Consistent with this hypothesis, the prokaryotic homolog channel MloK1, which also has a rigid C-helix in the cAMP-free form (28), has about 15-fold lower affinity for cAMP than HCN2 (29).

Our results are consistent with previous data addressing the conformation of the cAMP-free HCN channel CNBD. Although an available structure of the HCN2 CNBD crystallized in the cAMP-free state [Protein Data Bank (PDB) ID code 3FFQ (30)] shows no major differences compared with the cAMP-bound structures, likely due to the presence of bromide ions in the ligand binding pocket, which stabilize the structure in a "cAMP-bound-like" configuration (31), this structure suggests that cAMP-dependent rearrangements might occur in the F′- and C-helices. Moreover, evidence for structural rearrangements in these two elements has been provided by transition metal ion FRET (30, 31).

Very recently, a structural model of the cAMP-free HCN4 CNBD was obtained using CS-Rosetta implemented with the addition of residual dipolar couplings [PDB ID code 2MNG (32)]. The overall structure of the HCN4 model resembles the NMR solution structure of the cAMP-free HCN2 solved in this study, highlighting the high degree of conservation of CNBD folding in HCN channels. Nevertheless, the present experimentally determined 3D structure shows some important differences with respect to the HCN4 CS-Rosetta model: (*i*) the absence of the P-helix in the PBC domain, (*ii*) a lower helical propensity of the F′-helix, and (*iii*) a description of the dynamic of C-helix in the cAMP-free state. Thus, the HCN2 structure presented in this study provides the most comprehensive description to date of the conformational changes that occur upon cAMP binding to the HCN channel CNBD.

Using NMR titration and biochemical assays, we next identify two elements in the HCN2 channel CNBD domain that are both necessary for the interaction with $TRIP8b_{core}$. These elements comprise a number of solvent-exposed residues (Table S1) likely to be involved in the molecular recognition. In particular, the two positively charged residues Lys_{665} and $Lys_{666,}$ located in the stretch following the C-helix, have a critical role in protein complex formation. Intriguingly, $TRIP8b_{core}$ includes an acidic stretch of residues (EEEFE) previously shown to be essential for the functional interaction between TRIP8b and HCN channels (11). Together, these findings suggest that the binding between the C-helix/stretch and TRIP8b might be driven by electrostatic interactions. The relevance of the stretch sequence immediately following the C-helix in the regulation of channel activity is supported by its strong conservation among all four HCN isoforms (33).

Our work demonstrates that TRIP8b and cAMP do not compete for the same binding site and provides definitive structural evidence to validate the allosteric inhibition model recently proposed (11). The binding of $TRIP8b_{core}$ to the HCN2 CNBD affects only a minor set of signals in the NMR spectra, suggesting that no significant conformational changes occur in the overall CNBD structure upon $TRIP8b_{core}$ binding. We conclude that TRIP8b allosterically antagonizes the action of cAMP by stabilizing the cAMP-free conformation of the HCN channel CNBD. Among the several mobile elements that we have identified in the cAMP-free–to–cAMP-bound transition, we find that TRIP8b binding blocks two solvent-exposed elements: the N-bundle loop and the C-helix/stretch. These two elements form a single continuous region, which is easily accessible in both the monomeric and the tetrameric forms of the HCN channel C-linker/CNBD protein fragment. Thus, TRIP8b hinders the cAMP-induced effects on channel activity by two modalities: by blocking the movement of the N-terminal helical bundle, which presumably transmits the movement from the CNBD to the C-linker and the pore, and by preventing the movement of the C-helix, hampering its interaction with cAMP and thus its refolding. As a consequence, when the CNBD is bound to TRIP8b, it has a decreased affinity for cAMP, as recently estimated from electrophysiological data (11).

HCN channels are involved in the regulation of a number of higher order neural processes, including sleep–wake transitions and short- and long-term memory (34–36). Although HCN channels are expressed both in the brain and in the heart, where they contribute to the regulation of cardiac rhythmicity (37, 38), their interaction with the TRIP8b auxiliary subunit is unique to the brain (39). Thus, in providing structural information on the dual cAMP/TRIP8b modulation of HCN channel activity, our work may ultimately lead to a better comprehension of the molecular bases of neurological disorders linked to dysfunction of the I_h conductance in neurons and to the design of drugs specifically able to modulate HCN channel-mediated neural processes.

Materials and Methods

Preparation of Proteins. Samples for NMR studies, as well as protein complexes, were prepared as detailed in *SI Materials and Methods*.

ITC. Measurements were carried out at 25 °C using a MicroCal VP-ITC microcalorimeter (GE Healthcare). A detailed description of the measurements is provided in *SI Materials and Methods*.

NMR Data and Structure Determination. NMR experiments were acquired on a Bruker Avance II+ 800-MHz spectrometer equipped with a quadrupole resonance (QXI-HCN) gradient probe and on a Bruker Avance III 600-MHz NMR spectrometer equipped with a triple (TCI) resonance cryo-probe at 298 K. A detailed description of NMR experiments, data evaluation, and structure calculation is provided in *SI Materials and Methods*.

The NMR titration was performed maintaining the concentration of cAMP-free HCN2 CNBD constant at 0.1 mM. Each of the titration points was prepared independently by adding an aliquot of unlabeled $TRIP8b_{core}$ to a solution of ^{15}N-CNBD until reaching a ratio of [$TRIP8b_{core}$]/[HCN2 CNBD] of 2.0. CNBD in the complex with $TRIP8b_{core}$ exchanges with the free protein at rates slower than the chemical shift differences between the two forms (i.e., in the range of milliseconds).

ACKNOWLEDGMENTS. We thank Xention Ltd. for the generous gift of HCN2 cDNA, Claudia Corso for technical help, and Dr. Andrea Alfieri for helpful discussion. We thank Dr. Sebastiano Pasqualato and Dr. Valentina Cecatiello (Crystallography Unit, European Institute of Oncology) for providing ITC equipment and assistance. NMR data were collected on 600-MHz and 800-MHz NMR spectrometers that are part of the National NMR Network, supported by the Fundação para a Ciência e a Tecnologia (RECI/BBB-BQB/0230/2012), and on a 900-MHz spectrometer at the Magnetic Resonance Center of the University of Florence. This work was partially supported by Programmi di Ricerca di Rilevante Interesse Nazionale Grant 2010CSJX4F and Ministero Affari Esteri Grant 01467532013-06-27 (to A.M.), by the Deutsche Forschungsgemeinschaft with Heisenberg stipend HA3459/5 (to C.H.), by National Institutes for Health Grant NS36658 (to B.S.), by Portuguese National Funds through Fundação para a Ciência e Tecnologia Projects PTDC/BIA-PRO/109796/2009 (to S.R.P.) and PEst-C/EQB/LA0006/2013 (to S.R.P.), and by BIO-NMR (European FP7 e-Infrastructure 2010-1, Contract 261863; www.bio-nmr.net/).

1. Biel M, Wahl-Schott C, Michalakis S, Zong X (2009) Hyperpolarization-activated cation channels: From genes to function. *Physiol Rev* 89(3):847–885.
2. Wainger BJ, DeGennaro M, Santoro B, Siegelbaum SA, Tibbs GR (2001) Molecular mechanism of cAMP modulation of HCN pacemaker channels. *Nature* 411(6839):805–810.
3. Chen S, Wang J, Zhou L, George MS, Siegelbaum SA (2007) Voltage sensor movement and cAMP binding allosterically regulate an inherently voltage-independent closed-open transition in HCN channels. *J Gen Physiol* 129(2):175–188.
4. Craven KB, Zagotta WN (2004) Salt bridges and gating in the COOH-terminal region of HCN2 and CNGA1 channels. *J Gen Physiol* 124(6):663–677.
5. Craven KB, Olivier NB, Zagotta WN (2008) C-terminal movement during gating in cyclic nucleotide-modulated channels. *J Biol Chem* 283(21):14728–14738.
6. Lolicato M, et al. (2014) Cyclic dinucleotides bind the C-linker of HCN4 to control channel cAMP responsiveness. *Nat Chem Biol* 10(6):457–462.
7. Santoro B, et al. (2009) TRIP8b splice variants form a family of auxiliary subunits that regulate gating and trafficking of HCN channels in the brain. *Neuron* 62(6):802–813.
8. Zolles G, et al. (2009) Association with the auxiliary subunit PEX5R/Trip8b controls responsiveness of HCN channels to cAMP and adrenergic stimulation. *Neuron* 62(6):814–825.
9. Lewis AS, et al. (2009) Alternatively spliced isoforms of TRIP8b differentially control h channel trafficking and function. *J Neurosci* 29(19):6250–6265.
10. Santoro B, et al. (2011) TRIP8b regulates HCN1 channel trafficking and gating through two distinct C-terminal interaction sites. *J Neurosci* 31(11):4074–4086.
11. Hu L, et al. (2013) Binding of the auxiliary subunit TRIP8b to HCN channels shifts the mode of action of cAMP. *J Gen Physiol* 142(6):599–612.
12. Bobker DH, Williams JT (1989) Serotonin augments the cationic current Ih in central neurons. *Neuron* 2(6):1535–1540.
13. Gasparini S, DiFrancesco D (1999) Action of serotonin on the hyperpolarization-activated cation current (Ih) in rat CA1 hippocampal neurons. *Eur J Neurosci* 11(9):3093–3100.
14. Heys JG, Hasselmo ME (2012) Neuromodulation of I(h) in layer II medial entorhinal cortex stellate cells: A voltage-clamp study. *J Neurosci* 32(26):9066–9072.
15. Lolicato M, et al. (2011) Tetramerization dynamics of C-terminal domain underlies isoform-specific cAMP gating in hyperpolarization-activated cyclic nucleotide-gated channels. *J Biol Chem* 286(52):44811–44820.
16. Zagotta WN, et al. (2003) Structural basis for modulation and agonist specificity of HCN pacemaker channels. *Nature* 425(6954):200–205.
17. Han Y, et al. (2011) Trafficking and gating of hyperpolarization-activated cyclic nucleotide-gated channels are regulated by interaction with tetratricopeptide repeat-containing Rab8b-interacting protein (TRIP8b) and cyclic AMP at distinct sites. *J Biol Chem* 286(23):20823–20834.
18. Chow SS, Van Petegem F, Accili EA (2012) Energetics of cyclic AMP binding to HCN channel C terminus reveal negative cooperativity. *J Biol Chem* 287(1):600–606.
19. Bankston JR, et al. (2012) Structure and stoichiometry of an accessory subunit TRIP8b interaction with hyperpolarization-activated cyclic nucleotide-gated channels. *Proc Natl Acad Sci USA* 109(20):7899–7904.
20. Rehmann H, Wittinghofer A, Bos JL (2007) Capturing cyclic nucleotides in action: snapshots from crystallographic studies. *Nat Rev Mol Cell Biol* 8(1):63–73.
21. Zhou L, Siegelbaum SA (2007) Gating of HCN channels by cyclic nucleotides: Residue contacts that underlie ligand binding, selectivity, and efficacy. *Structure* 15(6):655–670.
22. Banci L, et al. (2006) The Atx1-Ccc2 complex is a metal-mediated protein-protein interaction. *Nat Chem Biol* 2(7):367–368.
23. Füzéry AK, et al. (2008) Solution structure of the iron-sulfur cluster cochaperone HscB and its binding surface for the iron-sulfur assembly scaffold protein IscU. *Biochemistry* 47(36):9394–9404.
24. Williamson MP (2013) Using chemical shift perturbation to characterise ligand binding. *Prog Nucl Magn Reson Spectrosc* 73:1–16.
25. Decher N, Chen J, Sanguinetti MC (2004) Voltage-dependent gating of hyperpolarization-activated, cyclic nucleotide-gated pacemaker channels: Molecular coupling between the S4-S5 and C-linkers. *J Biol Chem* 279(14):13859–13865.
26. Kim C, Xuong NH, Taylor SS (2005) Crystal structure of a complex between the catalytic and regulatory (RIalpha) subunits of PKA. *Science* 307(5710):690–696.
27. Rehmann H, Das J, Knipscheer P, Wittinghofer A, Bos JL (2006) Structure of the cyclic-AMP-responsive exchange factor Epac2 in its auto-inhibited state. *Nature* 439(7076):625–628.
28. Schünke S, Stoldt M, Lecher J, Kaupp UB, Willbold D (2011) Structural insights into conformational changes of a cyclic nucleotide-binding domain in solution from Mesorhizobium loti K1 channel. *Proc Natl Acad Sci USA* 108(15):6121–6126.
29. Cukkemane A, et al. (2007) Subunits act independently in a cyclic nucleotide-activated K(+) channel. *EMBO Rep* 8(8):749–755.
30. Taraska JW, Puljung MC, Olivier NB, Flynn GE, Zagotta WN (2009) Mapping the structure and conformational movements of proteins with transition metal ion FRET. *Nat Methods* 6(7):532–537.
31. Puljung MC, Zagotta WN (2013) A secondary structural transition in the C-helix promotes gating of cyclic nucleotide-regulated ion channels. *J Biol Chem* 288(18):12944–12956.
32. Akimoto M, et al. (2014) A Mechanism for the Auto-Inhibition of Hyperpolarization-Activated Cyclic Nucleotide-Gated (HCN) Channel Opening and its Relief by cAMP. *J Biol Chem* 289(32):22205–22220.
33. Santoro B, Tibbs GR (1999) The HCN gene family: Molecular basis of the hyperpolarization-activated pacemaker channels. *Ann N Y Acad Sci* 868:741–764.
34. Bal T, McCormick DA (1996) What stops synchronized thalamocortical oscillations? *Neuron* 17(2):297–308.
35. Nolan MF, et al. (2004) A behavioral role for dendritic integration: HCN1 channels constrain spatial memory and plasticity at inputs to distal dendrites of CA1 pyramidal neurons. *Cell* 119(5):719–732.
36. Thuault SJ, et al. (2013) Prefrontal cortex HCN1 channels enable intrinsic persistent neural firing and executive memory function. *J Neurosci* 33(34):13583–13599.
37. Barbuti A, DiFrancesco D (2008) Control of cardiac rate by "funny" channels in health and disease. *Ann N Y Acad Sci* 1123:213–223.
38. Wahl-Schott C, Fenske S, Biel M (2014) HCN channels: New roles in sinoatrial node function. *Curr Opin Pharmacol* 15:83–90.
39. Santoro B, Wainger BJ, Siegelbaum SA (2004) Regulation of HCN channel surface expression by a novel C-terminal protein-protein interaction. *J Neurosci* 24(47):10750–10762.

Supporting Information

Saponaro et al. 10.1073/pnas.1410389111

SI Materials and Methods

Preparation of Proteins for NMR Experiments. The cDNA fragment encoding residues 521–672 of human hyperpolarization-activated cyclic nucleotide-gated 2 (HCN2) [HCN2 cyclic nucleotide binding domain (CNBD)] was cloned into a modified pET-24b downstream of a double His_6-maltose binding protein (MBP) tag and transformed into *Escherichia coli* Rosetta strain (EMD Millipore) under kanamycin and chloramphenicol selection. Cells were grown at 37 °C in LB to an OD_{600} of 0.6 and induced with 0.4 mM isopropyl-1-thio-β-D-galactopyranoside overnight at 20 °C. To uniformly label the HCN2 CNBD with ^{15}N or $^{15}N/^{13}C$, cells were grown in M9 minimal medium containing 1.0 g/L $^{15}NH_4Cl$ (Cambridge Isotope Laboratories, Inc.), 3% (wt/vol) glucose or ^{13}C-U (Cambridge Isotope Laboratories, Inc.), 1 mM $MgSO_4$, 0.01 mg/mL thiamine-HCl, 18.5 μM $FeCl_3$ $6H_2O$, and 0.1 mM $CaCl_2$ $2H_2O$. Cells were collected by centrifugation and resuspended in ice-cold lysis buffer [500 mM KCl, 30 mM Hepes (pH 7.4), 10% (wt/vol) glycerol] with the addition of 1 mM β-mercaptoethanol, 10 μg/mL DNase, 0.25 mg/mL lysozyme, 100 μM phenylmethylsulfonyl fluoride, 5 μM leupeptin, and 1 μM pepstatin. Cells were sonicated on ice 12 times for 20 s each time, and the lysate was cleared by centrifugation. The proteins were purified by affinity chromatography on Ni^{2+}-nitrilotriacetic acid resin and eluted in lysis buffer plus 300 mM imidazole. The His_6-MBP was removed by Human Rhinovirus 3C rotease cleavage overnight at 4 °C. The cleavage reaction was loaded onto an amylose resin (New England Biolabs), and the flow-through was collected and loaded onto a HiLoad 16/60 Superdex 75 prep grade size exclusion column (GE Healthcare) equilibrated with 150 mM KCl and 20 mM potassium phosphate (pH 6.0). After the size exclusion chromatography, the fractions containing the HCN2 CNBD were combined and buffer was exchanged using a PD10 (GE Healthcare) column to buffer A [5 mM KCl and 20 mM potassium phosphate (pH 6.0)]. A Mono S G 5/5 (GE Healthcare) cation-exchange chromatography column was used to remove remaining protein contaminants. Buffer A was used as binding buffer, and elution was directed with buffer B [500 mM KCl and 20 mM potassium phosphate (pH 6.0)]. Dynamic light scattering analysis confirmed that the protein is monomeric (1, 2).

The cDNA fragment encoding residues 188–268 ($TRIP8b_{core}$) of mouse TRIP8b (splice variant 1a) was cloned into pET-52b (EMD Millipore) downstream of a Streptactin-binding (Strep) (II) tag sequence. The plasmid was transformed into an *E. coli* BL21 Rosetta strain under ampicillin and chloramphenicol selection. Cells were grown at 37 °C in LB to an OD_{600} of 0.6 and induced with 0.4 mM isopropyl-1-thio-β-D-galactopyranoside. After 3 h, cells were collected by centrifugation and resuspended in ice-cold lysis buffer [150 mM NaCl, 100 mM Tris·Cl (pH 8), and 1 mM EDTA] with the addition of 1 mM β-mercaptoethanol, 10 μg/mL DNase, 0.25 mg/mL lysozyme, 100 μM phenylmethylsulfonyl fluoride, 5 μM leupeptin, and 1 μM pepstatin. The cells were sonicated on ice 12 times for 20 s each time, and the lysate was cleared by centrifugation. Protein was purified by affinity chromatography using StrepTrap HP columns (GE Healthcare) and eluted in 150 mM KCl, 30 mM Hepes (pH 7.4), 10% (wt/vol) glycerol, and 2.5 mM desthiobiotin. The eluted protein was then loaded into a HiLoad 16/60 Superdex 75 prep grade size exclusion column (GE Healthcare), which was equilibrated with 150 mM KCl, 30 mM Hepes (pH 7.4), and 10% (wt/vol) glycerol.

All purification steps were performed at 4 °C and monitored using the AKTApurifier UPC 10 fast protein liquid chromatography system (GE Healthcare). The protein purity was confirmed by SDS/PAGE. For NMR experiments, the protein samples were buffer-exchanged with a PD10 column to 150 mM KCl and 20 mM potassium phosphate (pH 7.0). All NMR samples in the concentration range between 0.2 and 1 mM contained 10% (vol/vol) of $2H_2O$ (Sigma).

Purification of Protein Complexes. The modified pET-24b containing $HCN2_{470–672}$ (C-linker + CNBD) was cotransformed with vector pET-52b containing $TRIP8b_{core}$ (described above) into *E. coli* Rosetta strain under kanamycin and ampicillin selection. Cells were grown at 37 °C in LB to an OD_{600} of 0.6 and induced with 0.4 mM isopropyl-1-thio-β-D-galactopyranoside; after 3 h, cells were collected by centrifugation. Copurification was performed using the protocol described for the purification of the HCN2 CNBD, with the addition in the elution buffer of different concentrations of cAMP ranging from 0 to 1 mM.

The cDNA fragments encoding, $HCN2_{550–672}$ ($CNBD_{ΔN}$), $HCN2_{521–645}$ ($CNBD_{ΔC}$), $HCN2_{521–651}$, $HCN2_{521–657}$, $HCN2_{521–663}$, $HCN2_{521–666}$, and $HCN2_{521–669}$ were cloned into the same modified pET-24b described above. The double mutation $K_{665}E/K_{666}E$ was introduced on the HCN2 CNBD using the QuikChange mutagenesis kit (Stratagene). Each of these plasmids (including the HCN2 CNBD described above) was cotransformed with pET-52b containing $TRIP8b_{core}$ into *E. coli* Rosetta strain under kanamycin and ampicillin selection. Cells were grown at 37 °C in LB to an OD_{600} of 0.8 and induced with 0.1 mM isopropyl-1-thio-β-D-galactopyranoside for 3 h. Copurification was performed using the protocol described for the purification of $TRIP8b_{core}$. Each purification experiment was repeated at least three times.

Samples were analyzed by SDS/PAGE using Precise Tris-Hepes (Thermo Scientific) 8–16% gel (Fig. S1*A*) and NuPAGE (Novex) Bis-Tris 4–12% gel (Fig. 4 and Fig. S1*B*) in MES buffer (Invitrogen).

Isothermal Titration Calorimetry. Measurements were carried out at 25 °C using an MicroCal VP-ITC microcalorimeter (GE Healthcare). The volume of the sample cell was 1.4 mL; the reference cell contained water. The proteins were extensively dialyzed against PBS. The HCN2 CNBD (20 μM) was titrated with $TRIP8b_{core}$ (200 μM) using injection volumes of 10 μL. In the case of measurements of cAMP binding, the HCN2 CNBD WT, ΔN, and $K_{665}E/K_{666}E$ mutant proteins (15 μM) were titrated with cAMP (200 μM) using injection volumes of 4 μL. Calorimetric data were analyzed with MicroCal Origin software (version 7), and equations were described for the single-site binding model (3).

NMR Data and Structure Determination. The NMR experiments used for the assignment of backbone and aliphatic side-chain resonances and for collecting the distance restraints for structure calculation are summarized in Table S3. Resonance assignment for the cAMP-free HCN2 CNBD has been deposited in the BioMagResBank (BMRB ID code 19977). All spectra of the HCN2 CNBD in the cAMP-free form show a single set of resonance signals, indicating that the protein adopts a single conformation. The resonance assignment of the cAMP-free HCN2 CNBD formed the basis for automated peak-picking and automated NOE assignment of the 3D NOESY experiments using UNIO-ATNOS/CANDID (4, 5), combined with structure calculation using the Combined Assignment and Dynamics Algorithm for NMR Applications (CYANA), version 2.1 (6). A total of 105 ϕ- and 105 ψ-dihedral angle constraints were derived from ^{15}N, $^{13}C'$, $^{13}C_α$, $^{13}C_β$, and $H_α$ chemical shifts, using TALOS+ (7). After manual

NOE assignment refinement, the 20 conformers with the lowest residual target function values were subjected to restrained energy minimization with AMBER 12.0 (8) implemented in the web portal AMBER-Based Portal Server for NMA Structures (AMPS-NMR) (9) (www.wenmr.eu). The final bundle of 20 conformers of the cAMP-free HCN2 CNBD has an average total target function of 0.90 ± 0.22 Å (CYANA units). The average backbone and heavy atom rmsd values (to the mean structure) are 0.94 ± 0.23 Å and 1.37 ± 0.18 Å, respectively. The first 22 residues at the N-terminal region and the last 18 residues at the C-terminal region have been not included in the rmsd calculation because they are highly disordered and lack long-range NOEs. The quality of the family of conformers was evaluated using the Protein Structure Validation Suite (PSVS) (10) and WHAT IF (11) validation programs. Table S4 reports some statistics on constraint violations, together with selected quality parameters. The atomic coordinates have been deposited in the Protein Data Bank (PDB ID code 2MPF; www.rcsb.org).

The ^{15}N heteronuclear NOE experiments were collected as described in Table S3, and the values were calculated as the ratio of peak volumes in spectra recorded with and without ^{1}H saturation.

1. Lolicato M, et al. (2011) Tetramerization dynamics of C-terminal domain underlies isoform-specific cAMP gating in hyperpolarization-activated cyclic nucleotide-gated channels. *J Biol Chem* 286(52):44811–44820.
2. Chow SS, Van Petegem F, Accili EA (2012) Energetics of cyclic AMP binding to HCN channel C terminus reveal negative cooperativity. *J Biol Chem* 287(1):600–606.
3. Wiseman T, Williston S, Brandts JF, Lin LN (1989) Rapid measurement of binding constants and heats of binding using a new titration calorimeter. *Anal Biochem* 179(1): 131–137.
4. Herrmann T, Güntert P, Wüthrich K (2002) Protein NMR structure determination with automated NOE assignment using the new software CANDID and the torsion angle dynamics algorithm DYANA. *J Mol Biol* 319(1):209–227.
5. Herrmann T, Güntert P, Wüthrich K (2002) Protein NMR structure determination with automated NOE-identification in the NOESY spectra using the new software ATNOS. *J Biomol NMR* 24(3):171–189.
6. Güntert P, Mumenthaler C, Wüthrich K (1997) Torsion angle dynamics for NMR structure calculation with the new program DYANA. *J Mol Biol* 273(1):283–298.
7. Cornilescu G, Delaglio F, Bax A (1999) Protein backbone angle restraints from searching a database for chemical shift and sequence homology. *J Biomol NMR* 13(3):289–302.
8. Case DA, et al. (2012) AMBER 12 (University of California, San Francisco).
9. Bertini I, Case DA, Ferella L, Giachetti A, Rosato A (2011) A Grid-enabled web portal for NMR structure refinement with AMBER. *Bioinformatics* 27(17):2384–2390.
10. Bhattacharya A, Tejero R, Montelione GT (2007) Evaluating protein structures determined by structural genomics consortia. *Proteins* 66(4):778–795.
11. Vriend G (1990) WHAT IF: A molecular modeling and drug design program. *J Mol Graph* 8(1):52–56.

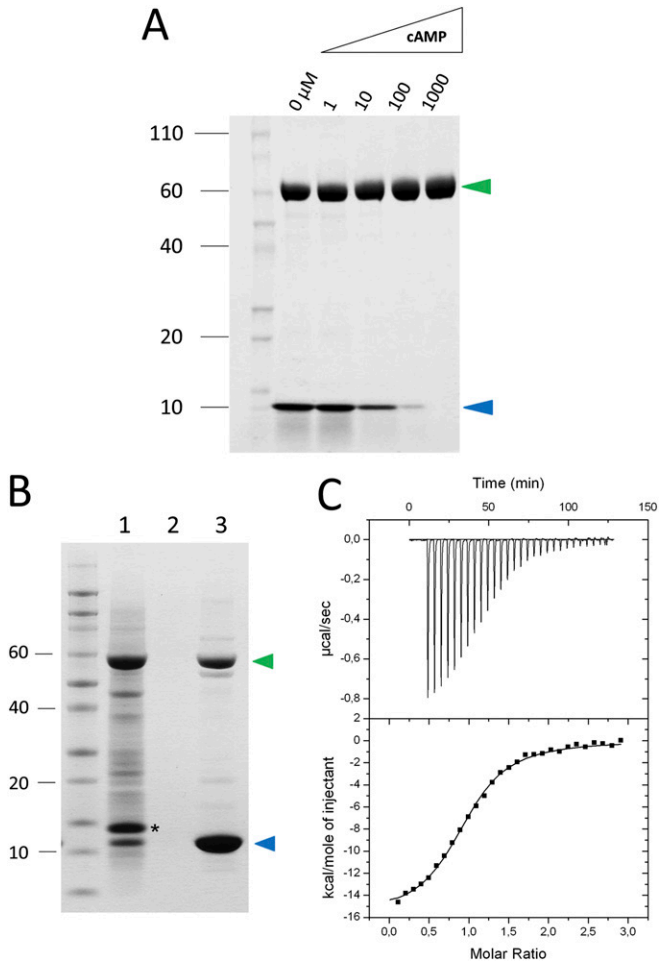

Fig. S1. Analysis of the interaction between the HCN2 channel CNBD and TRIP8b$_{core}$. (*A*) cAMP disrupts the TRIP8b$_{core}$–CNBD$_{c\text{-}linker}$ complex formation. Coomassie Blue staining was performed following SDS/PAGE separation of the complex eluted from a nickel affinity column, after preincubation with increasing cAMP concentrations (indicated above the gel picture). The green arrowhead marks the position of the His$_6$-MBP–tagged CNBD$_{c\text{-}linker}$, whereas the blue arrowhead marks the position of Strep-tagged TRIP8b$_{core}$. Numbers to the left refer to molecular mass markers (kDa), which are loaded in the first lane. (*B*) Coomassie Blue staining following SDS/PAGE separation of the complex purified on a Strep-tactin affinity column by means of the Strep tag attached to TRIP8b$_{core}$. Lanes: lysate (1), last wash (2), and eluate (3). The green arrowhead marks the position of the His$_6$-MBP–tagged CNBD, and the blue arrowhead marks Strep-tagged TRIP8b$_{core}$. The asterisk in lane 1 indicates lysozyme (*SI Materials and Methods*). Numbers indicate molecular mass markers (kDa) loaded in the first lane. (*C*) Isothermal titration calorimetry of TRIP8b$_{core}$ binding to the CNBD. (*Upper*) Heat changes during successive injections of 10 μL of TRIP8b$_{core}$ (200 μM) into the CNBD protein (20 μM). (*Lower*) Binding curve obtained from data (*Upper*). The peaks were integrated, normalized to the TRIP8b$_{core}$ concentration, and plotted against the molar ratio of TRIP8b$_{core}$ to the CNBD. The solid line represents a nonlinear least-squares fit to a single-site binding model (*SI Materials and Methods*), which yields a K_d of 1.30 ± 0.06 μM (SEM) and a stoichiometric N value of 0.98 ± 0.01 (SEM) (n = 3).

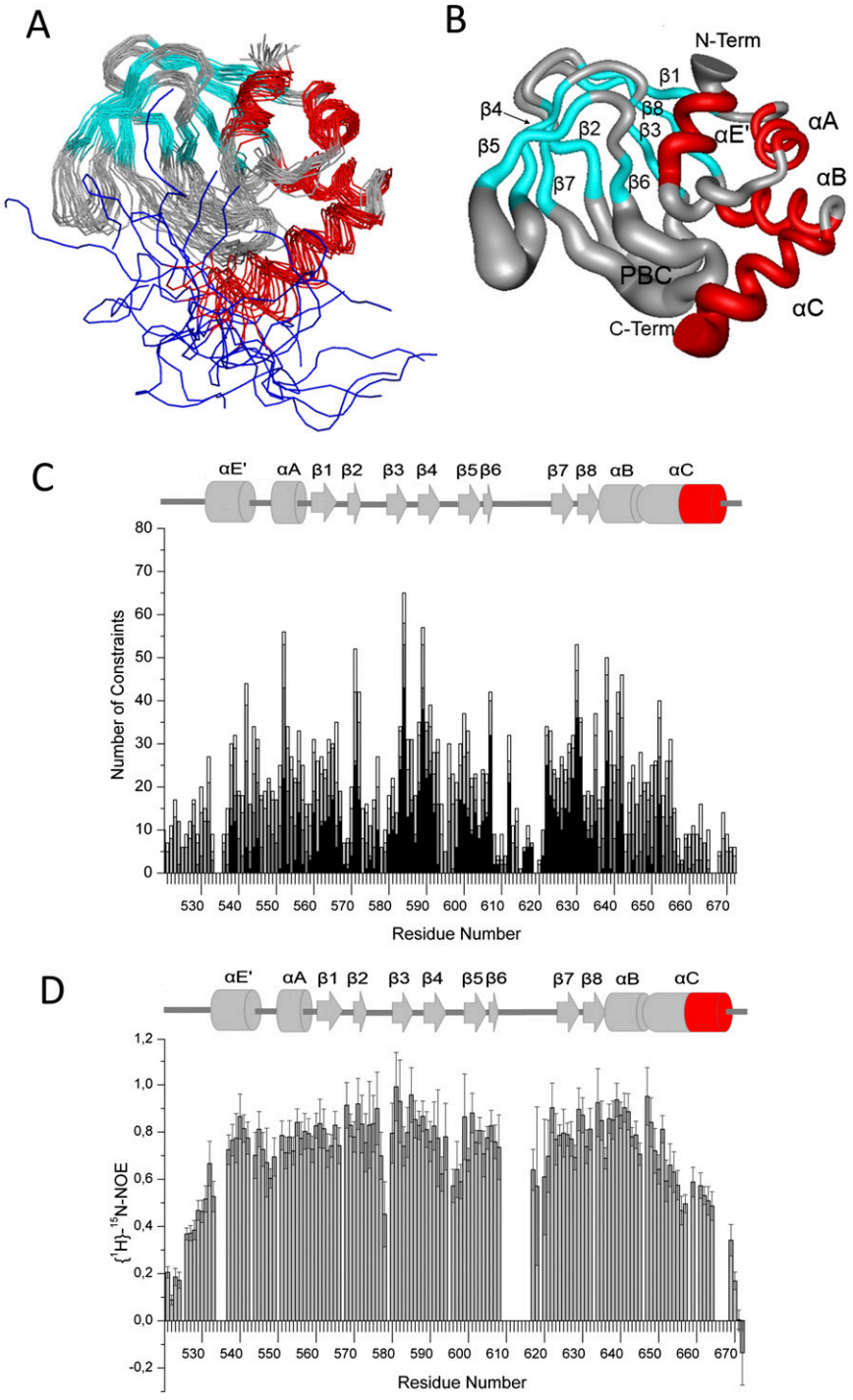

Fig. S2. NMR solution structure of the cAMP-free CNBD of human HCN2. (*A*) Overlay of the backbone traces for the 20 lowest energy conformers of the cAMP-free CNBD. The α-helices are colored in red, the β-strands are colored in cyan, and the C-terminal unstructured region comprising the C-terminal part of the C-helix and the following stretch (residues 659–672) is shown in blue. The unfolded region at the N terminus of the construct (residues 521–532) is omitted. (*B*) Radius of the tubes is proportional to the backbone rmsd of each residue. The C-terminal unstructured region was omitted for clarity. Secondary structure elements are labeled and color-coded as in *A*. (*C*, *Lower*) Number of meaningful NOEs per residue of the cAMP-free HCN2 CNBD. White, light gray, dark gray, and black bars indicate intraresidue, sequential, medium-range, and long-range connectivity, respectively. (C, *Upper*) Secondary structure elements are shown: Arrows indicate β-strands, and cylinders indicate α-helices. The unstructured C-terminal region of the C-helix (residues 659–663) is highlighted in red. (*D*, *Lower*) Two-dimensional ^{15}N heteronuclear NOE experiment performed on the cAMP-free HCN2 CNBD. {^{1}H}-^{15}N–NOE values of amide resonances at 298 K and 800 MHz, plotted against residue number. (*D*, *Upper*) Secondary structure elements are shown. Arrows indicate β-strands, and cylinders indicate α-helices. The unstructured C-terminal region of the C-helix (residues 659–663) is highlighted in red.

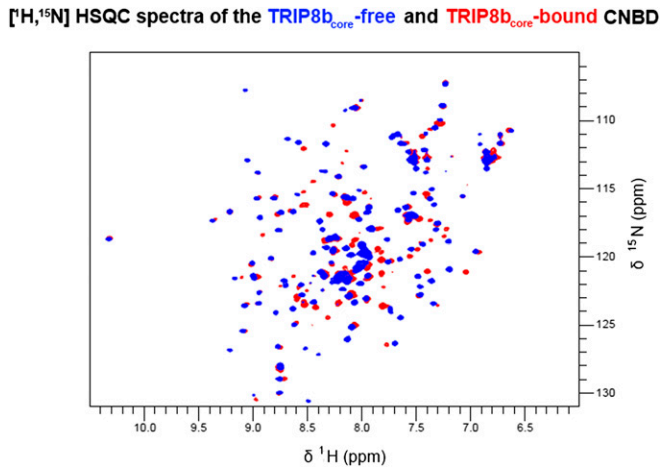

Fig. S3. Chemical shift perturbation of the cAMP-free HCN2 CNBD amide proton (^{N}H) signals due to TRIP8b$_{core}$ interaction. Superimposition of the [^{1}H, ^{15}N] heteronuclear single quantum coherence (HSQC) of TRIP8b$_{core}$-free CNBD (blue) and TRIP8b$_{core}$-bound CNBD (red) is shown ([TRIP8b$_{core}$]/[CNBD] = 2).

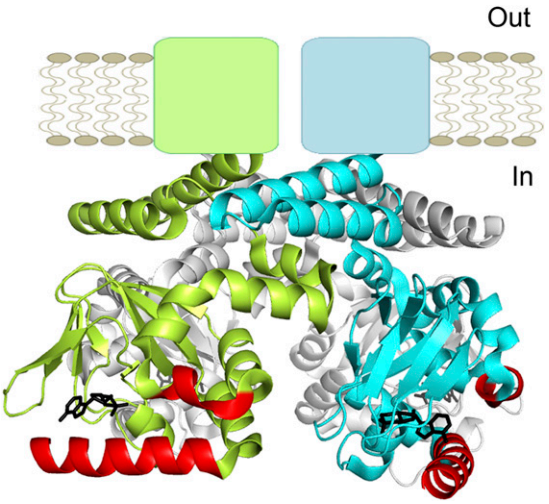

Fig. S4. Proposed binding region for TRIP8b$_{core}$ on the HCN2 CNBD. The quaternary structure of the C-linker + CNBD of HCN2 [cAMP-bound form, PDB ID code 1Q5O (1)] is shown. The N-bundle loop and C-helix are highlighted in red on two of the four subunits, transmembrane regions are represented by rectangles, and cAMP molecules are shown as black sticks.

1. Zagotta WN, et al. (2003) Structural basis for modulation and agonist specificity of HCN pacemaker channels. *Nature* 425(6954):200–205.

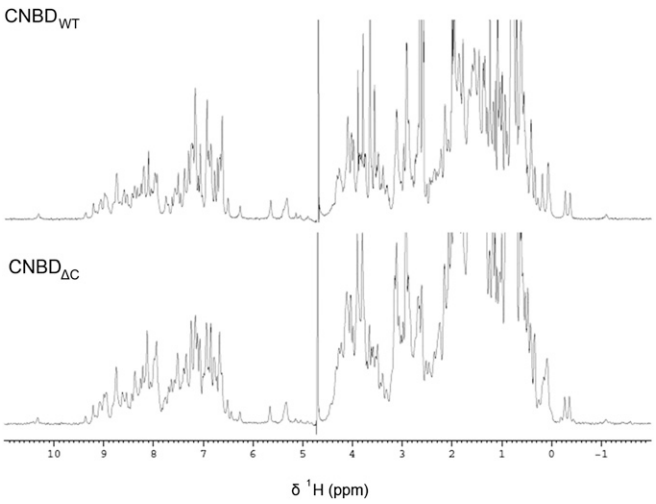

Fig. S5. CNBD$_{\Delta C}$ mutant retains the overall folding of the CNBD. A structural comparison of the CNBD WT (CNBD$_{WT}$) and the mutant lacking the C-helix/stretch (ΔC; CNBD$_{\Delta C}$) is shown. A comparison of the ^{1}H-monodimensional spectrum of the CNBD$_{WT}$ (*Upper*) and CNBD$_{\Delta C}$ (*Lower*) shows that the mutant retains the same folding as the WT.

Table S1. Amino acids of cAMP-free HCN2 CNBD whose amide proton (^{N}H) signals experience chemical shift changes upon the addition of TRIP8b$_{core}$

Exposure*	Residue
Buried	Val_{539}, Phe_{545}, Glu_{574}, Lys_{580}, Met_{581}, Thr_{593}, Tyr_{606}, Phe_{607}, Gly_{608}, Leu_{642}, Met_{648}, Phe_{652}
Exposed	Leu_{544}, Ala_{546}, Asn_{547}, Ala_{548}, Asp_{549}, Gly_{575}, Lys_{594}, Glu_{598}, Met_{599}, Arg_{617}, Met_{647}, Arg_{649}, Arg_{650}, Ala_{651}, Glu_{653}, Thr_{654}, Val_{655}, Ala_{656}, Arg_{659}, leu_{660}, Asp_{661}, Ile_{663}, Gly_{664}, Lys_{665}, Ile_{669}

*Based on solvent accessibility as calculated with the program Naccess V2.1.1 - Atomic Solvent Accessible Area Calculations (1).

1. Hubbard SJ, Hornton JM (1993) NACCESS, Computer Program (Department of Biochemistry and Molecular Biology, University College London).

Table S2. cAMP and TRIP8b$_{core}$ binding to HCN2 CNBD mutants

Titrant	CNBD	N ± SEM	K_d, μM ± SEM	*n*
cAMP	WT	1.06 ± 0.03	1.70 ± 0.10	3
	ΔN	0.90 ± 0.01	0.77 ± 0.11	3
	$K_{665}E/K_{666}E$	1.22 ± 0.03	6.10 ± 0.65	3
TRIP8b$_{core}$	WT	1.17 ± 0.01	1.50 ± 0.09	1
	ΔN	No binding detected		1
	ΔC	No binding detected		1

Isothermal titration calorimetry measurements of cAMP and TRIP8b$_{core}$ binding to the purified CNBD proteins fused to the MBP. ΔC, residues 521–645; ΔN, residues 550–672.

Table S3. Acquisition parameters for NMR experiments performed on cAMP-free form of the HCN2 CNBD

	Dimension of acquired data (nucleus)			Spectral width, ppm				
Experiments*	t1	t2	t3	F1	F2	F3	$n^{\dagger}$	Refs.
[^{1}H-^{1}H]-NOESY‡	1,024(^{1}H)	2,048(^{1}H)		16	16		80	(1)
[^{1}H-^{1}H]-TOCSY‡	896(^{1}H)	1,024(^{1}H)		16	16		64	(1, 2)
^{1}H-^{15}N-HSQC	256 (^{15}N)	2,048 (^{1}H)		28	14		4	(3, 4)
^{1}H-^{13}C-HSQC§	256(^{13}C)	1,024(^{1}H)		166	16		4	(5–7)
HNCACB§	128 (^{13}C)	48 (^{15}N)	2,048 (^{1}H)	75	28	16	16	(8)
CBCACONH§	80 (^{13}C)	48 (^{15}N)	2,048 (^{1}H)	75	28	14	32	(8, 9)
HNCO§	80 (^{13}C)	40 (^{15}N)	2,048 (^{1}H)	16	28	14	32	(10)
HNCACO§	80 (^{13}C)	40 (^{15}N)	2,048 (^{1}H)	16	28	16		(11)
HNHA	128 (1H)	40 (15N)	2,048 (1H)	16	30	16	16	(12)
(H)CCH-TOCSY§	128 (^{13}C)	64 (^{13}C)	2,048 (^{1}H)	75	75	14	16	(13)
^{15}N-edited [^{1}H-^{1}H]-NOESY¶	232 (^{1}H)	38 (^{15}N)	2,048 (^{1}H)	13	28	14	24	(7)
^{13}C-edited [^{1}H-^{1}H]-NOESY¶	200 (^{1}H)	48 (^{13}C)	2,048 (^{1}H)	14	76	14	16	(14)
2D (HB)CB(CGCD)HD and (HB)CB(CGCD)HE§	80 (^{13}C)	2,048 (^{1}H)		16	40		296	(15)
^{1}H-^{15}N NOE$^{\|}$	208 (^{15}N)	2,048 (^{1}H)		28	16		28	(4, 16)

F, three-dimensional frequency domain; HSQC, heteronuclear single quantum coherence; t, three-dimensional time domain.

*All of the experiments were acquired on a Bruker Avance II+ 800-MHz spectrometer equipped with an quadrupole resonance (QXI-HCN) gradient probe and on a Bruker Avance III 600-MHz NMR spectrometer equipped with a triple (TCI) resonance cryo-probe at 298 K.

†Number of acquired scans.

‡Experiment was conducted with a Bruker Avance 900-MHz spectrometer.

§Experiments were performed on ^{15}N-^{13}C samples.

¶Mixing times used were 120 ms for 3D ^{13}C-edited NOESY and 3D ^{15}N-edited NOESY experiments.

$^{\|}$Interscan delay (d_1) was 5 s with and without saturation of the amide protons, which was achieved using 120° high-power pulses. All 3D and 2D spectra were processed using the standard Bruker software TOPSPIN 2.1 and analyzed through the Computer Aided Resonance Assignment (CARA; cara.nmr.ch) and XEASY programs (17, 18).

1. Hwang TL, Shaka AJ (1995) Water suppression that works—Excitation sculpting using arbitrary wave-forms and pulsed-field gradients. *J Magn Reson A* 112(2):275–279.
2. Bax A, Davis DG (1985) Mlev-17-based two-dimensional homonuclear magnetization transfer spectroscopy. *J Magn Reson* 65(2):355–360.
3. Davis AL, Keeler J, Laue ED, Moskau D (1992) Experiments for recording pure-absorption heteronuclear correlation spectra using pulsed field gradients. *J Magn Reson* 98(1):207–216.
4. Grzesiek S, Bax A (1993) The Importance of Not Saturating H2o in Protein Nmr - Application to Sensitivity Enhancement and Noe Measurements. *J Am Chem Soc* 115(26):12593–12594.
5. Palmer AG, Cavanagh J, Wright PE, Rance M (1991) Sensitivity improvement in proton-detected 2-dimensional heteronuclear correlation NMR-spectroscopy. *J Magn Reson* 93(1): 151–170.
6. Kay LE, Keifer P, Saarinen T (1992) Pure absorption gradient enhanced heteronuclear single quantum correlation spectroscopy with improved sensitivity. *J Am Chem Soc* 114(26): 10663–10665.
7. Schleucher J, et al. (1994) A general enhancement scheme in heteronuclear multidimensional NMR employing pulsed field gradients. *J Biomol NMR* 4(2):301–306.
8. Muhandiram DR, Kay LE (1994) Gradient-enhanced triple-resonance 3-dimensional NMR experiments with improved sensitivity. *J Magn Reson B* 103(3):203–216.
9. Lescop E, Schanda P, Brutscher B (2007) A set of BEST triple-resonance experiments for time-optimized protein resonance assignment. *J Magn Reson* 187(1):163–169.
10. Schleucher J, Sattler M, Griesinger C (1993) Coherence selection by gradients without signal attenuation—Application to the 3-dimensional HNCO experiment. *Angew Chem Int Ed Engl* 32(10):1489–1491.
11. Salzmann M, Wider G, Pervushin K, Senn H, Wuthrich K (1999) TROSY-type triple-resonance experiments for sequential NMR assignments of large proteins. *J Am Chem Soc* 121(4): 844–848.
12. Vuister GW, Bax A (1993) Quantitative J Correlation—A new approach for measuring homonuclear 3-bond J(H(N)H(Alpha) coupling-constants in N-15-enriched proteins. *J Am Chem Soc* 115(17):7772–7777.
13. Kay LE, Xu GY, Singer AU, Muhandiram DR, Formankay JD (1993) A gradient-enhanced HCCH TOCSY experiment for recording side-chain H-1 and C-13 correlations in H_20 samples of proteins. *J Magn Reson B* 101(3):333–337.
14. Zhang O, Kay LE, Olivier JP, Forman-Kay JD (1994) Backbone 1H and 15N resonance assignments of the N-terminal SH3 domain of drk in folded and unfolded states using enhanced-sensitivity pulsed field gradient NMR techniques. *J Biomol NMR* 4(6):845–858.
15. Yamazaki T, Formankay JD, Kay LE (1993) 2-Dimensional NMR experiments for correlating C-13-Beta and H-1-Delta/Epsilon chemical-shifts of aromatic residues in C-13-labeled proteins via scalar couplings. *J Am Chem Soc* 115(23):11054–11055.
16. Farrow NA, et al. (1994) Backbone dynamics of a free and phosphopeptide-complexed Src homology 2 domain studied by 15N NMR relaxation. *Biochemistry* 33(19):5984–6003.
17. Keller R (2004) *The Computer Aided Resonance Assignment Tutorial* (CANTINA Verlag, Goldau, Switzerland).
18. Bartels C, Xia TH, Billeter M, Güntert P, Wüthrich K (1995) The program XEASY for computer-supported NMR spectral analysis of biological macromolecules. *J Biomol NMR* 6(1):1–10.

Table S4. Statistical analysis of the energy minimized family of conformers of cAMP-free HCN2 CNBD

Quality parameters	20 conformers	
Total no. of meaningful NOE upper distance constraints	1,877	
Intraresidue	508	
Sequential (|i − j| = 1)	577	
Medium-range (|i − j| < 4)	295	
Long-range (|i − j > 5)	461	
Total meaningful dihedral angle restraints		
ϕ	103	
ψ	103	
Hydrogen bond constraint	36	
No. of long-range constraints per residue*	4.20	
Residual constraint violations		
Average no. of distance violations per conformers		
0.1–0.2 Å	12.5	
0.2–0.3 Å	0.5	
0.3–0.4 Å	0.15	
Larger than 0.4 Å	0	
Average no. of dihedral angle violations per conformers		
5–10°	3.30	
10–15°	0.03	
Larger than 15°	0	
Average rmsd to the mean, Å		
Backbone atoms	0.94 ± 0.23	
All heavy atoms	1.37 ± 0.18	
Residual CYANA target function (CYANA units)	0.90 ± 0.22	
Structural analysis,† %		
Residues in most favorable regions	91.4(95.3)	
Residues in allowed regions	8.1(4.7)	
Residues in generously allowed regions	0.5(0.0)	
Residues in disallowed regions	0.0(0.0)	
WHAT IF structure Z-scores‡		
First-generation packing quality	−0.167 ± 0.759	
Second-generation packing quality	6.514 ± 2.170	
Ramachandran plot appearance	−2.866 ± 0.421	
χ_1/χ_2 rotamer normality	−5.800 ± 0.404	
Backbone conformation	−1.539 ± 0.406	
WHAT IF rms Z-scores		
Bond lengths	1.195 ± 0.004	
Bond angles	0.814 ± 0.023	
Omega angle restraints	1.950 ± 0.191	
Side-chain planarity	1.197 ± 0.120	
Improper dihedral distribution	1.185 ± 0.054	
Inside/outside distribution	0.949 ± 0.024	
Global quality scores (raw/Z-scores)§		
Verify3D	0.36	−1.61
Procheck (ϕ − ψ)	−0.43 (−0.27)	−1.38 (−0.75)
Procheck (all)2	−0.60 (−0.53)	−3.55 (−3.13)
MolProbity Clash score	4.04	0.83

Structure calculations were performed with the program CYANA 2.1 (1). A total of 500 random conformers were subjected to 10,000 steps of a simulated annealing process. Each member of the family was subjected to refinement with the AMBER 12.0 package (2). Values of 50 kcal·mol^{-1}·Å^{-2} and 32 kcal·mol^{-1}·rad^{-2} were used as force constants for the NOE and torsion angle restraints, respectively. The data are calculated over the 20 conformers of the family. The mean value and the SD are given.

*Average calculated over residues 536–654.

†Resulting from the Ramachandran plot analysis performed with PROCHECK calculated over residues 536–608 and 613–654. Values in parenthesis are calculated on the secondary structure elements:

α-Helices: 536–539, 550–555, 635–644, 646–658

β-Strands: 561–565, 570–572, 581–586, 588–592, 598–602, 606–607, 621–624, 628–633

‡Z-scores as they result from Common Interface for NMR Structure Generation (CING) (3) over residues 536–654.

§Raw and Z-scores as they result from PSVS over residues 536–654. Values in parentheses are calculated on the secondary structure elements (4).

1. Güntert P, Mumenthaler C, Wüthrich K (1997) Torsion angle dynamics for NMR structure calculation with the new program DYANA. *J Mol Biol* 273(1):283–298.
2. Case DA, et al. (2012) AMBER 12 (University of California, San Francisco).
3. Doreleijers JF, et al. (2012) CING: An integrated residue-based structure validation program suite. *J Biomol NMR* 54(3):267–283.
4. Bhattacharya A, Tejero R, Montelione GT (2007) Evaluating protein structures determined by structural genomics consortia. *Proteins* 66(4):778–795.

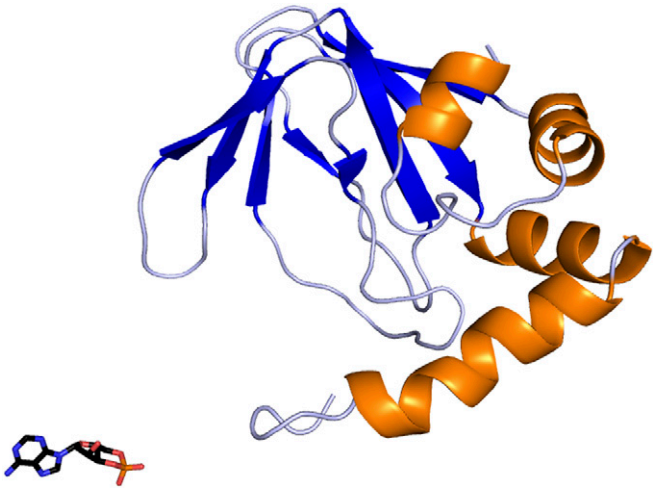

Movie S1. cAMP-induced conformational changes in the CNBD of human HCN2. Upon ligand binding (cAMP), the CNBD undergoes major rearrangements in the helical component (orange), including secondary structure formation (highlighted in red), whereas only minor movements are observed in the β-roll (blue).

Movie S1

Bimodal interaction between HCN channels and TRIP8b revealed through structural characterization of the protein complex

Andrea Saponaro[1], Francesca Cantini[2], Alessandro Porro[1], Annalisa Bucchi[1], Vincenzo Maione[2], Chiara Donadoni[1], Bianca Introini[1], Dario Di Francesco[1], Gerhard Thiel[3], Lucia Banci[2,4], Bina Santoro[5], Anna Moroni[1,6,*]

[1]Department of Biosciences University of Milan, Italy;

[2]Centro Risonanze Magnetiche (CERM) and Department of Chemistry, University of Florence, Italy;

[3]Department of Biology, TU-Darmstadt, Darmstadt, Germany;

[4]Institute of Neurosciences, Consiglio Nazionale delle Ricerche, Florence, Italy

[5]Department of Neuroscience, Columbia University, New York, USA;

[6]Institute of Biophysics, Consiglio Nazionale delle Ricerche, Milan, Italy.

* Corresponding author: Anna Moroni, Department of Biosciences, Via Celoria 26, 20133 Milano, Italy, tel. + 39 12 50314826, email: anna.moroni@unimi.it

BIOLOGICAL SCIENCES: Agricultural Sciences; Anthropology; Applied Biological Sciences; Biochemistry; Biophysics and Computational Biology; Cell Biology; Developmental Biology; Ecology; Environmental Sciences; Evolution; Genetics; Immunology and Inflammation; Medical Sciences; Microbiology; Neuroscience; Pharmacology; Physiology; Plant Biology; Population Biology; Psychological and Cognitive Sciences; Sustainability Science; and Systems Biology.

Keywords: HCN channels, TRIP8b, cAMP, allosteric inhibition, direct competition

Abstract

The auxiliary subunit TRIP8b prevents cAMP activation of HCN channels by antagonizing its binding to their cyclic-nucleotide binding domain (CNBD). By determining an NMR-derived structure of the complex formed by the HCN2 channel CNBD and a minimal TRIP8b fragment, we show here a bipartite interaction between TRIP8b and CNBD which prevents cAMP binding in two ways: through direct competition for binding at the distal C-helix of the CNBD; and through an allosteric reduction in cAMP affinity induced by TRIP8b binding to the CNBD N-bundle loop. Detailed structural knowledge of the TRIP8b/CNBD complex further allowed the engineering of an HCN channel whose gating responds selectively to cAMP, but not to TRIP8b, while leaving TRIP8b regulation of channel trafficking unaltered. Finally, we designed and produced a peptide, $TRIP8b_{nano}$, able to prevent cAMP binding in native HCN channels. Application of $TRIP8b_{nano}$ in sinoatrial node myocytes mimics the effect of physiological concentrations of acetylcholine leading to a 30% reduction in heart rate.

Significance statement

Hyperpolarization activated cyclic nucleotide gated (HCN) channels are key regulators of heart rate and neuronal excitability. Insights into modulation of their activity can lead to therapeutic intervention in cases of disease associated with electrical dysfunctions of cells. Here we present the structural model of the complex formed by the cyclic nucleotide binding domain (CNBD) of HCN channels and their regulatory subunit TRIP8b. The model explains in molecular detail the competition between cAMP and TRIP8b for binding to the CNBD, and how TRIP8b inhibits channel activity. On this basis we were able to design a small peptide,

TRIP8b$_{nano}$, which binds to the cardiac isoform HCN4 and acts as a bradycardic agent reducing heart rate by about 30 % in isolated cardiomyocytes.

Introduction

Hyperpolarization-activated cyclic nucleotide-regulated (HCN1-4) channels are the molecular correlate of the I_f/I_h current, which plays a key role in controlling several higher order electrophysiological functions, including dendritic integration and intrinsic rhythmicity both in cardiac and neuronal cells (1). Unique among the voltage-gated ion channel superfamily, HCN channels are modulated by the direct binding of cAMP to their C-terminal CNBD. cAMP binding enhances channel opening upon hyperpolarization via conformational changes in the CNBD that are propagated, through the C-linker domain, to the pore (2, 3).

In addition to cAMP, HCN channels are regulated by TRIP8b, their brain-specific auxiliary (β) subunit, which modulates channel trafficking and gating (4, 5). TRIP8b binds HCN channels in two distinct sites: the tetratricopeptide repeat (TPR) domain, which binds the last three amino acids (SNL) of HCN channels; and the TRIP8b$_{core}$ domain, which interacts with the HCN channel CNBD domain (6). Although TRIP8b is subject to alternative splicing giving rise to nine isoforms with different effects on HCN trafficking (4), all isoforms act in the same way on the electrical activity of HCN channels: they bind to the cAMP-free state of the CNBD and thus antagonize the effect of the ligand on the voltage dependency of the channel (7).

In previous work, we contributed to elucidating the dual mechanism of action of cAMP and TRIP8b on HCN channels by using a simplified system that included the HCN2 CNBD and the TRIP8b$_{core}$ protein fragments (8). By means of solution NMR spectroscopy we described in atomic detail the cAMP-induced conformational changes occurring in the HCN channel CNBD. These include a major rearrangement of the C-terminal helix of the CNBD (C-helix), which undergoes lateral translation and folding upon cAMP binding; and an upward

movement of the N-terminal helical bundle, a helix-turn-helix motif immediately upstream of the CNBD β-roll, which presumably initiates the cAMP-induced facilitation of pore opening. These movements are ostensibly inhibited by TRIP8b binding to both the C-helix and N-terminal helical bundle, thus explaining the allosteric inhibition exerted by TRIP8b on the HCN channel response to cAMP (7). The above TRIP8b interaction sites were validated by deletion analysis, confirming that both the N-terminal helical bundle and the C-helix are necessary but not sufficient for $TRIP8b_{core}$ binding to the CNBD (8). Despite these findings, several reports have suggested a direct competition mechanism between the two ligands for a common binding region that comprises the C-helix and the phosphate binding cassette, PBC, in the HCN channel CNBD (9–11).

A comprehensive structural model of the complex between TRIP8b and the HCN channel CNBD, which may explain the interaction in atomic detail, is therefore crucial for solving the apparent discrepancies between the two proposed models.

We present here a NMR-based 3D model structure of the complex formed by a minimal TRIP8b fragment and the CNBD of the human HCN2 channel isoform, which provides molecular support for both direct and indirect (allosteric) competition modes exerted by TRIP8b on cAMP binding. Our model further allowed the identification of a site-specific mutation in HCN that reduces TRIP8b binding to the CNBD without affecting its effect on channel trafficking. Such mutation constitutes a valuable tool for future dissection of the multiple TRIP8b actions and for a characterization of the cAMP-TRIP8b regulatory system *in vivo*. Finally, in an effort to obtain high-quality NMR data, we have identified a minimal peptide, $TRIP8b_{nano}$, which we successfully employed to manipulate the native I_f current in cardiac pacemaker cells. This result opens the possibility of controlling *in vivo* the cAMP-dependent facilitation of HCN channel opening, which represents the basis for the autonomic regulation of cardiac activity and spontaneous neuronal firing (1).

Results

We have previously shown that TRIP8b$_{core}$ (residues 223 - 303 of mouse TRIP8b splice variant 1a4, hereafter TRIP8b) interacts with two elements of the isolated CNBD protein fragment from HCN channels (residues 521 - 672 of human HCN2, hereafter CNBD): the C-helix and the N-bundle loop, a sequence connecting helix E' of the C-linker with helix A of the CNBD (8). Biochemical assays confirmed that each of these two elements i.e. the N-bundle loop and C-helix is necessary but not sufficient for binding (8).

To understand the interaction in atomic detail, we used solution NMR spectroscopy to characterize the structural properties of the CNBD-TRIP8b$_{core}$ complex. However, the NMR spectra of TRIP8b$_{core}$ showed very few signals. In order to improve the quality of the NMR spectra, we reduced the length of the TRIP8b fragment by progressively removing residues at the N- and C-termini with no predicted secondary structure. The truncated peptides were then tested for CNBD binding activity by isothermal titration calorimetry (ITC). We thus identified a 40 amino acid peptide (TRIP8b$_{nano}$, comprising residues 235 – 275 of TRIP8b) with a binding Kd of 1.5 μM, a value very similar to the Kd of 1.2 μM obtained with TRIP8b$_{core}$ (Fig. S1A, Table 1). TRIP8b$_{nano}$ was therefore employed for all subsequent NMR experiments, resulting in a remarkable improvement in the spectral quality and sample stability.

Structural characterization of TRIP8b$_{nano}$ bound to CNBD. The comparison of the ^{1}H-^{15}N HSQC spectra of TRIP8b$_{nano}$ with and without CNBD bound shows that the peptide folds upon interaction with the CNBD. Thus, a larger number of well-dispersed amide signals appear in the spectrum of the CNBD-bound form (Fig. S1B). Importantly, we were now able

to assign the backbone chemical shift resonances of TRIP8b$_{nano}$ bound to the CNBD. The φ and ψ dihedral angles obtained from the NMR assignment indicate that the peptide displays two α-helices (stretch L_{238}-E_{250} named helix N and stretch T_{253}-R_{269} named helix C) when bound to CNBD. The helices are separated by two amino acids; three and six residues at the N- and C- termini, respectively, are unstructured (Fig. 1).

Structural characterization of CNBD bound to TRIP8b$_{nano}$. NMR-analysis of the CNBD fragment bound to TRIP8b$_{nano}$ revealed that the interaction with the peptide does not affect the overall fold of the protein. Thus, the CNBD adopts the typical fold of the cAMP-free state, in line with previous evidence that this is the form bound by TRIP8b (8, 10). More specifically, the secondary structure elements of the cAMP- cAMP-free CNBD are all conserved in the TRIP8b$_{nano}$–bound CNBD (Fig. 2). This finding generally agrees with a recent double electron-electron resonance (DEER) analysis of the CNBD-TRIP8b interaction, which showed that TRIP8b binds to a conformation largely similar to the cAMP-free state (10). Despite the overall agreement with the DEER study, the NMR data also reveal a new and unexpected feature of TRIP8b binding to the CNBD. Our results surprisingly show that TRIP8b$_{nano}$ induces, upon binding to the CNBD, a well-defined secondary structure of the distal region of the C-helix (Fig. 2). This means that the distal region of the C-helix (residues 657-662), which is unstructured in the free form of the CNBD (8), extends into a helical structure upon ligand binding irrespectively of whether the ligand is cAMP (8, 12) or TRIP8b (Fig. 2). In contrast, and very differently from cAMP, which directly contacts the P-helix in the Phosphate Binding cassette (PBC) and causes its folding (8), the NMR data show that TRIP8b$_{nano}$ binding to the CNBD does not induce P-helix formation (Fig. 2).

Modelling the CNBD-TRIP8b$_{nano}$ complex. Despite the significant improvement in sample stability and NMR spectra quality achieved upon TRIP8b$_{nano}$ binding, we were still unable to assign the side chains of both proteins in the complex and thus could not solve the solution

structure of the complex by the canonical NMR procedure. We therefore built a model of the CNBD-TRIP8b$_{nano}$ complex by docking the two NMR-derived structures using the Haddock program (a detailed description of how the respective structures were generated is provided in SI Materials and Methods and Table S1).

In order to define the active residues (ambiguous interaction restraints) on the CNBD we used the chemical shift perturbation values as described in Fig. S2. For TRIP8b$_{nano,}$ we defined as active a stretch of residues, E_{239}-E_{243}, previously identified as critical for the interaction (4,6). Output clusters of this first molecular docking calculation (settings can be found in SI Material and Methods) were further screened for TRIP8b$_{nano}$ orientations in agreement with a previous DEER analysis, which placed TRIP8b residue A_{248} closer to the proximal portion and TRIP8b residue A_{261} closer to the distal portion of the CNBD C-helix (10). Remarkably, in all clusters thus selected, residues E_{264} or E_{265} in TRIP8b were found to interact with residues K_{665} or K_{666} of the CNBD (Fig. S3). This finding was notable, because we previously identified K_{665}/K_{666} as being critical for TRIP8b interaction in a biochemical binding assay (8). We thus proceeded to individually mutate each of these four positions, and test their effect on binding affinity through ITC. As expected, reverse charge mutations K_{665}E or K_{666}E (CNBD) as well as E_{264}K or E_{265}K (TRIP8b$_{nano}$) each strongly reduced the CNBD/TRIP8b$_{nano}$ binding affinity (Fig. S4).

Based on these observations, we performed a second molecular docking calculation, including E_{264} and E_{265} as additional active residues for TRIP8b$_{nano}$. This procedure resulted in the model shown in Fig. 3, which represents the top-ranking cluster for energetic and scoring function (Table S2) and was fully validated by mutagenesis analysis as described below. Scrutiny of the model shows that TRIP8b$_{nano}$ binds to both the C-helix and the N-bundle loop (Fig. 3A). Binding to the C-helix is mainly guided by electrostatic interactions between the negative charges on TRIP8b$_{nano}$, and the positive charges on the

CNBD (Fig. 3A). As shown in Fig. 3B, the model highlights a double saline bridge (K_{665} and K_{666} of CNBD with E_{265} and E_{264} of TRIP8b$_{nano}$) in line with the ITC results described above (Fig. S4). Of note, the contribution of residue R_{662} to the binding is also consistent with previous experiments showing residual TRIP8b interaction in a CNBD deletion mutant ending at position 663 (8). Our modelling data suggest that, upon folding of the distal portion of the C-helix, the side chains of residues R_{662} and R_{665} face to the inside when contacting cAMP but face to the outside when binding TRIP8b (Fig. S5).

In addition to clarifying the role of residues in the distal portion of the CNBD C-helix, the model also highlights a second important cluster of electrostatic interactions with R_{650} in the proximal portion of the CNBD C-helix contacting E_{240} and E_{241} in helix N of TRIP8b$_{nano}$ (Fig 3C). To confirm the contribution of these residues, we reversed charges and tested each residue mutation for binding in ITC. The results in Fig. S4 show that R_{650}E caused a more than six-fold reduction in binding affinity for TRIP8b$_{nano}$, with smaller but significant effects seen also for E_{240}R and E_{241}R.

A third important contact highlighted by the model is the interaction between N_{547} in the N-bundle loop of the CNBD and D_{252} in the link between helix N and helix C of TRIP8b$_{nano}$ (Fig. 3D). We tested this potential interaction by disrupting the expected hydrogen bond between N_{547} and the carboxyl group of the negative residue (D_{252}) in TRIP8b$_{nano}$. The asparagine in CNBD was mutated into aspartate (N_{547}D) to generate an electrostatic repulsion for D_{252}, and the carboxyl group in D_{252} of TRIP8b$_{nano}$ was removed by mutation into asparagine (D_{252}N). As predicted, N_{547}D greatly reduced binding to TRIP8b in ITC assays (Fig. S4, and Table 1), with a smaller but significant effect observed also for D_{252}N (Fig. S4). These results confirm and extend our previous finding that the N-bundle loop contributes in a substantial manner to the binding of TRIP8b (8).

Developing genetic tools for the regulation of HCN currents in cells. While several studies have addressed the importance of residues in the CNBD C-helix for binding to both cAMP (3, 13) and TRIP8b (Fig. 3; and (8)), no mutagenesis studies have been performed on residues within the N-bundle loop. Furthermore, it has so far proven difficult to design specific mutations, which can affect TRIP8b binding without, at the same time, affecting cAMP binding. Identifying such mutations would allow to more effectively explore the role of TRIP8b in limiting the cAMP response of HCN channels *in vivo*. In addition, it would address the question whether the TRIP8b/cAMP competition for CNBD binding has an indirect allosteric component, as some studies have suggested (7, 8), in addition to the direct component highlighted above. To screen for such mutations, given the role of the CNBD C-helix in directly contacting cAMP, we focused our efforts on the N-bundle loop and proceeded to test candidate mutations for cAMP binding activity.

Somewhat surprisingly, when assessed for cAMP binding, we found the N-bundle loop $N_{547}D$ mutation to significantly affect cAMP binding affinity both in the CNBD fragment and in the full-length channel (Table 1, Fig. S6). NMR (15^{N}-HSQC spectrum) analysis of the $N_{547}D$ CNBD mutant confirmed that it is appropriately folded and therefore the effect on cAMP and $TRIP8b_{nano}$ affinity is not due to a global structural rearrangement (Fig. S7). Since the N-bundle loop does not make any direct contact with cAMP, this finding underscores a previously unaddressed role of the N-bundle loop in allosterically modulating cAMP binding to the CNBD (see Discussion).

As the $N_{547}D$ mutation did not satisfy our criteria for isolating TRIP8b binding from cAMP binding activity, we considered alternative mutations. Interestingly, the closely related CNG channels, which bind cAMP like HCN channels but do not bind TRIP8b (6), carry an aspartate instead of asparagine at the position corresponding to N_{547}, just like the $N_{547}D$ mutant. The aspartate in CNG is however followed by a second substitution, within an

otherwise highly conserved sequence, namely a cysteine instead of alanine (Fig. S8). To fully mimic the CNG channel sequence, we thus introduced a double point mutation in our HCN CNBD construct. Binding assays performed by ITC show that the HCN CNBD $N_{547}D/A_{548}C$ mutant displays a 6-fold decrease in the affinity for $TRIP8b_{nano}$ (Fig. S4, and Table 1). In contrast, the affinity for cAMP of the double mutation remains essentially unaltered (Table 1), as expected from the homology with CNG channels. Importantly, the loss of $TRIP8b_{nano}$ binding activity was largely rescued by pairing the $N_{547}D/A_{548}C$ double mutation in the CNBD with the $D_{252}N$ point mutation in $TRIP8b_{nano}$ (Fig. S4). The results of this swap experiment provide further demonstration that the $N_{547}D/A_{548}C$ double mutant is appropriately folded, and strongly support an interaction between residues in the CNBD N-bundle loop and the bend region between helix N and helix C of $TRIP8b_{nano,}$ as predicted by our model (Fig. 3D).

In light of these findings, we next tested whether the $N_{547}D/A_{548}C$ double mutation may also be able to affect TRIP8b binding (but not cAMP binding) in the more physiological context of a full-length channel expressed in living cells. We therefore recorded currents from HEK 293T cells co-transfected with HCN1 and TRIP8b (Fig. 4). Because of its higher affinity for cAMP, compared to the other HCN isoforms, the HCN1 isoform shows virtually a fully rightward shifted activation curve due to the endogenous cAMP levels present in HEK 293T cells (Fig. S9). When full-length TRIP8b (splice variant 1a4) is cotransfected with HCN1, the mid-activation point ($V_{1/2}$) of the channel is shifted significantly to hyperpolarized potentials (Fig. 4A). This reflects the fact that TRIP8b prevents cAMP binding to the channel. This 6 mV negative shift in the activation curve closely matches the shift recorded with the $R_{549}E$ mutation in the PBC of HCN1 (14), which essentially prevents cAMP binding (Fig. S9), suggesting that TRIP8b fully antagonizes the interaction of endogenous cAMP with the channel. As noted in previous studies (4, 15) cotransfection of TRIP8b(1a4) also has a

second effect on HCN1 channel function, namely a ~2.5-fold increase in maximal current density (Fig. 4B).

We thus introduced the $N_{547}D/A_{548}C$ double mutation in the background of the full-length HCN1 channel. Consistent with its effect on the isolated CNBD fragment, the double mutant had a rightward shifted $V_{1/2}$ identical to the wildtype HCN1 channel (Fig. 4A). This confirms an intact response of the mutant to endogenous cAMP. Strikingly, cotransfection with TRIP8b (1a4) was completely ineffective in preventing the facilitatory effect of cAMP on channel activation. At the same time, TRIP8b still exerted its normal positive effect on channel surface expression, as reflected by the increase in maximal current density of the mutant channel (Fig. 4B). It is worth remembering that full-length TRIP8b exerts its effect on channel trafficking in part by interacting with the last three amino acids of the channel (-SNL) which are still present in the full-length HCN1 construct (6).

In conclusion, the double mutation $N_{547}D/A_{548}C$ in the HCN CNBD is sufficient to prevent the effect of TRIP8b to cAMP, while having no impact on the role of TRIP8b to promote channel expression and trafficking.

TRIP8b$_{nano}$ as a tool for the direct regulation of native HCN currents. Next, we asked whether the relatively short TRIP8b$_{nano}$ peptide could be used to block the response of native HCN channels to cAMP by delivering the peptide *in vivo*. To this end, we dialyzed TRIP8b$_{nano}$ into the cytosol of HEK 293T cells transfected either with HCN1, HCN2, or HCN4 channels. The peptide was added (10 µM) in the recording pipette together with a non-saturating concentration of cAMP for each isoform (5 µM for HCN2, 1 µM for HCN4) expected to produce a ~10 mV rightward shift in $V_{1/2}$ in the wildtype channel. No cAMP was added in the case of HCN1, as this isoform is already fully shifted by low endogenous cAMP levels (Fig. 4A and Fig. S9). The results of the respective recordings in the presence and absence of

TRIP8b$_{nano}$ show that the peptide fully abolished the cAMP-induced potentiation of channel opening in all HCN isoforms (Fig. S10).

Thus, we reckoned it may be employed as a regulatory tool for native I_f/I_h currents. As proof of principle, we tested whether TRIP8b$_{nano}$ can modulate the frequency of action potential firing in sinoatrial node (SAN) cells. In these cells, I_f contributes substantially to the diastolic depolarization phase of the action potential. Moreover, the autonomic nervous system modulates the frequency of action potential firing by changing intracellular cAMP levels, which in turn acts on HCN channel open probability (16). The native I_f current from cardiomyocytes acutely isolated from rabbit sinoatrial node (SAN) was recorded with and without 10 μM TRIP8b$_{nano}$ in the pipette solution. Figure 5A shows that the activation curve recorded in presence of TRIP8b$_{nano}$ is significantly hyperpolarized compared to the control. This indicates that the peptide is displacing the binding of endogenous cAMP to native HCN channels. Moreover, when the experiment was repeated in the presence of 1 μM cAMP, TRIP8b$_{nano}$ prevented the typical cAMP-dependent potentiation of the native I_f current (Fig. 5A). In light of these results, we tested whether TRIP8b$_{nano}$ is also able to modulate cardiac automaticity by antagonizing basal cAMP. The data in Fig. 5B show that TRIP8b$_{nano}$ indeed significantly decreased the rate of action potential firing in single SAN cells. Strikingly, the observed 30% decrease in action potential rate corresponds to the effect induced by physiological concentrations of acetylcholine (17).

Discussion

TRIP8b-CNBD complex. In the present study, we describe the interaction between TRIP8b and the HCN channel CNBD at atomic level, based on a NMR-derived structural model of their complex. The data show that the minimal binding unit of TRIP8b, TRIP8b$_{nano}$, folds in two helices upon binding, suggesting that this region of the regulatory subunit has an intrinsically disordered behavior when not in the complex. The model structurally validates

previous indirect evidence, which suggested that TRIP8b binds to two different elements of the CNBD, the N-bundle loop and the C-helix. As a consequence of the interaction with TRIP8b$_{nano}$, the C-helix in the CNBD increases in length, a behavior already observed in the case of cAMP binding. The model also identifies residues R_{662} and K_{665} in the CNBD as interaction partners with TRIP8b$_{nano}$, two cationic residues also involved in cAMP binding (13). The finding that TRIP8b and cAMP share binding sites on the C-helix provides a solid molecular explanation for functional data which underscore a competition between the two regulators (9–11). However, it has been previously suggested that a direct competition model does not fully explain the mutually antagonistic effect of the two ligands (7). Specifically, the fact that the inhibitory effect of TRIP8b on channel activity persists even at saturating cAMP concentrations suggests an allosteric component in the regulation mechanism. Our structural model provides the missing molecular evidence for this allosteric component. TRIP8b$_{nano}$ binds to the solvent-exposed elements of CNBD (N-bundle loop and C-helix) and does not interact directly with the buried PBC, which remains unfolded, as demonstrated by the observation that the P-helix does not form upon TRIP8b binding. This rules out the possibility that TRIP8b$_{nano}$ controls the affinity for cAMP by directly binding to the PBC. Rather, it confirms that the PBC in the complex is indirectly kept in the low affinity state for cAMP binding (unfolded form) through allosteric long-range interactions.

Our mutagenesis analysis of the N-bundle loop further demonstrates that the N-terminal helical bundle of the CNBD plays a crucial role not only in the propagation of the cAMP signal to the channel pore (8) but also in the allosteric control of cAMP affinity. Our data show that the single mutation $N_{547}D$ affects cAMP binding both in the isolated CNBD and in the full-length HCN2 channel, even though the mutation is far from the cAMP binding site. This finding is well fitting with the allosteric control of cAMP affinity exerted by TRIP8b via its interaction with the same residue in the N-bundle loop. In addition, our results indicate

that the N-terminal helical bundle strategically controls the gating pathway in both directions: from the CNBD to the transmembrane portion of the channel and, vice versa, from the transmembrane portion to the CNBD, a view also supported by experimental results showing that voltage sensor movement and activation gate elements can regulate the affinity of CNBD for cAMP (18, 19).

$N_{547}D/A_{548}C$ mutation. Guided by the molecular model described above, we identified and characterized the mutation $N_{547}D/A_{548}C$ in the CNBD of HCN2 channels ($N_{478}D/A_{479}C$ in HCN1) which selectively abolishes TRIP8b regulation without affecting cAMP regulation. The behaviour of this double mutation has a dual implication: it functionally proves the allosteric model of TRIP8b vs. cAMP binding to the CNBD; and it provides a tool for *in vivo* studies of HCN channels which are fully sensitive to cAMP, without any interference by the TRIP8b auxiliary subunit. Because TRIP8b is essential for the proper surface expression of HCN channels, simply abolishing TRIP8b expression *in vivo* through genetic deletion has not allowed such question to be addressed, as knockout of TRIP8b results in drastically reduced HCN channel currents and protein (20). The observation that the $N_{547}D/A_{548}C$ mutation does not prevent the effects of TRIP8b on channel trafficking means it may be employed as a genetic tool for dissecting the binary cAMP – TRIP8b regulatory system of HCN channels in the brain. As the sensitivity of neuronal HCN channels to cAMP is critical in several physiological contexts (21–24), it would be interesting to determine the consequences of an unabated response of HCN channels to cyclic nucleotides, as allowed by the absence of TRIP8b.

$TRIP8b_{nano}$ as a tool for inhibiting adrenergic regulation of I_f. $TRIP8b_{nano}$ is a minimal protein fragment, which binds the HCN channel CNBD with high affinity and fully abolishes the cAMP effect in all tested isoforms (HCN1, 2 and 4). Given the small size of the peptide (<5kD), $TRIP8b_{nano}$ may be easily adapted for *in vivo* delivery, and thus constitutes a

promising tool for the study or modulation of native HCN channels in systems where the regulatory protein is not expressed, or is expressed at low levels. Our structural model explains why a previous attempt at identifying the minimal domain required for TRIP8b activity resulted in a peptide with strongly reduced CNDB affinity, as the fragment selected in the study by Lyman et al (25) is lacking an important contact residue (E_{240}). In the present study, we successfully used $TRIP8b_{nano}$ to control native I_f currents and pacemaking in rabbit sinoatrial node cardiomyocytes. Unlike channel blockers, which inhibit ionic currents, the peptide only interferes with the cAMP-based regulation of HCN channels, while leaving basal HCN functions unaltered. In addition, and in contrast to even the most selective blockers, it is entirely specific for HCN channels. The ability to selectively control a specific molecular mechanism to modulate channel activity represents a novel approach, which yields the promise of a more targeted therapeutic intervention compared to pore blockers.

ACKNOWLEDGEMENTS

This work has been supported by Fondazione CARIPLO grant 2014-0796 to A.M., B.S and L.B., by 2016 Schaefer Research Scholars Program of Columbia University to A.M., by National Institutes for Health Grant R01 NS036658 to B.S., by Instruct-ERIC and national member subscriptions to L.B, and by Accademia Nazionale dei Lincei (Giuseppe Levi foundation) to A.S. We specially thank the EU ESFRI Instruct Core Centre CERM-Italy.

Materials and Methods

Preparation of proteins. Samples were prepared as previously described (8)

Isothermal Titration Calorimetry. Measurements were carried out at 25 °C using an VP-ITC MicroCalorimeter (MicroCal, GE Healthcare) as previously described (8).

NMR data. NMR experiments were acquired on Bruker Avance III 950, 700 and 500 MHz NMR spectrometers equipped with a TXI-cryoprobe at 298 K. A detailed description of NMR experiments and structure calculations is provided in *SI Materials and Methods.*

Docking Calculation. Docking calculations were performed with HADDOCK2.2 implemented in the WeNMR/West-Life GRID-enabled web portal (www.wenmr.eu). A detailed description of the calculations is provided in *SI Materials and Methods*.

Electrophysiology. A detailed description of all HEK 293T and cardiomyocytes recording conditions and measurements is provided in *SI Materials and Methods*.

1. Robinson RB, Siegelbaum SA (2003) Hyperpolarization-Activated Cation Currents: From Molecules to Physiological Function. *Annu Rev Physiol* 65(1):453–480.
2. Wainger BJ, DeGennaro M, Santoro B, Siegelbaum SA, Tibbs GR (2001) Molecular mechanism of cAMP modulation of HCN pacemaker channels. *Nature* 411(6839):805–810.
3. Zagotta WN, et al. (2003) Structural basis for modulation and agonist specificity of HCN pacemaker channels. *Nature* 425(6954):200–205.
4. Santoro B, et al. (2009) TRIP8b Splice Variants Form a Family of Auxiliary Subunits that Regulate Gating and Trafficking of HCN Channels in the Brain. *Neuron* 62(6):802–813.
5. Zolles G, et al. (2009) Association with the auxiliary subunit PEX5R/Trip8b controls responsiveness of HCN channels to cAMP and adrenergic stimulation. *Neuron* 62(6):814–825.
6. Santoro B, et al. (2011) TRIP8b Regulates HCN1 Channel Trafficking and Gating through Two Distinct C-Terminal Interaction Sites. *J Neurosci* 31(11):4074–4086.
7. Hu L, et al. (2013) Binding of the auxiliary subunit TRIP8b to HCN channels shifts the mode of action of cAMP. *J Gen Physiol* 142(6):599–612.
8. Saponaro A, et al. (2014) Structural basis for the mutual antagonism of cAMP and TRIP8b in regulating HCN channel function. *Proc Natl Acad Sci U S A* 111(40):14577–14582.
9. Han Y, et al. (2011) Trafficking and gating of hyperpolarization-activated cyclic nucleotide-gated channels are regulated by interaction with tetratricopeptide repeat-containing Rab8b-interacting protein (TRIP8b) and cyclic AMP at distinct sites. *J Biol Chem* 286(23):20823–20834.
10. Deberg HA, et al. (2015) Structural mechanism for the regulation of HCN ion channels by the accessory protein TRIP8b. *Structure* 23(4):734–744.
11. Bankston JR, DeBerg HA, Stoll S, Zagotta WN (2017) Mechanism for the inhibition of the cAMP dependence of HCN ion channels by the auxiliary subunit TRIP8b. *J Biol Chem*. doi:10.1074/jbc.M117.800722.
12. Puljung MC, Zagotta WN (2013) A secondary structural transition in the C-helix promotes gating of cyclic nucleotide-regulated ion channels. *J Biol Chem* 288(18):12944–12956.

13. Zhou L, Siegelbaum SA (2007) Gating of HCN channels by cyclic nucleotides: residue contacts that underlie ligand binding, selectivity, and efficacy. *Structure* 15(6):655–670.

14. Chen S, Wang J, Siegelbaum SA (2001) Properties of Hyperpolarization-Activated Pacemaker Current Defined by Coassembly of Hcn1 and Hcn2 Subunits and Basal Modulation by Cyclic Nucleotide. *J Gen Physiol* 117(5):491–504.

15. Lewis AS, et al. (2009) Alternatively spliced isoforms of TRIP8b differentially control h channel trafficking and function. *J Neurosci* 29(19):6250–6265.

16. DiFrancesco D (1993) Pacemaker mechanisms in cardiac tissue. *Annu Rev Physiol* 55:455–472.

17. DiFrancesco D, Ducouret P, Robinson RB (1989) Muscarinic modulation of cardiac rate at low acetylcholine concentrations. *Science (80-)* 243(4891):669–671.

18. Kusch J, et al. (2010) Interdependence of receptor activation and ligand binding in hcn2 pacemaker channels. *Neuron* 67(1):75–85.

19. Wu S, et al. (2012) Inner activation gate in S6 contributes to the state-dependent binding of cAMP in full-length HCN2 channel. *J Gen Physiol* 140(1):29–39.

20. Lewis AS, et al. (2011) Deletion of the Hyperpolarization-Activated Cyclic Nucleotide-Gated Channel Auxiliary Subunit TRIP8b Impairs Hippocampal Ih Localization and Function and Promotes Antidepressant Behavior in Mice. *J Neurosci* 31(20):7424–7440.

21. McCormick DA, Pape HC (1990) Noradrenergic and serotonergic modulation of a hyperpolarization-activated cation current in thalamic relay neurones. *J Physiol* 431:319–342.

22. McCormick DA, Pape HC (1990) Properties of a hyperpolarization-activated cation current and its role in rhythmic oscillation in thalamic relay neurones. *J Physiol* 431:291–318.

23. Wang M, et al. (2007) α2A-Adrenoceptors Strengthen Working Memory Networks by Inhibiting cAMP-HCN Channel Signaling in Prefrontal Cortex. *Cell* 129(2):397–410.

24. Marcelin B (2012) Dorsoventral Differences in Intrinsic Properties in Developing CA1 Pyramidal Cells. *J Neurosci* 32(11):3736–47.

25. Lyman KA, et al. (2017) Allostery between two binding sites in the ion channel subunit TRIP8b confers binding specificity to HCN channels. *J Biol Chem*. doi:10.1074/jbc.M117.802256.

Figures and Table

Table 1. cAMP and TRIP8b peptides binding to CNBD WT and mutants.

Titrant	CNBD	K_D ± SEM (µM)	n
$TRIP8b_{core}$	WT	1.2 ± 0.1	3
$TRIP8b_{nano}$	WT	1.5 ± 0.1	3
	$N_{547}D$	11.0 ± 0.9	3
	$N_{547}D/A_{548}C$	9.3 ± 0.9	3
cAMP	WT	1.4 ± 0.1	3
	$N_{547}D$	5.5 ± 0.4	3
	$N_{547}D/A_{548}C$	1.1 ± 0.1	3

Isothermal titration calorimetry (ITC) measurements of $TRIP8b_{core}$, $TRIP8b_{nano}$ and cAMP binding to His_6-MBP tagged CNBD proteins.

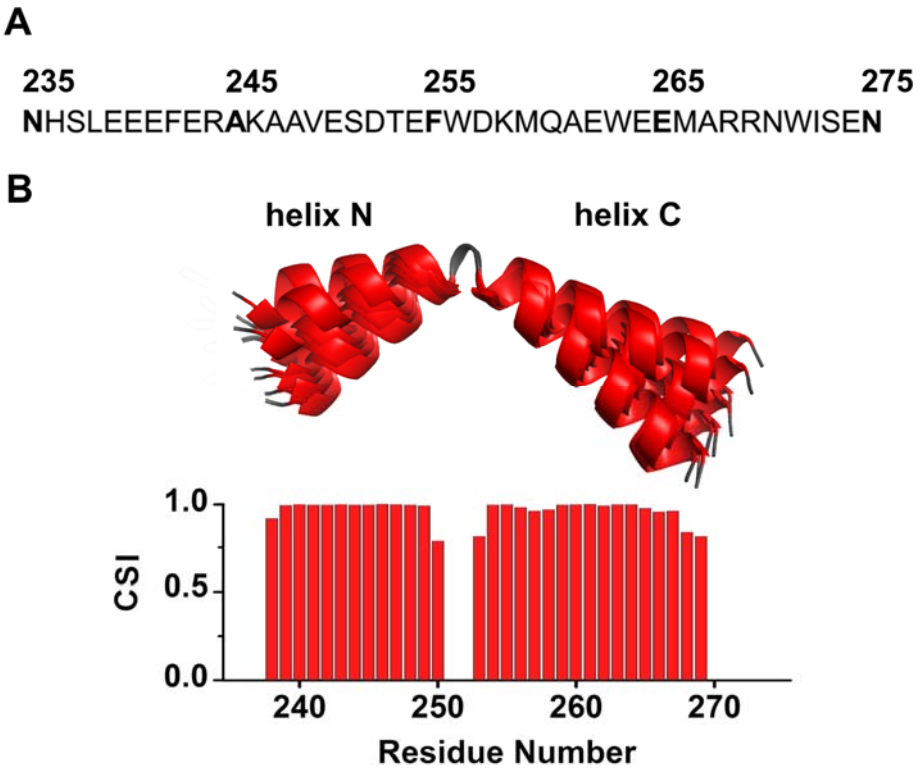

Fig. 1. NMR structure of TRIP8b$_{nano}$ bound to CNBD. (A) Primary sequence of TRIP8b$_{nano}$. Amino acid numbering refers to full length mouse TRIP8b (1a4). (B, *Upper*) Ribbon representation of the 10 lowest energy conformers of TRIP8b$_{nano}$ bound to CNBD used for *in silico* modelling of CNBD-TRIP8b$_{nano}$ complex. The unfolded regions at the N- and C-termini of the construct (residues 235–237 and 270 – 275) are omitted for clarity. (B, *Lower*) Chemical Shift Index (CSI, calculated using TALOS+) plotted as a function of the residue number of TRIP8b$_{nano}$. Positive values represent helical propensity.

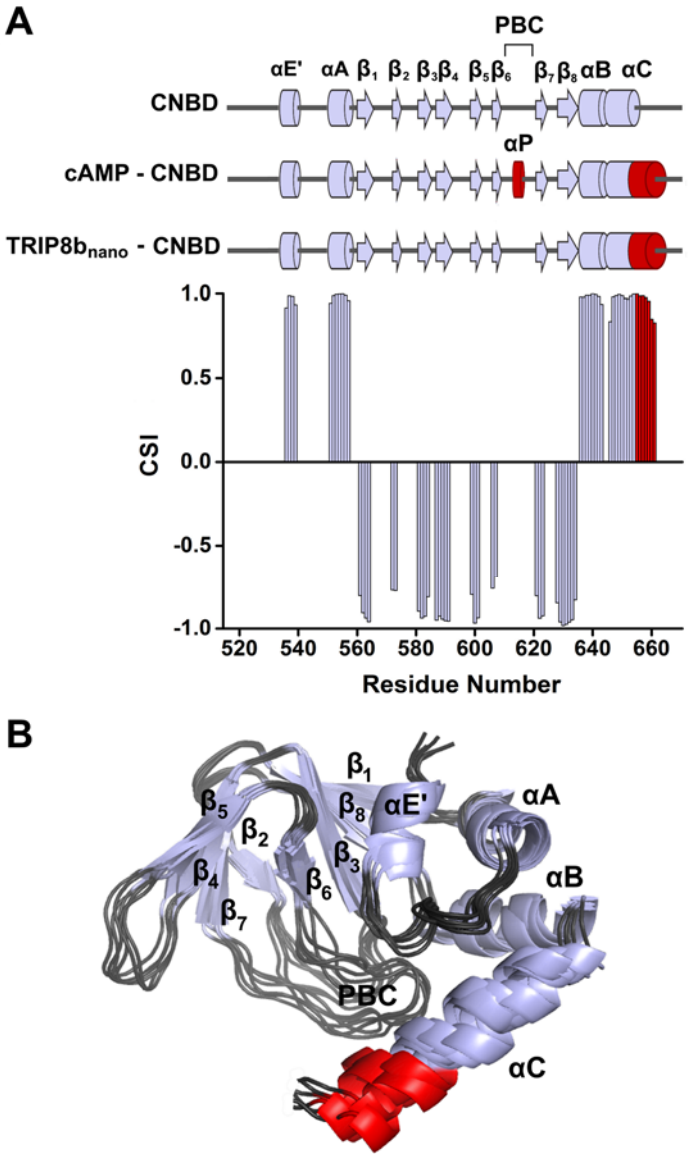

Fig. 2. NMR structure of CNBD bound to TRIP8b$_{nano}$. (A, *Upper*) comparison of secondary structure elements of cAMP-free CNBD (7), cAMP-bound CNBD (3) and cAMP-free CNBD bound to TRIP8b$_{nano}$ (this study). Secondary structure elements are indicated by arrows (β-strands) and cylinders (α-helices) and labelled. The loop between β$_6$ and β$_7$ constitutes the Phosphate Binding Cassette (PBC). The elements that fold upon binding of cAMP and TRIP8b$_{nano}$ are shown in red. (A, *Lower*) Chemical Shift Index (CSI, calculated using TALOS+) plotted as a function of the residue number of CNBD bound to TRIP8b$_{nano}$. Positive values represent helical propensity, while negative values represent strands. (B) Ribbon representation of the 10 lowest energy conformers of CNBD bound to TRIP8b$_{nano}$ used for *in silico* modelling of CNBD-TRIP8b$_{nano}$ complex. Secondary structure elements are coloured in light gray and labelled. Loop regions are coloured in dark gray. The unfolded

regions at the N- and C-termini of the construct (residues 521–532 and 663 – 672 respectively) are omitted for clarity.

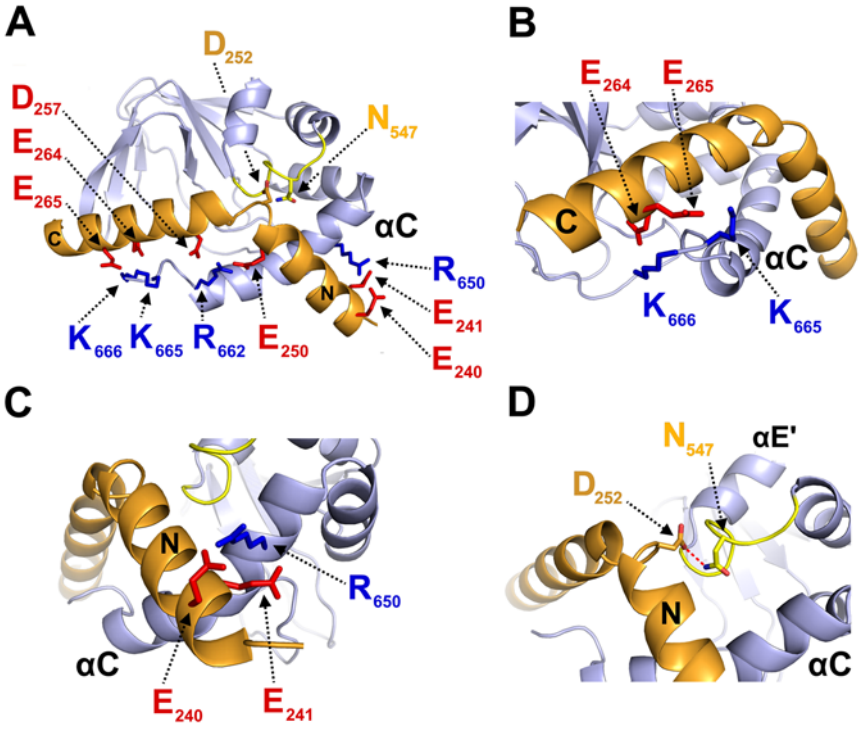

Fig. 3. Structural model of CNBD–TRIP8b$_{nano}$ complex. (A) Ribbon representation of the complex where CNBD is in gray and TRIP8b$_{nano}$ is in orange. Helix N (N) and helix C (C) of TRIP8b$_{nano}$ are labelled. C-helix of CNBD (αC) is labelled, while N-bundle loop is coloured in yellow. Positively charged residues of C-helix CNBD (blue) and negatively charged residues of TRIP8b$_{nano}$ (red) involved in salt bridges, are shown as sticks and labelled. N_{547} of the N-bundle loop (yellow) and D_{252} of TRIP8b$_{nano}$ (orange) are shown and labelled. (B) Close view of K_{665} and K_{666} of CNBD that interact respectively with E_{265} and E_{264} of TRIP8b$_{nano}$. (C) Close view of R_{650} of CNBD that is positioned between E_{240} and E_{241} of TRIP8b$_{nano}$. (D) Close view of N_{547} of N-bundle loop that forms a hydrogen bond (red dashed line) with D_{252} of TRIP8b$_{nano}$. Helix E' (αE') and C-helix (αC) of CNBD, and Helix N (N) of TRIP8b$_{nano}$ are labelled.

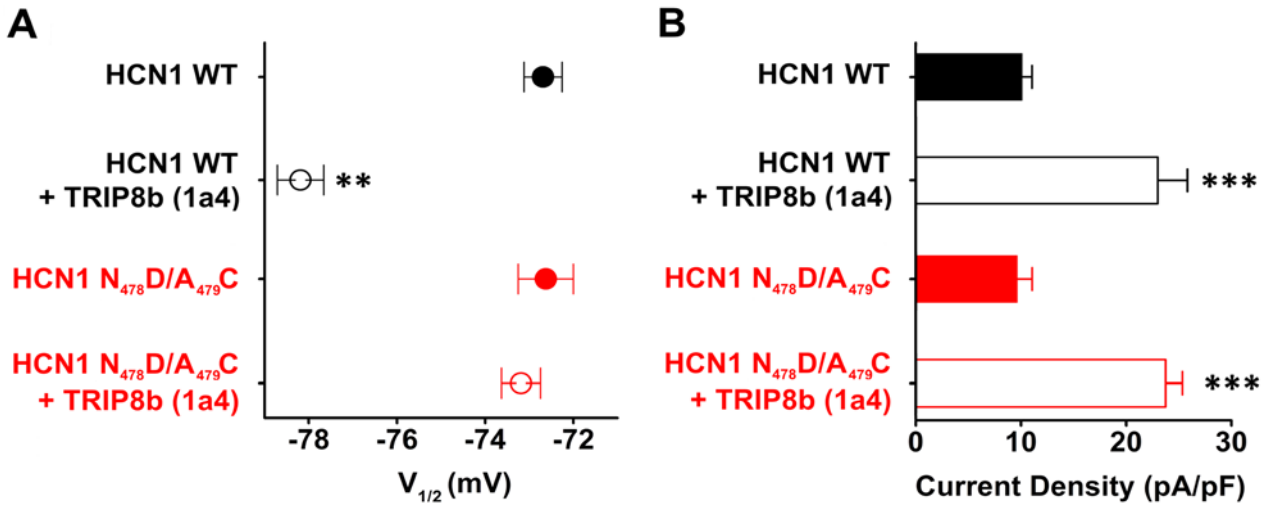

Fig. 4. The double mutation $N_{478}D/A_{479}C$ of human HCN1 prevents TRIP8b regulation of channel function. HCN1 currents were recorded from HEK 293T cells co-transfected with TRIP8b (1a4) and analysed as described in *SI Material and Methods*. (A) Half activation potential ($V_{1/2}$) of HCN1 WT (black filled circle) = -72.7 ± 0.4 mV; HCN1 WT + TRIP8b (1a4) (black open circle) = -78.2 ± 0.5 mV; HCN1 $N_{478}D/A_{479}C$ (red filled circle) = -72.6 ± 0.6 mV; HCN1 $N_{478}D/A_{479}C$ + TRIP8b (1a4) (red open circle) = -73.2 ± 0.4 mV. (B) Maximal tail current density (pA/pF) of HCN1 WT (black filled bar) = 10.1 ± 2.7 pA/pF; HCN1 WT + TRIP8b (1a4) (black open bar) = 23 ± 8 pA/pF; HCN1 $N_{478}D/A_{479}C$ (red filled bar) = 9.6 ± 4 pA/pF; HCN1 $N_{478}D/A_{479}C$ + TRIP8b (1a4) (red open bar) = 23.8 ± 4.5 pA/pF. Data are presented as means ± SEM. Number of cells (N) was = 8. Statistical analysis performed with ANOVA, followed by post-hoc Tukey test (**, $P < 0.01$; ***, $P < 0.001$).

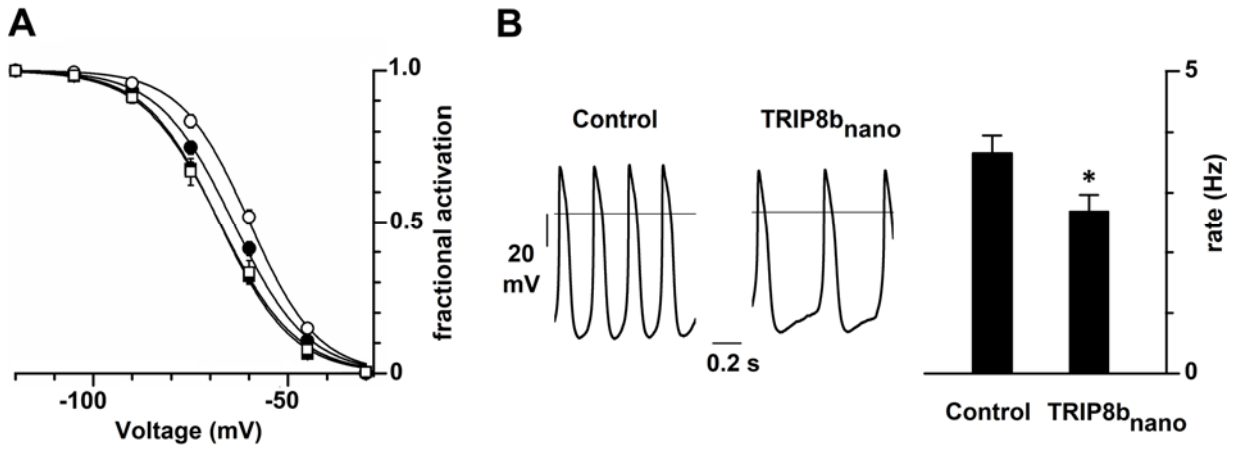

Fig. 5. Effects of TRIP8b$_{nano}$ on voltage-dependent activation of I_f and spontaneous rate in rabbit sinoatrial node (SAN) myocytes. (A) Mean I_f activation curves measured in control (filled circles) or in the presence of: 1 μM cAMP (open circles); 10 μM TRIP8b$_{nano}$ (filled squares); 1 μM cAMP + 10 μM TRIP8b$_{nano}$ (open squares). Ligands were added in the patch pipette. Half activation potential ($V_{1/2}$) of I_f activation curves measured in control = -64.1 ± 0.4 mV or in the presence of: 1 μM cAMP = -59.9 ± 0.4 mV; 10 μM TRIP8b$_{nano}$ = -67.7 ± 0.4 mV; 1 μM cAMP + 10 μM TRIP8b$_{nano}$ = -67.6 ± 0.7 mV. Data are presented as means ± SEM. Number of cells (N) was ≥ 15. $V_{1/2}$ values are significantly different with the exception of $V_{1/2}$ obtained in the presence TRIP8b$_{nano}$ and cAMP + TRIP8b$_{nano}$. Statistical analysis performed with ANOVA, followed by post-hoc Bonferroni test (*, $P < 0.05$) (B, *Left*) Representative recordings of single SAN cell spontaneous activity in control and in the presence of 10 μM TRIP8b$_{nano}$. (B, *Right*) Mean spontaneous rate (Hz) recorded in control solution and in the presence of 10 μM TRIP8b$_{nano}$ added to the pipette. Statistical analysis performed with t test (*, $P < 0.05$).

Supporting Information

SI Materials and Methods

Constructs. The cDNA fragment encoding residues 235 – 275 (TRIP8b$_{nano}$) of mouse TRIP8b (splice variant 1a4) was cloned into pET-52b (EMD Millipore) downstream of a Strep (II) tag sequence, while the cDNA fragment encoding residues 521–672 of human HCN2 (HCN2 CNBD) was cloned, in a previous study, into a modified pET-24b downstream of a double His$_6$-maltose-binding protein (MBP) (1). The cDNA encoding full-length human HCN1 channel, mouse HCN2 channel, rabbit HCN4 channel and mouse TRIP8b (1a4) were cloned into the eukaryotic expression vector pcDNA 3.1 (Clontech Laboratories). Mutations were generated by site-directed mutagenesis (QuikChange site-directed mutagenesis kit; Agilent Technologies) and confirmed by sequencing.

Structure calculation of the cAMP-free human HCN2 CNBD in complex with TRIP8b$_{nano}$ and vice versa. The acquired triple resonance NMR experiments for the assignment of backbone resonances of cAMP-free HCN2 CNBD (CNBD hereafter) in complex with TRIP8b$_{nano}$ and vice versa are summarized in Table S1. ^{15}N, $^{13}C'$, $^{13}C_{\alpha}$, $^{13}C_{\beta}$, and H_{α} chemical shifts were used to derive ϕ and ψ dihedral angles by TALOS+ program (2) for both CNBD and TRIP8b$_{nano}$. For TRIP8b$_{nano}$, CYANA-2.1 structure calculation (3) was performed using 68 ϕ and ψ dihedral angles and 40 backbone hydrogen bonds as input. For CNBD, CYANA-2.1 structure calculation was performed using 108 ϕ and ψ dihedral angles, combined with the NOEs obtained in our previous determination of the cAMP-free form of the CNBD (1) for those regions not affected by the interaction with TRIP8b$_{nano}$. The 10 conformers of TRIP8b$_{nano}$ and CNBD with the lowest residual target function values were subjected to restrained energy minimization with AMBER 12.0 (4) (http://pyenmr.cerm.unifi.it/access/index/amps-nmr) and used as input in docking calculations.

Docking calculations. Docking calculations were performed with HADDOCK2.2 implemented in the WeNMR/West-Life GRID-enabled web portal (www.wenmr.eu). The docking calculations are driven by ambiguous interaction restraints (AIRs) between all residues involved in the intermolecular interactions (5). Active residues of the CNBD were defined as the surface exposed residues (at least 50% of solvent accessibility), which show chemical shift perturbation upon TRIP8b$_{nano}$ binding.

The assignment of the CNBD bound to TRIP8b$_{nano}$ allowed to highlight the residues of CNBD whose backbone featured appreciable Combined Chemical Shift Perturbation (CSP) (Fig. S2). The combined CSP (Δ_{HN}) is given by the equation $\Delta_{HN}=\{((H_{Nfree}-H_{Nbound})^2+((N_{free}-N_{bound})/5)^2)/2\}^{½}$ (6).

Passive residues of CNBD were defined as the residues close in space to active residues and with at least 50% solvent accessibility.

In the case of TRIP8b$_{nano}$, the conserved stretch E_{239}-E_{243}, located in helix N, was defined as active region in a first docking calculation, while all the other solvent accessible residues of the peptide were defined as passive. This docking calculation generated several clusters. A post-docking filter step allowed us to select those clusters having an orientation of TRIP8b$_{nano}$ bound to CNBD in agreement with a DEER study on the CNBD - TRIP8b$_{nano}$ interaction (7). The selected clusters grouped in two classes on the basis of the orientation of helix N of TRIP8b$_{nano}$ (N) relative to CNBD (Fig S3). A second docking calculation was subsequently performed introducing also residues E_{264}-E_{265}, located in helix C of TRIP8b$_{nano}$ as active residues. The active residues for CNBD were the same used for the first calculation. For this second HADDOCK calculation 14 clusters were obtained and ranked according to their HADDOCK score. Among them only four clusters showed both an orientation of TRIP8b$_{nano}$ bound to CNBD in agreement with the DEER study (7) and the involvement of E_{239}-E_{243} stretch of TRIP8b$_{nano}$ in the binding to CNBD. These clusters were manually analyzed and subjected to a per-cluster re-analysis following the protocol reported in http://www.bonvinlab.org/software/haddock2.2/analysis/#reanal. From this analysis, it resulted that the top-ranking cluster, i.e. the one with the best energetic and scoring functions, has a conformation in agreement with mutagenesis experiments (Fig. S4). Energy parameters (van der Waals energy, electrostatic energy, desolvation energy, and the penalty energy due to violation of restraints) for this complex model are reported in Table S2.

Both docking calculations were performed using 10 NMR conformers of both the CNBD and the TRIP8b$_{nano}$ structures calculated as described above. In the TRIP8b$_{nano}$ structures the unfolded N- and C-terminal regions were removed, while in the CNBD structures only the unfolded N-terminal region was removed. This is because the C-terminal region of the CNBD is known to comprise residues involved in TRIP8b$_{nano}$ binding (1). Flexible regions of the proteins were defined based on the active and passive residues plus two preceding and following residues. The residue solvent accessibility was calculated with the program

NACCESS (8). In the initial rigid body docking calculation phase, 5000 structures of the complex were generated, and the best 400 in terms of total intermolecular energy were further submitted to the semi-flexible simulated annealing and a final refinement in water. Random removal of the restraints was turned off. The number of flexible refinement steps was increased from the default value of 500/500/1000/1000 to 2000/2000/2000/4000. The final 400 structures were then clustered using a cutoff of 5.0 Å of RMSD to take into consideration the smaller size of protein-peptide interface.

Electrophysiology of HEK 293T cells. HEK 293T cells were cultured in Dulbecco's modified Eagle's medium (Euroclone) supplemented with 10% fetal bovine serum (Euroclone), 1% Pen Strep (100 U/mL of penicillin and 100 µg/ml of streptomycin), and stored in a 37°C humidified incubator with 5% CO_2. The plasmid containing cDNA of wild-type and mutant HCN1, HCN2 and HCN4 channels (1 µg) was co-transfected for transient expression into HEK 293T cells with a plasmid containing cDNA of Green Fluorescent Protein (GFP) (1.3 µg). For co-expression with TRIP8b (1a-4), HEK 293T cells were transiently transfected with wild-type (wt) and/or mutant human HCN1 cDNA (1 µg), wt TRIP8b (1a-4) cDNA (1 µg) and cDNA of Green Fluorescent Protein (GFP) (0.3 µg).

One day after transfection, GFP-expressing cells were selected for patch-clamp experiments in whole-cell configuration. The experiments were conducted at R.T. The pipette solution in whole cell experiments contained: 10 mM NaCl, 130 mM KCl, 1 mM egtazic acid (EGTA), 0.5 mM $MgCl_2$, 2 mM ATP (Mg salt) and 5 mM HEPES–KOH buffer (pH 7.4). The extracellular bath solution contained 110 mM NaCl, 30 mM KCl, 1.8 mM $CaCl_2$, 0.5 mM $MgCl_2$ and 5 mM HEPES–KOH buffer (pH 7.4).

$TRIP8b_{nano}$ was added (10 µM) to the pipette solution. cAMP was added at different concentration to the pipette solution depending on the HCN isoform used: 0 µM for HCN1, 5 µM for HCN2 and 1 µM for HCN4.

Whole-cell measurements of HCN channels were performed using the following voltage clamp protocol depending on the HCN isoform measured: for HCN1, holding potential was –30 mV (1s), with steps from –40 mV to –130 mV (10 mV interval, 3.5 s) and tail currents recorded at –40mV (3 s); for HCN2, holding potential was –30 mV (1 s), with steps from –40 mV to –150 mV (10 mV interval, 5 s) and tail currents recorded at -40mV (5 s); for HCN4, holding potential was –30 mV (1s), steps from –40 mV to –160 mV (10 mV interval, 6 s) and tail currents were recorded at -40mV (6 s).

Isolation and electrophysiology of sinoatrial node cells. Animal protocols conformed to the guidelines of the care and use of laboratory animals established by Italian and European Directives (D. Lgs n° 2014/26, 2010/63/UE). New Zealand white female rabbits (0.8–1.2 kg) were anesthetized (xylazine 5mg/Kg, i.m.), and euthanized with an overdose of sodium thiopental (i.v.); hearts were quickly removed, and the SAN region was isolated and cut in small pieces. Single SAN cardiomyocytes were isolated following an enzymatic and mechanical procedure as previously described (9). Following isolation, cells were maintained at 4 °C in Tyrode solution: 140 mM NaCl, 5.4 mM KCl, 1.8 mM $CaCl_2$, 1 mM $MgCl_2$, 5.5 mM D-glucose, 5 mM HEPES-NaOH (pH 7.4).

For patch clamp experiments cells were placed in a chamber on an inverted microscope and experiments were performed in the whole-cell configuration at 35 ± 0.5 °C. The pipette solution contained: 10 mM NaCl, 130 mM KCl, 1 mM egtazic acid (EGTA), 0.5 mM $MgCl_2$, and 5 mM HEPES–KOH buffer (pH 7.2). The I_f current was recorded from single cells superfused with Tyrode solution with 1 mM $BaCl_2$, and 2 mM $MnCl_2$.

I_f activation curves were obtained using a two-step protocol in which test voltage steps (from -30 to -120 mV, 15 mV interval) were applied from a holding potential of -30 mV and were followed by a step to -125 mV. Test steps had variable durations so as to reach steady – state activation at all voltages.

In current-clamp studies, spontaneous action potentials were recorded from single cells superfused with Tyrode solution, and rate was measured from the interval between successive action potential. When indicated cAMP (1 μM) and/or nanoTRIP8b (10 μM) were added to the pipette solution.

Data analysis. Data were acquired at 1 kHz using an Axopatch 200B amplifier and pClamp10.5 software (Axon Instruments). Data were analyzed off-line using Clampfit 10.5 (Molecular Devices) and Origin 16 (OriginLab Corp., Northampton MA). Activation curves were analyzed by the Boltzmann equation, $y=1/\{1+\exp[(V-V1/2)/s]\}$, where y is fractional activation, V is voltage, $V_{1/2}$ half-activation voltage, and s the inverse slope factor (mV) (10). Mean activation curves were obtained by fitting individual curves from each cell to the Boltzmann equation and then averaging all curves obtained.

1. Saponaro A, et al. (2014) Structural basis for the mutual antagonism of cAMP and TRIP8b in regulating HCN channel function. *Proc Natl Acad Sci U S A* 111(40):14577–14582.

2. Cornilescu G, Delaglio F, Bax A (1999) Protein backbone angle restraints from searching a database for chemical shift and sequence homology. *J Biomol NMR* 13(3):289–302.
3. Guntert P, Buchner L (2015) Combined automated NOE assignment and structure calculation with CYANA. *J Biomol NMR* 62(4):453–471.
4. Case DA, et al. (2012) AMBER 12 (University of California, San Francisco).
5. Dominguez C, Boelens R, Bonvin AMJJ (2003) HADDOCK: a protein-protein docking approach based on biochemical or biophysical information. *J Am Chem Soc* 125(7):1731–1737.
6. Garrett DS, Seok YJ, Peterkofsky A, Clore GM, Gronenborn AM (1997) Identification by NMR of the binding surface for the histidine-containing phosphocarrier protein HPr on the N-terminal domain of enzyme I of the Escherichia coli phosphotransferase system. *Biochemistry* 36(15):4393–4398.
7. Deberg HA, et al. (2015) Structural mechanism for the regulation of HCN ion channels by the accessory protein TRIP8b. *Structure* 23(4):734–744.
8. Hubbard SJ, Hornton JM (1993) NACCESS, Computer Program (Department of Biochemistry and Molecular Biology, University College London.
9. DiFrancesco D, Ferroni A, Mazzanti M, Tromba C (1986) Properties of the hyperpolarizing-activated current (if) in cells isolated from the rabbit sino-atrial node. *J Physiol* 377:61–88.
10. DiFrancesco D (1999) Dual allosteric modulation of pacemaker (f) channels by cAMP and voltage in rabbit SA node. *J Physiol* 515 (Pt 2:367–376.

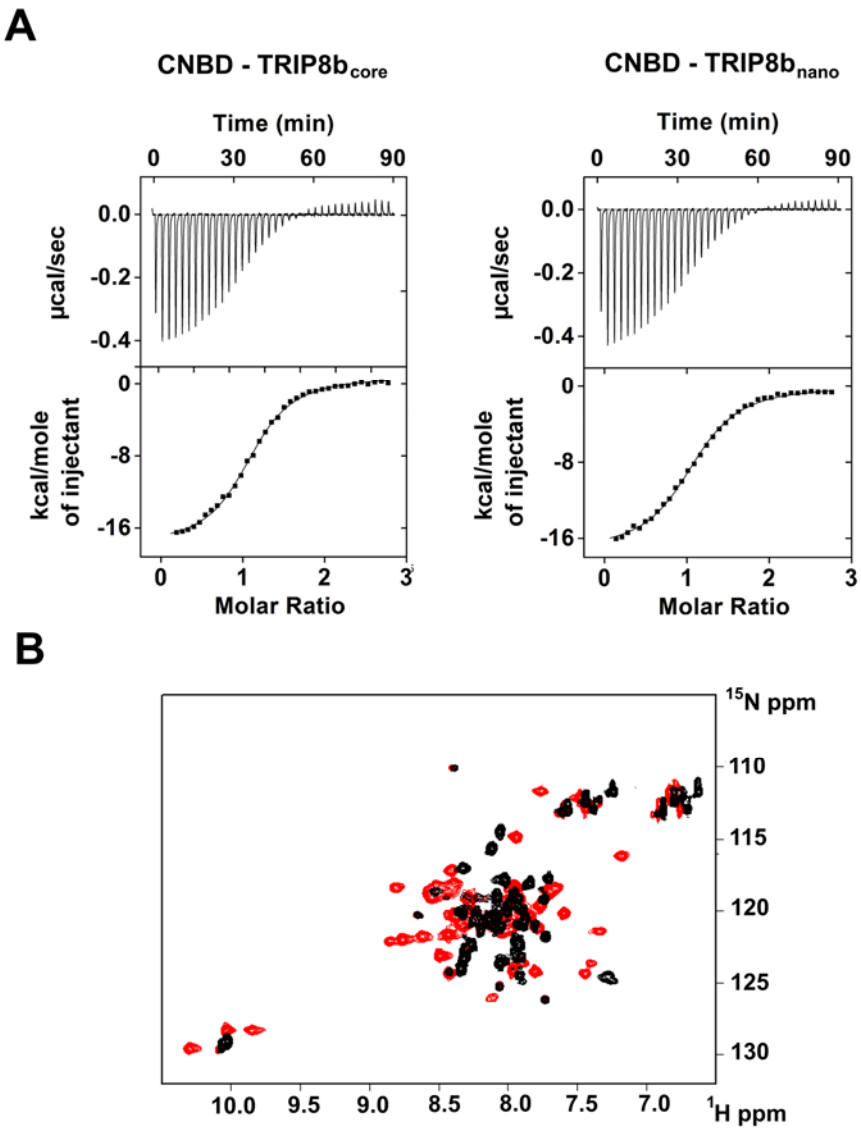

Fig. S1. Functional and structural characterization of TRIP8b$_{nano}$**.** (A) Binding of TRIP8b$_{core}$ and TRIP8b$_{nano}$ to purified His$_6$-MBP-CNBD measured by Isothermal titration calorimetry (ITC). Upper panel, heat changes (µcal/sec) during successive injections of 8 µL of the corresponding TRIP8b peptide (200 µM) into the chamber containing His$_6$-MBP-CNBD (20 µM). Lower panel, binding curve obtained from data displayed in the upper panel. The peaks were integrated, normalized to TRIP8b peptide concentration, and plotted against the molar ratio (TRIP8b peptide / His$_6$-MBP-CNBD). Solid line represents a nonlinear least-squares fit to a single-site binding model (1), yielding, in the present examples, a K_D = 1.2 ± 0.1 µM for TRIP8b$_{core}$ and K_D = 1.4 ± 0.1 µM for TRIP8b$_{nano}$. (B) Evidence for TRIP8b$_{nano}$ folding upon CNBD binding based on the superimposition of the [^{1}H, ^{15}N] heteronuclear single quantum coherence (HSQC) NMR spectrum of CNBD-free TRIP8b$_{nano}$ (black) and CNBD-bound

TRIP8b$_{nano}$ (red). The latter experiment was performed at the molar ratio ([CNBD]/[TRIP8b$_{nano}$]) = 3.

1. Saponaro A, et al. (2014) Structural basis for the mutual antagonism of cAMP and TRIP8b in regulating HCN channel function. *Proc Natl Acad Sci U S A* 111(40):14577–14582.

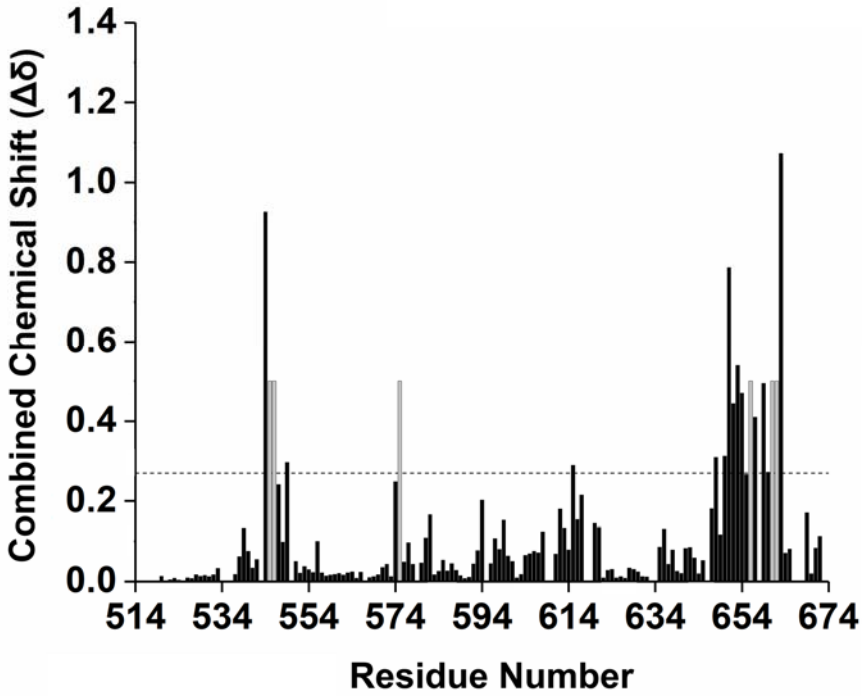

Fig. S2. CNBD residues involved in TRIP8b$_{nano}$ binding. Combined chemical shift variations of NMR signals between CNBD unbound and TRIP8b$_{nano}$-bound state. Combined chemical shift variations are calculated from the experimental ^{1}H and ^{15}N chemical shift changes (Δδ(^{1}H) and Δδ (^{15}N), respectively) between corresponding peaks in the two forms, through the following equation (1).

$$\Delta\delta^{combined} = \sqrt{\frac{\left(\Delta\delta\left(^{1}\mathrm{H}\right)\right)^{2} + \frac{1}{25}\left(\Delta\delta\left(^{15}\mathrm{N}\right)\right)^{2}}{2}}$$

Residues experiencing intermediate exchange regime (whose NMR signal becomes broad beyond detection upon addition of TRIP8b$_{nano}$) are shown in grey. The horizontal dotted line indicates the average value plus one standard deviation. Residues above the line were set as “active” in the docking calculation described in the text (see *SI Materials and Methods*).

1. Garrett DS, Seok YJ, Peterkofsky A, Clore GM, Gronenborn AM (1997) Identification by NMR of the binding surface for the histidine-containing phosphocarrier protein HPr on the N-terminal domain of enzyme I of the Escherichia coli phosphotransferase system. *Biochemistry* 36(15):4393–4398.

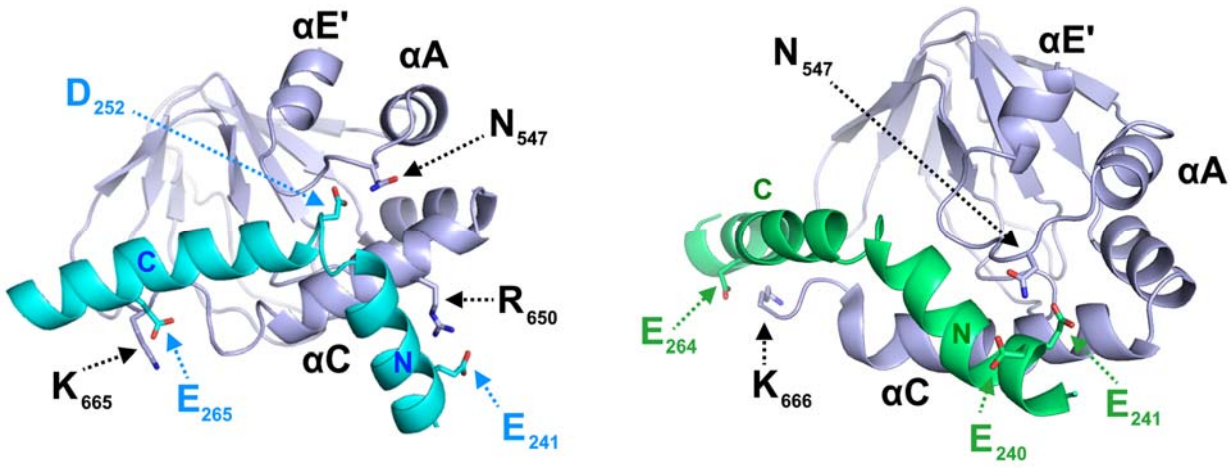

Fig. S3. Representative families of clusters obtained from the first docking calculation. The clusters obtained can be grouped in two classes, shown here, on the basis of the position of helix N of TRIP8b$_{nano}$ (N) relative to the CNBD. In the left representative structure, helix N is oriented in a way that allows E_{241} to interact with R_{650} of C-helix. In the right representative structure, E_{240} - E_{241} interact with N_{547} of CNBD. In all clusters K_{665} or K_{666} of CNBD establish a contact with either E_{264} or E_{265} of TRIP8b$_{nano}$. The structural elements of CNBD are labelled: αE', αA and αC. Helices N and C of TRIP8b$_{nano}$ are labelled.

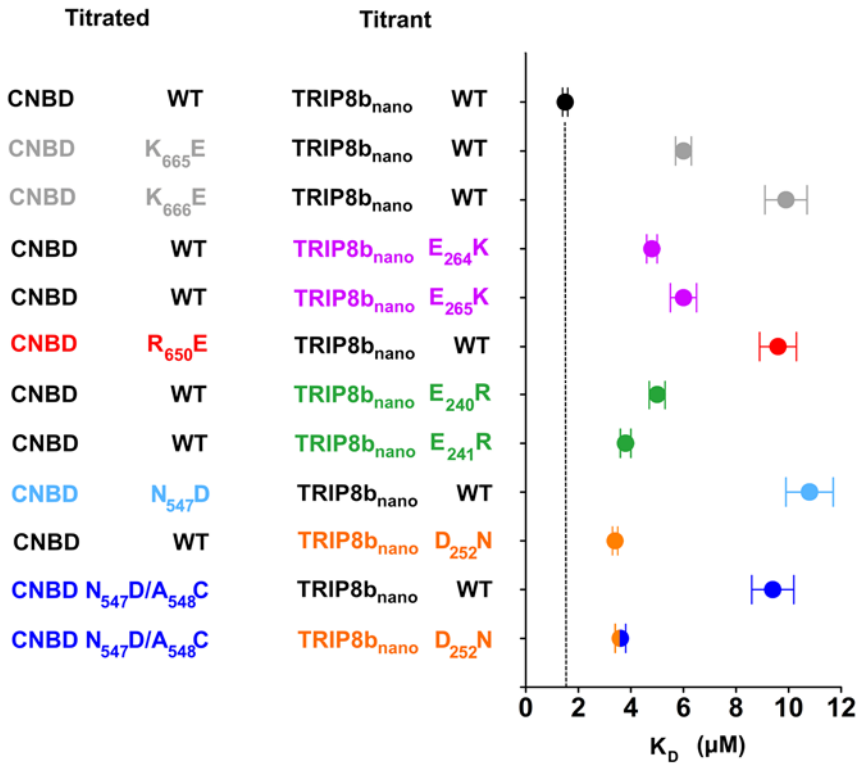

Fig. S4. Biochemical validation of CNBD – TRIP8b$_{nano}$ complex. Dissociation constant (K_D) of the interaction between the indicated CNBD and TRIP8b$_{nano}$ peptides were measured by means of Isothermal Titration Calorimetry (ITC). CNBD WT - TRIP8b$_{nano}$ WT (black filled circle) = 1.4 ± 0.1 μM; CNBD K$_{665}$E - TRIP8b$_{nano}$ WT (grey filled circle) = 6 ± 0.3 μM; CNBD K$_{666}$E - TRIP8b$_{nano}$ WT (grey filled circle) = 9.9 ± 0.8 μM; CNBD WT - TRIP8b$_{nano}$ E$_{64}$K (purple filled circle) = 4.8 ± 0.2 μM; CNBD WT - TRIP8b$_{nano}$ E$_{65}$K (purple filled circle) = 6 ± 0.5 μM; CNBD R$_{650}$E - TRIP8b$_{nano}$ WT (red filled circle) = 9.6 ± 0.7 μM; CNBD WT - TRIP8b$_{nano}$ E$_{40}$R (green filled circle) = 5 ± 0.3 μM; CNBD WT - TRIP8b$_{nano}$ E$_{41}$R (green filled circle) = 3.8 ± 0.2 μM; CNBD N$_{547}$D - TRIP8b$_{nano}$ WT (light blue filled circle) = 11 ± 0.9 μM; CNBD WT - TRIP8b$_{nano}$ D$_{52}$N (orange filled circle) = 3.4 ± 0.1 μM; CNBD N$_{547}$D/A$_{548}$C - TRIP8b$_{nano}$ WT (blue filled circle) = 9.3 ± 0.9 μM; CNBD N$_{547}$D/A$_{548}$C - TRIP8b$_{nano}$ D$_{52}$N (orange/blue filled circle) = 3.6 ± 0.2 μM. Data are presented as mean ± SEM. Number of experiments (N) ≥ 3. K_D values of all tested combinations are statistically different from the K_D of CNBD WT for TRIP8b$_{nano}$ WT (*, P ≤ 0.05; **, P < 0.01). K_D of CNBD N$_{547}$D/A$_{548}$C for TRIP8b$_{nano}$ WT and K_D of CNBD N$_{547}$D/A$_{548}$C for TRIP8b$_{nano}$ D$_{52}$N are statistically different (**, P < 0.01). Statistical analysis performed with ANOVA, followed by post-hoc Tukey test. Dashed black vertical line indicates the K_D of WT peptides.

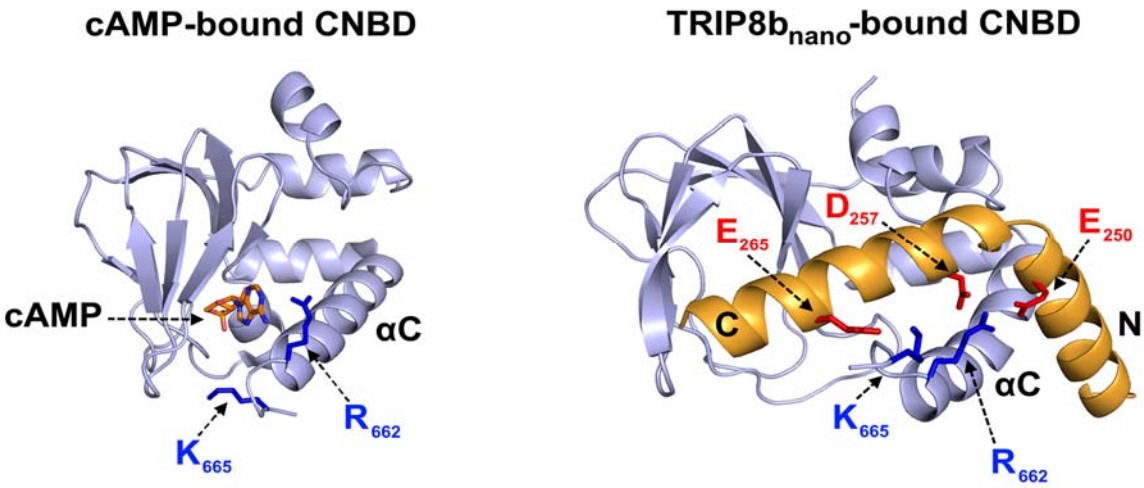

Fig. S5. Different orientation of R_{662} and K_{665} in the cAMP-bound (1) and TRIP8b$_{nano}$-bound conformation of the CNBD (this study). Residues R_{662} and K_{665} of CNBD C-helix (αC) which interact with cAMP (left) and TRIP8b$_{nano}$ (right) are represented as blue sticks and labelled. TRIP8b$_{nano}$ residues E_{250} and D_{257} interacting with R_{662} and residue E_{265} interacting with K_{665} are shown in red sticks and labelled.

1. Lolicato M, et al. (2011) Tetramerization dynamics of C-terminal domain underlies isoform-specific cAMP gating in hyperpolarization-activated cyclic nucleotide-gated channels. *J Biol Chem* 286(52):44811–44820.

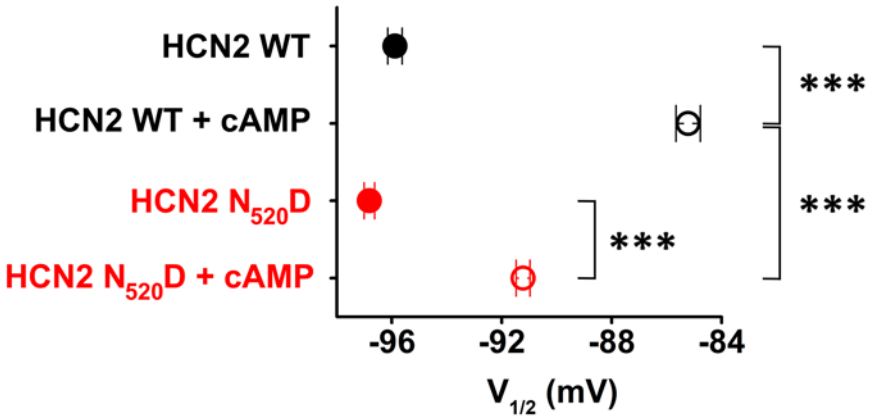

Fig. S6. Mutation $N_{520}D$ affects cAMP affinity in full-length HCN2 channel. Note that in mouse HCN2 $N_{520}D$ corresponds to $N_{547}D$ in human HCN2 (used in our structural studies). HCN2 currents were recorded by patch clamp in HEK 293T cells and analysed as described

in *SI Material and Methods*. The effect of 5 µM cAMP on half activation potential is shown here ($V_{1/2}$). HCN2 WT (black filled circle) $V_{1/2}$ = -95.9 ± 0.3 mV; HCN2 WT + cAMP (black open circle) $V_{1/2}$ = 85.2 ± 0.4 mV; HCN2 $N_{520}D$ (red filled circle) $V_{1/2}$ = -96.8 ± 0.2 mV; HCN2 $N_{520}D$ + cAMP (red open circle) $V_{1/2}$ = -91.2 ± 0.2 mV. Data are presented as mean ± SEM. Number of experiments (N) ≥ 6. Statistical analysis performed with ANOVA, followed by post-hoc Tukey test (***, P < 0.001).

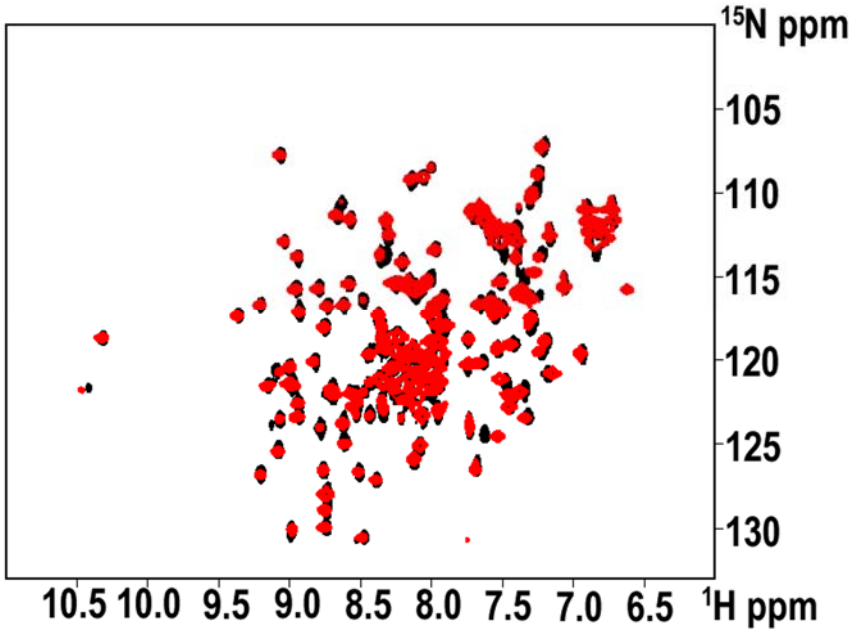

Fig. S7. Structural characterization of $N_{547}D$ CNBD protein. Superimposition of the [^{1}H, ^{15}N] HSQC spectra of CNBD wt (black) and CNBD $N_{547}D$ mutant (red).

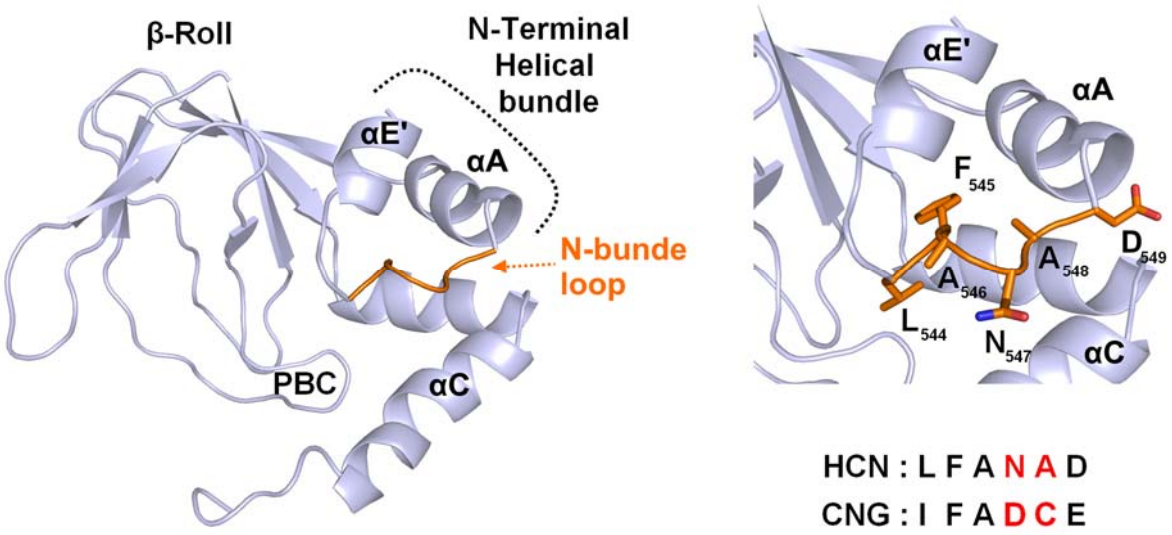

Fig. S8. Structural insights into the N-bundle loop of the CNBD. Left, ribbon representation of human HCN2 CNBD structure (cAMP-free conformation; (1)). The main structural elements are labelled: β-Roll; N-terminal helical bundle, which is composed by α-helices E' and A (αE', αA) interconnected by the N-bundle loop (orange); Phosphate Binding Cassette (PBC); α-helix C. Right, close-up view showing the residues of the N-bundle loop, labelled and coloured in orange. The alignment of the N-bundle loop sequences of mammalian HCN and CNG channels (shown here is CNGA1) is reported below. Non-conservative substitutions are highlighted in red.

1. Saponaro A, et al. (2014) Structural basis for the mutual antagonism of cAMP and TRIP8b in regulating HCN channel function. *Proc Natl Acad Sci U S A* 111(40):14577–14582.

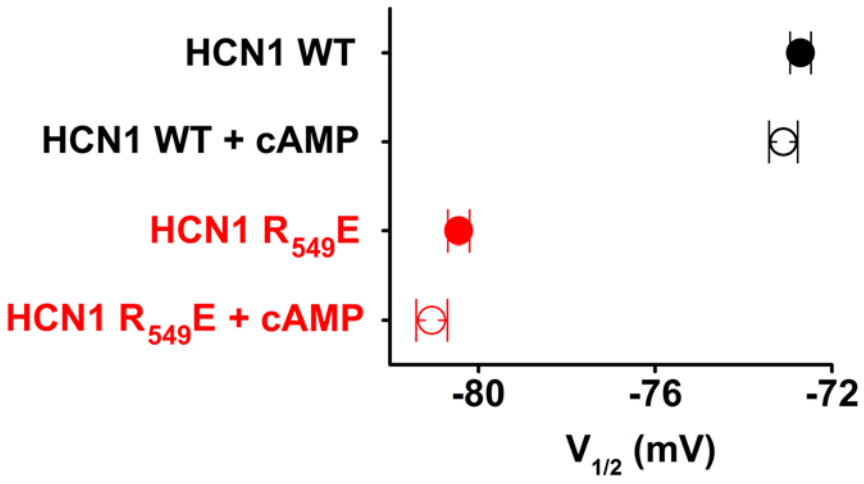

Fig. S9. Comparison of half activation potentials of human HCN1 WT and of the cAMP-insensitive $R_{549}E$ mutant (1). Currents were measured by patch clamp from HEK 293T cells transfected with WT and $R_{549}E$ mutant in the absence and presence of 15 µM cAMP in the pipette. Half activation potential ($V_{1/2}$) was determined as described in *SI Material and Methods*. HCN1 WT (black filled circle) = -72.7 ± 0.2 mV; HCN1 WT + cAMP (black open circle) = 73.1 ± 0.3 mV; HCN1 $R_{549}E$ (red filled circle) = -80.4 ± 0.2 mV; HCN1 $R_{549}E$ + cAMP (red open circle) = -81 ± 0.3 mV. Data are presented as mean ± SEM. Number of experiments (N) ≥ 8.

1. Chen S, Wang J, Siegelbaum SA (2001) Properties of Hyperpolarization-Activated Pacemaker Current Defined by Coassembly of Hcn1 and Hcn2 Subunits and Basal Modulation by Cyclic Nucleotide. *J Gen Physiol* 117(5):491–504.

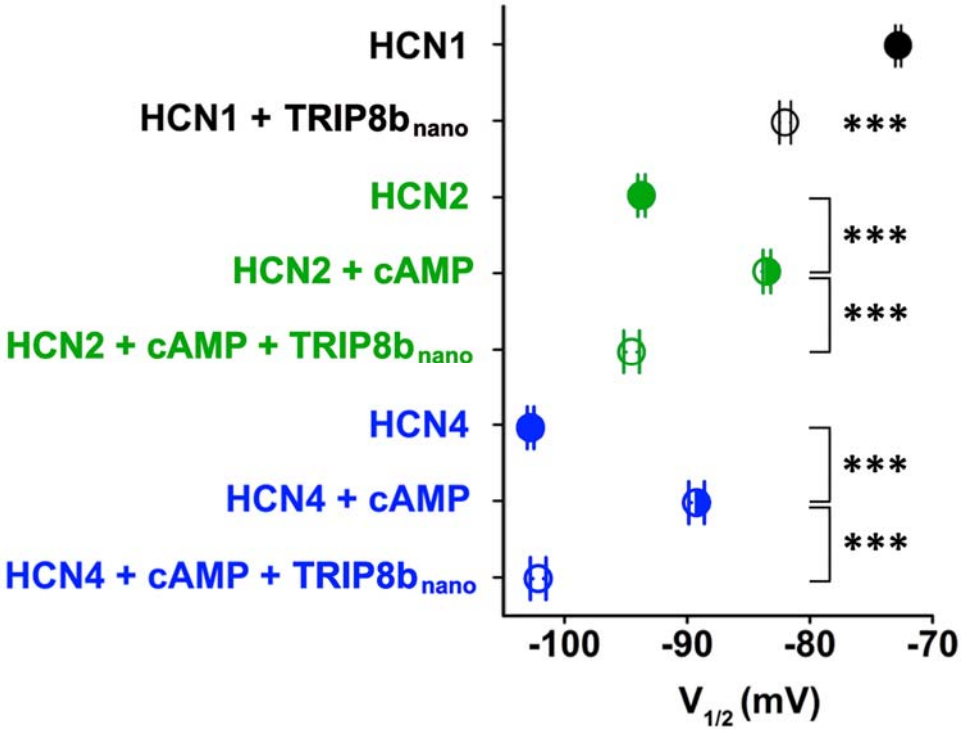

Fig. S10. TRIP8b$_{nano}$ abolishes cAMP effect on HCN channel gating. Effect of TRIP8b$_{nano}$ on human HCN1, mouse HCN2 and rabbit HCN4 half activation potentials ($V_{1/2}$). HCN1 (black filled circle) = -72.8 ± 0.2 mV; HCN1 + 10 µM TRIP8b$_{nano}$ (black open circle) = -82 ± 0.5 mV; HCN2 (green filled circle) = -93.7± 0.3 mV; HCN2 + 5 µM cAMP (green semi-open circle) = -83.5 ± 0.3 mV; HCN2 + 5 µM cAMP + 10 µM TRIP8b$_{nano}$ (green open circle) = -94.5 ± 0.6 mV; HCN4 (blue filled circle) = -102.8 ± 0.3 mV; HCN4 + 1µM cAMP (blue semi-open circle) = -89.2 ± 0.6 mV; HCN4 + 1µM cAMP + 10 µM TRIP8b$_{nano}$ (blue open circle) = -102.1 ± 0.6 mV. Data are presented as mean ± SEM. Number of cells (N) ≥ 11. Statistical analysis performed with ANOVA, followed by post-hoc Tukey test (***, P < 0.001).

Table S1. Acquisition parameters for NMR experiments performed on cAMP-free human HCN2 CNBD in complex with TRIP8bnano and vice-versa.

Experiments	Dimension of acquired data			Spectral width (ppm)			n[a]
	t_1	t_2	t_3	F_1	F_2	F_3	
HCN2 CNBD [b]							
^{1}H-^{15}N-HSQC	256(^{15}N)	1024(^{1}H)		32	16		8
CBCA(CO)NH	108(^{13}C)	56(^{15}N)	2048(^{1}H)	72	32	16	16
HNCACB	108(^{13}C)	56(^{15}N)	2048(^{1}H)	72	32	16	16
HNCO	80(^{13}C)	56(^{15}N)	2048(^{1}H)	18	32	16	4
HN(CA)CO	80(^{13}C)	56(^{15}N)	2048(^{1}H)	18	32	16	16
^{15}N-edited [^{1}H-^{1}H]-NOESY[c]	192(^{1}H)	74(^{15}N)	2048(^{1}H)	14	70	14	16
TRIP8bnano[d]							
^{1}H-^{15}N-HSQC	128(^{15}N)	1024(^{1}H)		40	14		16
CBCA(CO)NH	88(^{13}C)	48(^{15}N)	2048(^{1}H)	80	40	16	24
HNCACB	88(^{13}C)	48(^{15}N)	2048(^{1}H)	80	40	16	24
HNCA	88(^{13}C)	48(^{15}N)	1024(^{1}H)	50	40	16	24
HN(CO)CA	88(^{13}C)	48(^{15}N)	1024(^{1}H)	50	40	16	24

[a] number of acquired scans. [b] Experiments were acquired on a 700 MHz Bruker spectrometer equipped with a triple resonance cryoprobe at 298 K. All the triple resonance (TCI 5-mm) probes used were equipped with Pulsed Field Gradients along the z-axis.
[c] ^{15}N-edited edited 3D NOESY-HSQC experiments was acquired with a mixing time value of 100ms at the Bruker Avance 950 MHz spectrometer. [d] Experiments were acquired on a 500 MHz Bruker spectrometer equipped with a triple resonance cryoprobe at 298 K. All 3D and 2D spectra were processed using the standard Bruker software TOPSPIN 2.1 and analyzed through CARA (1,2).

1. Keller R, Wüthrich KA. (2002) New Software for the Analysis of Protein NMR Spectra.

2. Keller RLJ. (2004) The Computer Aided Resonance Assignment tutorial. Goldau: CANTINA Verlag.

Table S2. Docking calculation.

	Cluster 1 [a]
HADDOCK Score [b]	-130 (7)
RMSD (Å) [c]	1.8 (0.9)
Number of structures	71
BSA (Å^2) [d]	1968 (106)
EAIR [e]	30.5 (15.2)
Einter[f]	-398(50)
Enb[g]	-431(46)

Statistics on the top-ranking cluster of the structural models of CNBD and TRIP8b$_{nano}$ complex obtained through HADDOCK2.2 calculations and in agreement with previous experimental data (1). Averages (standard deviations are reported in parenthesis) were calculated over the best ten structures.

[a] Cluster rank according to the HADDOCK score. [b] HADDOCK score defined as a weighted sum of different energetic terms, such as: van der Waals energy, electrostatic energy, distance restraints energy, buried surface area, binding energy and desolvation energy. [c] Backbone RMSD from the lowest HADDOCK score structure in each cluster. Some individual energy terms are also reported: [d] Buried surface area, [e] distance restraints energy, [f] binding energy, [g] non-bonded interaction energy.

1. Deberg HA, et al. (2015) Structural mechanism for the regulation of HCN ion channels by the accessory protein TRIP8b. *Structure* 23(4):734–744.

PART III

MATHERIALS AND METHODS OF HCN-MINT INTERACTION

1. HEK293T electrophysiology

HEK293T cells were co—transfected with Turbofect transfection reagent (ThermoFisher Scientific). For each 35 mm petri dish, 1 μg of HCN1 or HCN2 cDNA (pIRES::mHCN1 from A. Bucchi; pCI::mHCN2 from B. Santoro) was used plus 1 μg of EGFP (as control, pmaxGFP AmaxaBiosystems) or 1 μg of Mint proteins cDNA (pEC::rMint1, pEC::rMint2 and pEC::rMint3 from B.Santoro). The constructs of the deleted mHCN2 (pCI vector) channels were obtained by inserting two codon stops after residues 643, 679 and 813 with the QuikChange Lightning Site-Directed Mutagenesis Kit (Agilent, #210519).

Transfected cells were detected by GFP fluorescence.

For the recordings, the extracellular solution used was: 110 mM NaCl, 30 mM KCl, 1.8 mM $CaCl_2$, 0.5 mM $MgCl_2$ and 5 mM HEPES–KOH buffer (pH 7.4). Recording pipettes were fabricated from 1.5mm o.d. borosilicate glass capillaries with a P-97 Flaming/Brown Micropipette Puller (Sutter, Novato, CA, USA) and had resistances of 3–5MΩ. The pipettes were filled with the following intracellular solution: 10 mM NaCl, 130 mM KCl, 1 mM EGTA, 0.5 mM $MgCl_2$, 2 mM MgATP and 5 mM HEPES–KOH buffer (pH 7.4).

Currents were recorded in whole cells configuration with a Dagan 3900A (Degan, Minneapolis, MN, USA). Data were digitized with an Axon Digidata 1322 A/D (Axon Instruments, CA, USA) converter and analysed with Axon pClamp9. To obtain channel activation, cells were held at -40 mV and then hyperpolarizing steps (from -160 to -25 mV) of variable duration were applied in order to reach steady-state activation at all voltages. After, current tails were measured by returning to -40mV. To analyse current density, the steady-state current amplitude was measured at the end of each test potential, and normalized to cell capacitance. Mean activation curves were obtained by fitting maximal tail current amplitude, plotted against the voltage step applied, with the Boltzmann equation It=It(max)/(1+exp(V-V1/2)/k. It stands for the current amplitude of the tail current recorded for a given pre-pulse, It(max) is the maximum current amplitude of the tail current, V is the voltage of the pre-pulse, $V_{1/2}$ is the half-activation voltage and k is the slope factor in mV using Originpro software (Originlab, Northampton, MA, USA). Unpaired Student's tests (Origin software) was used to make comparisons. All data are shown as mean ± S.E.M.

2. Immunocytochemistry

HEK293T cells were transfected with Turbofect transfection reagent (ThermoFisher Scientific) or X-tremeGENE™ HP DNA Transfection Reagent (Roche). Cells were washed in PBS, fixed in 4% PFA, washed in PBS and blocked with PBS + 0.1% Triton X-100 + 3% Normal Goat Serum (ThermoFisher Scientific). Triton X-100 was not used for not permeabilizing conditions. Incubation with primary and secondary antibodies was performed in PBS + 3% Normal Goat Serum. Primary antibodies used: anti-HA (12CA5) (Roche, 1:500), anti-HCN2 (Neuromab, 1:250).
Secondary antibodies used: Goat anti-Mouse IgG2b Alexa Fluor 546 (ThermoFisher Scientific, 1:1000, A-21143), Goat anti-Mouse IgG (H+L) Alexa Fluor 647 (ThermoFisher Scientific, 1:400).

3. Western Blot on HEK293T cell lysate

HEK293T cells were transfected with Turbofect transfection reagent (ThermoFisher Scientific). For each 35 mm petri dish, 1µg of HCN1 or 2 (pIRES::mHCN1 from A. Bucchi; pCI::mHCN2 from B. Santoro) was used plus 1 µg of EGFP (as control, pmaxGFP AmaxaBiosystems) or 1 µg of Mint proteins cDNA (pEC::rMint1, pEC::rMint2, pEC::rMint3 and pEC::TRIP8b(1a-4) from B.Santoro). Cells were lysed in the lysis buffer (150 mM NaCl, 10 mM Tris-Cl pH 7.4, 2 mM EDTA, 1% Triton X-100) with protease inhibitors (Complete Mini, Roche). Cell lysates were kept in ice for 30 minutes and then centrifuged. The surnatant protein concentration was calculated with Pierce BCA protein assay kit (ThermoFisher Scientific #23225). For the Western Blot analysis of protein expression, cell lysates were run on 4-12% SDS-PAGE (ThermoFisher Scientific), transferred to a polyvinyldene difluoride membrane (PVDF, Bio-Rad) in transfer buffer (192 mM glycine, 25 mM Tris-HCl, 20% methanol). Membranes were blocked in TBST + 2% BSA. Primary antibodies incubation was performed in over-night at 4°C in TBST + 2% BSA. Primary antibodies used: anti-HCN1 RTQ (Millipore, 1:1000) and anti-HCN2 (APC-030 Alomone, 1:300). After being washed in TBST, membranes were incubated with secondary antibodies in PBS + 5% w/v milk. Secondary antibodies used: HRP-conjugate anti-rabbit (1:10000, Cell Signaling Technology #7074) and HRP-conjugate anti-mouse (1:10000, Cell Signaling Technology #7076). Protein bands were detected with SuperSignal West Pico chemiluminescent substrate (ThermoFisher Scientific #34080).

4. Protein co-expression and co-purification

In pGEX-6P-2rb, the cDNA of MID domain of the rat isoform Mint2 (from residue 1 to residue 356) was cloned BamHI/EcoRI. In pET24b, the cDNA of the short HCN2 CNBD (from residue 521 to 672 of the human isoform) and the one of the long HCN2 CNBD (from residue 594 to 676 of the murine isoform) were cloned with the LIC system.

Plasmids were co-transformed in *E.coli* BL21 Rosetta strain (Novagen). Cells were grown at 37°C and induced with IPTG 0.4Mm at OD_{600}=0.6. Three hour after induction, cells were harvested by centrifugation. Pellets were re-suspended in ice-cold lysis buffer (PBS + 5 mM β-mercaptoethanol, 5 µg/ml leupeptin, 1µg/ml pepstatin, 100 µM phenylmethylsulphonyl chloride, 10 µg/ml DNase and 0.25 mg/ml lysozyme). The lysate was sonicated 16 times 20 seconds, and then centrifuged 30 min 20000 x *g*. All purification steps were performed at 4 °C and monitored using the AKTApurifier UPC 10 fast protein liquid chromatography system (GE Healthcare). For the affinity purification, the GSTrap 4B column (GE Healthcare) was used. Protein complex was eluted in 50 mM TrisHCl pH8 + 10 mM reduced glutathione. The elution was loaded into a HiLoad 16/60 Superdex 75 prep grade size exclusion column (GE Healthcare). The fractions corresponding to the peaks were analysed by SDS-PAGE and Western blot. Anti-polyHistidine (mouse monoclonal, 1:1000, Sigma-Aldrich H1029) was used as primary antibody and goat anti-mouse IgG antibody linked to the Alkaline Phosphatase (1:1000, Sigma-Aldrich A3688) was used as secondary antibody. For protein detection, SIGMAFAST™ BCIP®/NBT tablets (Sigma-Aldrich) was used.

5. Yeast two-hybrid assay

Assays were performed using the Grow'N'Glow Two-Hybrid kit (Bio 101) and yeast strain EGY48. In vector pEG202 the following bait constructs were cloned: mHCN1 C-linker/CNBD short (from residue 390 to 592) and long (from residue 390 to 625), mHCN2 C-linker/CNBD short (from residue 443 to 643) and long (from residue 443 to 676), Munc18-1 (full-length). In pJG4-5 the prey constructs were cloned: miniTRIP8b (used as positive control, from residue 236 to 316 of TRIP8b(1b-2) (Santoro et al. 2011)), Mint1 full-length (rat isoform), Mint1 MID (rat isoform, from residue 1 to 446) ,Mint2 full-length (rat isoform), Mint2 MID (rat isoform, from residue 1 to 356). Cloning was performed with In-Fusion® HD Cloning Kit (Takara Bio USA).

Bait and prey plasmids were co-transformed with the reporter plasmid pGNG1 with the Frozen-EZ yeast transformation II kit (Zymo Reasearch). After transformation, cells were plated onto glucose-containing medium. Transformants were restreaked on selective medium (galactose+/leucine-), and after 3–5 days of growth, they are screened for positive GFP expression under a UV light.